ALMA MATER STUDIORUM - UNIVERSITÀ DI BOLOGNA

DOTTORATO IN SCIENZE DELLA TERRA

CICLO XXVI

Techniques for Lagrangian modelling of dispersion in geophysical flows

TESI DI DOTTORATO

Dottorando:

DANIELE ROSSI

Relatore:

Chiar.mo Prof. FRANCESCO TAMPIERI

Coordinatore:

Chiar.mo Prof. VINCENZO PICOTTI

Co-relatore:

Dott. ALBERTO MAURIZI

Abstract

Basic concepts and definitions relative to Lagrangian Particle Dispersion Models (LPDMs) for the description of turbulent dispersion are introduced. The study focusses on LPDMs that use as input, for the large scale motion, fields produced by Eulerian models, with the small scale motions described by Lagrangian Stochastic Models (LSMs).

The data of two different dynamical model have been used: a Large Eddy Simulation (LES) and a General Circulation Model (GCM). After reviewing the small scale closure adopted by the Eulerian model, the development and implementation of appropriate LSMs is outlined. The basic requirement of every LPDM used in this work is its fullfillment of the Well Mixed Condition (WMC).

For the dispersion description in the GCM domain, a stochastic model of Markov order 0, consistent with the eddy-viscosity closure of the dynamical model, is implemented.

A LSM of Markov order 1, more suitable for shorter timescales, has been implemented for the description of the unresolved motion of the LES fields. Different assumptions on the small scale correlation time are made.

Tests of the LSM on GCM fields suggest that the use of an interpolation algorithm able to maintain an analytical consistency between the diffusion coefficient and its derivative is mandatory if the model has to satisfy the WMC. Also a dynamical time step selection scheme based on the diffusion coefficient shape is introduced, and the criteria for the integration step selection are discussed.

Absolute and relative dispersion experiments are made with various unresolved motion settings for the LSM on LES data, and the results are compared with laboratory data. The study shows that the unresolved turbulence parameterization has a negligible

influence on the absolute dispersion, while it affects the contribution of the relative dispersion and meandering to absolute dispersion, as well as the Lagrangian correlation.

Riassunto

Il lavoro, dopo aver introdotto definizioni e concetti relativi ai Modelli Lagrangiani di Dispersione (LPDM), si focalizza su LPDM che fanno uso, per descrivere i moti a grande scala, di campi prodotti da modelli euleriani, con i moti a piccola scala descritti da Modelli Stocastici Lagrangiani (LSM).

Sono stati utilizzati i dati prodotti da due modelli dinamici: una Large Eddy Simulation (LES) ed un modello di circolazione globale (GCM). Dopo aver analizzato le chiusure adottate dai modelli euleriani, vengono descritti sviluppo ed implementazione dei modelli stocastici più appropriati. Una delle richieste fondamentali per ogni LPDM studiato è stato il rispetto della condizione di buon mescolamento (WMC).

Un modello stocastico markoviano di ordine 0, consistente con la chiusura del modello dinamico, è stata implementata per descrivere la dispersione nel dominio del modello a circolazione globale.

Per la simulazione degli effetti del campo di velocità non risolta dalla LES sulla dispersione, è stato invece utilizzato un modello markoviano di ordine 1, più adatto a descrivere la dispersione turbolenta per tempi scala più brevi. Sul tempo di correlazione delle piccole scale sono state testate diverse assunzioni.

I test compiuti sul LSM implementato sul modello di circolazione globale suggeriscono che, se la condizione di buon mescolamento deve essere mantenuta, l'algoritmo di interpolazione deve assicurare la consistenza analitica tra il valore del coefficiente di diffusione e la sua derivata. Vengono inoltre discussi i criteri utilizzati per la selezione di un passo di integrazione appropriato, e viene descritto uno schema per la selezione dinamica del *time step* basata sulla curvatura del profilo del coefficiente di diffusione.

Con il LPDM che utilizza i campi LES sono eseguiti esperimenti con diversi settaggi della parametrizzazione dei moti non risolti, confrontando i risultati con quelli ottenuti da esperimenti reali. Lo studio mostra che la dispersione assoluta è poco influenzata dalla chiusura a piccola scala del modello lagrangiano, che ha invece l'effetto di ridistribuire il contributo della dispersione assoluta in modo diverso tra le componenti di dispersione relativa e meandering.

Introduction

The use of particle dispersion modelling in geophysical flows

.

The description of the diffusion of pollutants is a central issue in many environmental studies.

The best suited models for the description of fluid dynamics are the Eulerian models, which integrate the equation of motion of the fluid at fixed points in space.

For air quality studies, one usually is interested in the characteristics of motion and concentration of masses of trackers transported by the flow. Among the techniques used to assess this problem, the Lagrangian approach, which follows a large set of tracker pollutant particle, is an efficient and flexible one for achieving such a task.

Lagrangian models are also easily adaptable to different problems and their physics is usually intuitive. On the other hand, describing the dynamics of complex flows in the Lagrangian framework is a daunting task. With this in mind, the use of an Eulerian model to provide dynamical fields for a Lagrangian model is a natural strategy. Throughout this text, one will refer to such a model simply as a Lagrangian Particle Dispersion Model (LPDM).

Still, the small scale turbulence has a non-negligible effect on the diffusion of particles, and the coarse gridded, smooth fields produced by an Eulerian model can not be enough precise to describe dispersion with the desired accuracy. This is especially true for the description of vertical motion in the Planetary Boundary Layer, where small scale turbulence is produced by shear or buoyancy.

Where the description of particle motions on scales smaller than the Eulerian model grid size is needed, a Lagrangian dispersion model can be provided with a parameterization describing unresolved motion effects. Many of such parameterizations have been explored. The most used, for its simplicity and numerical efficiency, is the description of unresolved kinetic fields by means of a Lagrangian Stochastic Model (LSM). A LSM simulate trajectories that are not (necessarily) solutions of the deterministic equation of motion of the fluid but mantain a pre-selected set of statistical properties of the flow (Asymptotic behaviour of tracer statistics, position - velocity moments, trajectory curvature, and other properties as well).

Some consideration have to be made when providing a LPDM with a LSM. Usually, a good parameterization is one that mantains consistency with the dynamic model closure and other hypothesis, and at the same time improve as much as possible the performance of the dispersion description, for example including effects not covered by the smoothed Eulerian fields.

The LPDM unresolved scale parameterization methods are the focus of this text. Here, the implementation of subgrid parameterizations in Lagrangian models using Dynamical Model outputs is discussed. The work will cover two different situations. In the first case the subgrid turbulence has well known features, namely it lies in the inertial subrange. In the second one, a LPDM is implemented on a general circulation model, in a case where accurate theoretical information for the model subgrid part are lacking. A substantial number of similar considerations can be applied to both the models.

This text is organized as follow: chapter 1 covers the physical basics and dynamic modelling information needed. Chapter 2 introduces elements of stochastic modelling. Chapter 3 describes the numerical methods used in the implementation. Then, chapters 4 and 5 describe in depth the model settings and approximations used and the experimental results, respectively. Conclusions are outlined in chapter 6.

Contents

Part I

Physics and Methods

Chapter 1

Characterization of turbulence in the atmosphere

1.1 Introduction

All flows of liquids and gases may be divided into laminar flows, and their opposite, turbulent flows in which the velocity, pressure, temperature and other fluid mechanical quantities fluctuate in a disordered manner with sharp space and time variations.

The ability of turbulent flows in the transfer of momentum, heat and admixtures is far greater with respect to their viscous counterpart.

In addition, it is found that in nature turbulent flows made up the most part of fluid motions, while viscous flows present themselves in limited conditions.

An appropriate description of turbulence is thus needed in order to predict atmospheric motion.

1.2 Basic equations, terminology and techniques

Atmosphere and ocean are treated under the assumptions of continuum dynamics[1]. From the conservation laws of mass, momentum and internal energy, it is possible to obtain the laws of fluid dynamics in differential form(Landau and Lifshitz, 1959). The conservation of mass is expressed throught the continuity equation:

$$\frac{\mathrm{d}\rho}{\mathrm{d}t} + \rho\frac{\partial u_i}{\partial x_i} = 0\,; \tag{1.1}$$

Where ρ is the density field and $\mathbf{u} = (u_1, u_2, u_3)$ is the Eulerian velocity field. Here, and throughout the whole text, we adopt the Einstein summation of repeated index convention. If ambiguity arises, the summation will be written explicitly.

The Navier-Stokes equation describes the conservation of momentum:

$$\rho\frac{\mathrm{d}u}{\mathrm{d}t} = \rho X_i - \frac{\partial p}{\partial x_i} + \frac{\partial}{\partial x_j}\left[\mu\left(\frac{\partial u_i}{\partial x_j} + \frac{\partial u_j}{\partial x_i}\right) - \frac{2}{3}\mu\frac{\partial u_k}{\partial x_k}\right]\;; \tag{1.2}$$

Where p is the pressure field and μ is the dynamic viscosity of the fluid. X_i represents the effects of volume forces. In usual atmospheric application, this term takes into account gravitational force as well as pseudoforces caused by the rotating frame of reference adopted for the NS equation on earth. Assuming the gravitational fields to be $\nabla\Phi = -g\mathbf{k}$, and denoting the earth rotation vector with Ω:

$$X_i = \rho g\delta_{i3} - 2\varepsilon_{lmi}\Omega_l u_m\;. \tag{1.3}$$

Finally, the conservation of internal energy is described by the thermodynamic equation:

$$c_v\frac{\mathrm{d}T}{\mathrm{d}t} + p\frac{1}{\rho^2}\frac{\mathrm{d}\rho}{\mathrm{d}t} = J\;. \tag{1.4}$$

where T is the temperature, J is the rate of heating due to radiation, conduction, and latent heat release.

---

[1] Because of the density of air in troposphere and ocean, the particle mean free path is short with respect to the scale of observations. Moreover, the large sample of molecules contained in a given volume assure that statistical variability in averaged quantities are negligible.

1.2.1 Approximate forms of the dynamic equations

Equations 1.1, 1.2 and 1.4 are general expressions that potentially describe any effect within the fluid dynamic paradigm. In many real problem, some semplification can be made.

Scaling analysis, or scaling, is a convenient technique for estimating the magnitudes of various terms in the governing equations for a particular type of motion. In scaling, typical expected values of the following quantities are specified:

1. Magnitudes of the field variables;
2. Amplitudes of fluctuations in the field variables;
3. Characteristic length, depth and time scales on which this fluctuations occur.

Once evaluated the weight of each term involved, terms of smaller order of magnitude are neglected. Fluctuation of similar magnitude can occur in motion systems of various space and time scales, and, as such, the nature of the dominant terms in the governing equation is dependent of the scale of motion.

Scaling in the synoptic scale

For example, when considering the vertical momentum equation with quantities p_0, f_0, ρ, H typical for the synoptic scale motion, the terms $\rho^{-1}\partial p/\partial x_3$ and g are many order of magnitude greater than the other involved in the equation. This scale analysis gives similar results also when considering horizontal fluctuation of density and pressure fields. This means that at those scale, to a high degree of accuracy, hydrostatic equlibrium holds.

Similar considerations on the continuity equation lead to the conclusion that, at this scale of motion and with respect to the basic state density profile $\rho_0(x_3)$, the mass flux is non-divergent:

$$\frac{\partial}{\partial x_k}(\rho_0 u_k) = 0\,. \tag{1.5}$$

Boundary layer typical scales

On the other hand, when considering a boundary layer with scales of motion of the order of the km, other terms can become dominant in the equations. There is a rather general approximation (in the lower atmosphere and ocean) that involve the density value and is called after Boussinesq.

The Boussinesq approximation treat ρ as constant in every term but the external forces one inside the equations of motion (Van der Hoven, 1957)^2.

One writes the density $\rho(\mathbf{x}, t)$ as:

$$\rho(\mathbf{x}, t) = \rho_{00} + \rho_0(x_3, t) + \rho'(\mathbf{x}, t)\,. \tag{1.6}$$

Adopting the Boussinesq approximation and considering the viscosity constant within the fluid, the Eq.s 1.1, 1.2 and 1.4 take the following forms:

$$\frac{\partial u_i}{\partial x_i} = 0\,, \tag{1.7}$$

$$\frac{\mathrm{d}u}{\mathrm{d}t} = X_i - \frac{1}{\rho_{00}}\frac{\partial p}{\partial x_i} + \nu\frac{\partial}{\partial x_j}\left[\left(\frac{\partial u_i}{\partial x_j} + \frac{\partial u_j}{\partial x_i}\right)\right]\,. \tag{1.8}$$

Here, $\nu = \mu/\rho$ is the kinematic viscosity.

A direct way to put forth the difference in magnitude in each term is the adimensionalization of the equation 1.2:

$$\frac{\mathrm{d}u_i}{\mathrm{d}t} = -\frac{\partial p}{\partial x_i} + \epsilon_{ij3}\mathrm{Ro}^{-1}u_j + \mathrm{Re}^{-1}\frac{\partial^2 u_i}{\partial x_j \partial x_j} + \delta_{i3}\mathrm{Fl}^{-2}\rho\,, \tag{1.9}$$

where all the variable are considered adimensionalized. Re, Ro and Fl are parameters that express the magnitude of each term, and thus characterize the motion. If U, L are the characteristic scales of velocity and length, and $f = 2\Omega_3\ \mathrm{sen}(\varphi)$, where φ is the latitude, then the characteristic numbers are defined as:

$$\mathrm{Re} = \frac{UL}{\nu}\,, \tag{1.10}$$

$$\mathrm{Ro} = \frac{U}{fL}\,, \tag{1.11}$$

$$\mathrm{Fl} = \frac{U}{NL}\,, \tag{1.12}$$

---

[2] Given the small coefficient of volume of espansion of most fluids, for temperature variations not exceeding $10K$, the variation in the density are at most of 1%. The only exception is represented by the term ρX_i, because the acceleration resulting from $\delta\rho X_i$ can be quite large(Chandrasekar, 1961).

where N is the Brünt-Vaisala frequency:

$$N = \left(-\frac{g}{\rho_{00}} \frac{\mathrm{d}\rho_0}{\mathrm{dx}_3} \right)^{1/2} \quad . \tag{1.13}$$

Typical values in the planetary boundary layer are $\mathrm{Re} \approx 10^9$, $\mathrm{Ro} \approx 10^2$ and $\mathrm{Fl} \approx 1$.

1.3 Turbulence

In the earth system, both the motions of air, from small scale breeze to general atmospheric circulation, and the motions of water in oceans and rivers, are turbulent flows. Atmospheric turbulence play a fundamental role in the transfer of heat and moisture by air masses, in evaporation from the surface of land or water, and in thermal and dynamic interaction between the atmosphere and underlying surface which has a considerable effect on changes in the weather. Atmospheric turbulence is responsible for the spreading of admixtures in the air, the production of wind waves and wind currents in the ocean, and also for turbulent fluctuations in refractive index that can affect significantly the propagation of light and radio waves from terrestrial and cosmic sources.

The motion of any continuous medium can be described by and infinite number of generalized coordinates. For laminar motions, these coordinates are chosen in such a way that only a few of the corresponding degrees of freedom will actually take part in the motion. However, in case of turbulent motion, a large number of degrees of freedom are always excited, and hence the variation with time of any physical value will be described here by functions containing a huge number of Fourier components, i.e., by functions of an extremely complicated nature. Therefore, in this case it is practically hopeless to attempt to describe the individual time variations of all the generalized coordinates corresponding to the excited degrees of freedom (i.e., to find a mathematical expression for the time-dependence of the fields of velocity, pressure, etc., of a single individual flow). The only possibility in the theory of turbulence is a statistical description, based on the study of specific statistical laws, with validity for large ensemble of similar objects. Thus, a turbulence theory is, by the nature of turbulence itself, strictly related to the statistical mechanics(Monin and Yaglom, 1971, 1975).

In other words, in a turbulent flow, an individual description of velocity, temperature and other characteristic is both impossible and unuseful. In fact, the irregular and highly variable nature of all of these individual fields eliminates the possibility of using exact values of them in any practical problem.

The inertial forces which produces mixing of the different volumes of fluid moving inertially with different velocities also produce a transfer of energy from large to small scale components of motion and hence assist the formation in the flow of sharp, small scale inhomogeneities that characterize a turbulent flow. The viscous forces, on the contrary, assist in the smoothing out of small scale inhomogeneities.

1.3.1 Reynolds Averaging

The first attempt in the describtion of turbulence in modern physics is due to the work of Osborne Reynolds. Among its theory, two concepts have remained almost unchanged in the following works.

On one hand, Reynolds defined a general criterion for dynamic similarity of flows of a viscous, incompressible fluid. The so-called Reynolds number, defined by the characteristic scale of velocity and length of a particular flow and the viscosity of the fluid. From a dynamical viewpoint, the Reynolds number (Eq. 1.10) may be interpreted as the ratio of typical values of the inertial and viscous forces acting within the fluid. Flows with sufficiently large Reynolds number will be turbulent, while flows in which Reynolds number is low will be laminar.

On the other hand, Reynolds also introduced a technique still in use in the majority of turbulence problems, namely the separation of turbulent fields in averaged and fluctuating parts. In the present day theory of turbulence, it is always implied that the fluid mechanical fields of a turbulent flow are random fields in the sense of probability theory (see Appendix).

Given the velocity fields $\mathbf{u}(\mathbf{x}, t)$, and given the phase space of turbulent flows, $\Omega\{\omega\}$, where the points ω represent all the possible vector fields $\mathbf{u}(\mathbf{x}, t)$ which satisfy the equations of fluid mechanics and the boundary conditions of the flow, the problem of turbulence is reduced to finding the probability distribution $P(\omega)$ in the phase space Ω.

The determination of $P(\omega)$ is a difficult task, and the general problem has not been solved yet. In most practical cases, anyway, is sufficient to determine only some of the simplest numerical characteristics of the probability distribution of a given turbulent flow. Those characteristics usually are the single or multiple point moments of a given set of fields.

The fluid dynamic fields are written as an averaged component (ensemble mean averaged) and a fluctuating component, whose average is 0:

$$\phi = \langle\phi\rangle + \phi' \,, \tag{1.14}$$

where ϕ can be u_i, θ, p, ρ or a generic scalar field variable χ.

By substituting with the Expression 1.14 in the Navier-Stokes equations, Eq. 1.2, and averaging, one can obtain the Reynolds momentum equations.

$$\frac{\mathrm{d}\langle u_i\rangle}{\mathrm{d}t} = -\frac{1}{\rho}\frac{\partial\langle p\rangle}{\partial x_i} + \langle X_i\rangle + \nu\frac{\partial^2\langle u_i\rangle}{\partial x_j \partial x_j} + \frac{\partial\langle u'_i u'_j\rangle}{\partial x_j} \,. \tag{1.15}$$

In the deduction of Eq. 1.15, the properties of linearity and commutativity of the average operation with the derivation has been used.

A method for obatining the complete set of differential equation for moments of $P(\omega)$ has been first proposed by kel (1924). The system of equation is very complicated, and any finite subsystem of these equation is nonclosed. We report the expression for the second order averaged momentum equation

$$\frac{\mathrm{d}}{\mathrm{d}t}\langle u_i u_k\rangle = \mathcal{S} + \mathcal{T} + \mathcal{B} + \mathcal{C} + \mathcal{P} + \mathcal{D} \,, \tag{1.16}$$

where:

$$\mathcal{S} = -\langle u_i' u_j' \rangle \frac{\partial \langle u_k \rangle}{\partial x_j} - \langle u_k' u_j' \rangle \frac{\partial \langle u_i \rangle}{\partial x_j} \, , \tag{1.17}$$

$$\mathcal{T} = -\frac{\partial \langle u_i' u_j' u_k' \rangle}{\partial x_j} \, , \tag{1.18}$$

$$\mathcal{B} = -\frac{g}{\rho_{00}} (\delta_{k3} \langle u_i' \rho' \rangle + \delta_{i3} \langle u_k' \rho' \rangle) \, , \tag{1.19}$$

$$\mathcal{C} = f(\varepsilon_{kj3} \langle u_i' u_j' \rangle + \varepsilon_{ij3} \langle u_k' u_j' \rangle) \, , \tag{1.20}$$

$$\mathcal{P} = -\frac{1}{\rho_{00}} \left(\left\langle u_k' \frac{\partial p'}{\partial x_i} \right\rangle + \left\langle u_i' \frac{\partial p'}{\partial x_k} \right\rangle \right) \, , \tag{1.21}$$

$$\mathcal{D} = \nu \left(\frac{\partial^2}{\partial x_j^2} \langle u_k' u_i' \rangle - 2 \left\langle \frac{\partial u_i'}{\partial x_j} \frac{\partial u_k'}{\partial x_j} \right\rangle \right) \, . \tag{1.22}$$

Here, the term $\mathcal{T}$ is a third order moment (the problem is not closed) The first term of $\mathcal{D}$ describes the diffusion of second order moments, and is small with respect to the second term of $\mathcal{D}$ in flows with high Reynolds numbers. The second term, which represents the correlation of the first derivative of velocity fluctuations, for small scales of motion is diagonal and takes the form:

$$2\nu \left\langle \frac{\partial u_i}{\partial x_j} \frac{\partial u_k}{\partial x_j} \right\rangle = \frac{2}{3} \delta_{ik} \varepsilon \tag{1.23}$$

where ε is the molecular dissipation.

Diffusive closure for the Reynolds tensor

The traditional approach to the closure problem is to assume that turbulent eddies act similarly to molecular diffusion so that the the flux of a field is proportional to the local gradient of the mean. This means writing, for the velocity:

$$\langle u_i' u_j' \rangle = -K_{mij} \frac{\partial \langle u_i \rangle}{\partial x_j} \, , \tag{1.24}$$

and, for a scalar quantity χ:

$$\langle u_i' \chi' \rangle = -K_{\chi i} \frac{\partial \langle \chi \rangle}{\partial x_i} \, . \tag{1.25}$$

$K_{m\ ij}$ is calle *eddy viscosity* and, when $\chi \equiv \theta$, $K_{\chi i} \equiv K_{hi}$ is the eddy diffusivity of heat. This closure scheme is usually referred to as K-theory.

The K-Theory has many limitations. The eddy viscosities depend on the flow rather than the properties of the fluid. The determination of the value of the diffusion coefficient thus cannot be easily measured and can vary for different conditions for the same fluid. The K-theory approximation also fails completely when the most energetic eddies have size comparable with the boundary layer height. In that case, neither the momentum flux or flux of a scalar are proportional to the local gradient of the mean.

A simple model for estimating the value of diffusion coefficient has been initially proposed by (Prandtl, 1925). The fundamental hypothesis of that model assumes that a parcel of fluid carrying the mean properties of the original level is displaced of the characteristic distance l' and then it will mix with its surrounding. The hypothesis is referred to as the 'mixing length hypothesis'. It is also postulated that the parcel then will create a fluctuation whose magnitude is proportional to the local gradient of the mean field and the displacement l' itself. In formulas, for the velocity and scalar quantities

$$u_i' = -l_j' \frac{\partial \langle u_i \rangle}{\partial x_j} \tag{1.26}$$

$$\chi' = -l_j' \frac{\partial \langle \chi \rangle}{\partial x_j} \tag{1.27}$$

It should be noted that $l' > 0$ describe a displacement toward the increase of the Cartesian coordinate x_j and vice-versa. Making the mixing length hypothesis is similar to assume that the particles behave as a molecule travelling along its mean free path.

Also, the flow $\mathbf{J}_m$, $\mathbf{J}_\chi$ of the quantities will be:

$$J_{mij} = \rho \langle l_j u_j' \rangle \frac{\partial \langle u_i \rangle}{\partial x_j} \tag{1.28}$$

$$J_{\chi j} = \rho \langle l_j u_j' \rangle \frac{\partial \langle \chi \rangle}{\partial x_j} \tag{1.29}$$

In the 3-dimensional case, K is a fourth-rank tensor (Monin and Yaglom, 1971):

$$K_{ij\alpha\beta} = \frac{1}{2} \left(\mathfrak{K}_{i\alpha} \delta_{j\beta} + \mathfrak{K}_{j\alpha} \delta_{i\beta} \right) \,, \tag{1.30}$$

where:

$$\mathfrak{K}_{ij} = \sqrt{\frac{1}{2} \langle u_\gamma^2 \rangle} \; l_{ij} \,. \tag{1.31}$$

Here l is a second-rank tensor, because of anisotropy. In the one-dimensional case, the above expression becomes:

$$K = \langle l^2 \rangle \left| \frac{\partial \langle u \rangle}{\partial x} \right| , \tag{1.32}$$

where l is called mixing length.

1.3.2 Homogeneous and Isotropic Turbulence

The previous theory used assumption that are not derived from the equations of fluid mechanics. It is what is called a *semi-empirical* theory of turbulence. This kind of theory concentrates mainly on effects on the large scale of motion, in many practical cases it can predict the quantity of interest of with good accuracy, but do not provide a deep understanting of the physical nature of turbulence.

The theory of 'the universal steady statistical regime of the small scale compontents of turbulence for very high Reynolds numbers' is developed starting from few general assumption and has been proved to be very predictive on some physical features of turbulence.

The development of this theory can be traced back to the works of Richardson (1926), Taylor (1935) and Kolmogorov (1941).

In the theory first stated from Richardson, the physical mechanism of developed turbulence is the existence of a hierarchy of disturbances in the flow (eddies) of various order. The higher order, small scale disturbances predates on the energy of lower order, large ones. This creates a transfer of energy from large to small disturbances, up to the limit at which the Reynolds number become sufficiently small and the viscous forces dissipates kinetic energy into heat.

The length scales at which the dissipation become important are of the order of several millimeters in typical air and water turbulent flows[3].

The theory is mainly based on the concept of homogeneous and isotropic turbulence. This is similar to the requirements that all the finite dimensional probability density

---

[3] This length is still many order of magnitude greater than the mean free path of the molecules, so for regular geophysical flow the continuum mechanics still can be applied.

functions of the fluid dynamical quantities at a finite number of space-time points are invariant under any shift, rotation and reflection operations.

Under the assumption that this regime can be obtained in every flow with sufficiently high Reynolds number for sufficiently small scale of motions, the Kolmogorov theory (hereinafter K41 theory) is based on two main assumption

- In such conditions, the statistical regime will be universal and determined by only two dimensional parameters, namely the coefficient of viscosity ν and the mean rate of dissipation of energy, $\langle\epsilon\rangle$. This assumption introduces a length-scale at which the viscous forces still exerts a considerable effects on the motion. The scale is known as Kolmogorov scale and is defined as:

$$\eta = \left(\frac{\nu^3}{\langle\epsilon\rangle}\right)^{1/4} , \tag{1.33}$$

- It exists a range of scales, larger than the Kolmogorov scale η and much smatter of the length scale of the flow L, in which the viscosity do not play any part and the statistical regime is determined only by $\langle\epsilon\rangle$.

Within the relevant deduction of this theory, we list the expression for the second order Lagrangian and Eulerian structure functions $D^{(2)}(t)$ and $D^{(2)}(t)$:

$$D^{(2)}(t) = 2(\langle u^2\rangle - R(t)) = C_0\varepsilon t\,, \tag{1.34}$$

$$D^{(2)}(t) = 2(\langle u^2\rangle - R(r)) = C_K\varepsilon^{2/3}r^{2/3}\,. \tag{1.35}$$

Where ε is the molecular dissipation, C_0 and C_K are constants, and $R(t)$, $R(r)$ are the velocity correlation functions. Different values have been attributed to C_0 and C_K. In recent works, their values is set as $C_0 = 6.2$ $C_K = 2.0$ (Ouellette et al., 2006).

In the inertial subrange, the Lagrangian and Eulerian velocity spectra take the form:

$$E(\omega) = \frac{\Gamma(2)sin(\pi/2)}{\pi}C_0\varepsilon\omega^{-2}\,, \tag{1.36}$$

$$E(k) = \frac{\Gamma(5/3)sin(\pi/3)}{\pi}C_K\varepsilon^{2/3}k^{-5/3}\,, \tag{1.37}$$

where k and ω are the wavenumber and frequency, respectively.

A model for Lagrangian correlation is proposed by Gifford (1982):

$$R(t) = \langle u^2 \rangle \exp\left(\frac{t}{T_L}\right) , \tag{1.38}$$

which implies a relationship between the Lagrangian Timescale T_L and $C_0\varepsilon$ of the form:

$$\varepsilon = \frac{2\langle u^2 \rangle}{C_0 T_L} . \tag{1.39}$$

Concerning the Eulerian velocity correlation function, Durbin (1980) suggests:

$$R(r) = \langle u^2 \rangle \left[1 - \left(\frac{r^2}{r^2 + L_E^2} \right)^{1/3} \right] . \tag{1.40}$$

In the expression, L_E is the Eulerian lengthscale

1.4 The Boundary Layer(s)

The viscous sublayer is only few millimeter high, but has the indirect effect of reducing the flow velocity to 0 at the surface. This no-slip condition causes strong velocity shear near the surface, which lead to the development of turbulent eddies. These effects, with the addition of turbulent eddy formation due to the buoyancy, give rise to a layer whose height varies from tenth of meters (for strong stable conditions) to few kilometers over the surface. This layer is referred to as *Planetary Boundary Layer*.

As expected, as interface between the fluid and its boundaries, the characteristics of the latter have strong influence on the PBL. Dishomogeneities, roughness and obstacles lead to sensible modification in the flow. In particular, the ratio between the buoyancy production and the wind shear at the surface is of paramount importance for the description of the boundary layer features.

Based on dimensional consideration, a limited number of parameters characterize the turbulence generated. A measure of the relative effects of combined heat and momentum fluxes is given by the Richardson flux number:

$$\mathcal{R}_f = \frac{g/\theta_{00} \langle u_3' \theta' \rangle}{\langle u_h' u_3' \rangle \mathrm{d}\langle u \rangle / \mathrm{d}x_3} , \tag{1.41}$$

where u_h is a velocity representative of the horizontal components, θ is the potential temperature and θ_{00} is the reference value of the potential temperature, defined similarly to eq. 1.6. Buoyancy effects can produce turbulence if $\langle u_3'\theta'\rangle > 0$ ($\mathcal{R}_f < 0$) or inhibite it if, viceversa, $\langle u_3'\theta'\rangle < 0$ (Experimentally, stable stratification correspond to $\mathcal{R}_f > 0.2$).

$\mathcal{R}_f \approx 0$ means that the turbulence production is completely due to the wind shear. This condition is called neutral stratification. In this case the turbulent flux near the ground is constant and gives a definition for the scaling parameter known as friction velocity, u_*:

$$-\langle u'u_3'\rangle = u_*^2\,. \tag{1.42}$$

The profile of the average velocity in this condition is logarithmical, and the eddy diffusion coefficient has the form:

$$K_m = \kappa u_* z\,. \tag{1.43}$$

If characteristic quantities can be defined in global terms in a PBL flow, a length scale can be introduced:

$$L_{MO} \frac{u_*^3}{\kappa g \langle u_3'\theta'\rangle/\theta_{00}}\,. \tag{1.44}$$

$|L_{MO}| \to \infty$ describes the neutral boundary layer. For $L_{MO} > 0$ the boundary layer is stable. This boundary layer is characterized from a suppression of turbulence and the presence of internal gravity waves.

$L_{MO} < 0$ implies a buoyancy production of turbulence. A Convective Bounary Layer is characterized by stronge vertical transport due to eddies. The presence of thin, strong uprising currents (thermals) and large, slow descending ones, causes the Pdf of the velocity to be strongly skewed. To adequately describe the CBL, the vertical and horizontal scales have to be considered separately. A scaling parameter for the vertical motion is the convective velocity scale w_*, defined as:

$$w_* = \left(\frac{g}{\theta_{00}\langle u_3'\theta' h_i\rangle}\right)^{1/3}\,, \tag{1.45}$$

where h_i is the CBL height.

For additional information about PBL structure, see for example Stull (1988).

1.5 Dispersion of fluid particles

After introducing an admixture in a turbulen flow, it is rapidly trasported in disordered intermixed filaments and rapidly spreads until it is homogeneously mixed in the whole volume of the fluid.

This phenomenon is one of the fundamental properties of turbulent flows and it mixes particle many order of magnitude more efficiently than the molecular diffusion. The spread of plant pollen, industrial pollutants, bacteria and viruses, radioactive isotopes, sea salt and desert sand are all driven by turbulent dispersion.

The problem of turbulent dispersion has been studied extensively, starting from the works of Taylor (1921), with experiments both from laboratory and atmosphere.

In this section, a short introduction on theory of turbulent dispersion of fluid particles is given. All the results refer to particles that are assumed to be indistinguishable from the fluid particles in their surroundings (i.e., are fluid particle tracers).

1.5.1 Absolute dispersion

Let us consider a set of independent particles (i.e. each particle belonging to a different realization of the flow). In steady condition particles move independently from each other if they are released from the same point $\mathbf{x}_0$ at time intervals larger than the correlation time T_{Lij}. As reported by the work of Taylor (1921), for such a set of particles the relation for the position variance reads:

$$\langle x_i x_j \rangle = 2\langle u'_i u'_j \rangle \left\{ T_{Lij} t - T_{Lij}^2 \left[1 - \exp\left(-\frac{t}{T_{Lij}} \right) \right] \right\}. \tag{1.46}$$

It follows easily from the equation (1.46) for $t << T_{ij}$ that:

$$\langle x_i x_j \rangle \simeq \langle u'_i u'_j \rangle \left\{ t^2 - \frac{t^3}{3T_{Lij}} \right\}, \tag{1.47}$$

that is called ballistic regime. Note that this is true if the particles are inserted in equilibrium with the flow, and $\langle v_i(0) v_j(0) \rangle = \langle u'_i u'_j \rangle$.

For $t >> T_{Lij}$, eq. (1.46) is reduced to:

$$\langle x_i x_j \rangle \simeq 2T_{Lij} \langle u'_i u'_j \rangle t\,, \tag{1.48}$$

called diffusion regime. Now, it is possible to define the eddy-diffusion coefficient (computed as a limit) as:

$$D_{ij} = \langle u_i' u_j' \rangle T_{Lij} \,. \tag{1.49}$$

It is thus expected for particles' mean square distance from the initial position to show a quadratic growth initially, and, for large time, to manifest a linear growth.

1.5.2 Relative dispersion

Another property of interest of the turbulent dispersion pertains to the evolution of the mean square separation of a pair of "marked particles" which starts at the time t_0 at a certain distance l_0 in the flow (l_0 supposed to belong to the inertial range).
When $t < t_{l_0}$, where t_{l_0} is the characteristic time for eddies of the size of the source, $t_{l_0} \simeq l_0 / \langle \Delta v^2(l_0) \rangle \approx \epsilon^{-1/3} l_0^{2/3}$, it is possible to show that, under the assumption that at times t the velocity difference is dominated by the vortices of scale l_0:

$$\langle (l - l_0)^2 \rangle \simeq \langle \Delta v^2(t_0) \rangle t^2 \,, \tag{1.50}$$

where $\langle \Delta v^2(\tau_0) \rangle$ is the mean square Lagrangian velocity difference at the starting time t_0.

For times larger than t_{l_0} but smaller than T (integral time scale), instead it is:

$$\langle (l - l_0)^2 \rangle \simeq g \epsilon t^3 \,. \tag{1.51}$$

This is also known as Richardson's law (Richardson (1926)), and recent evaluation for the Richardson's constant g suggest $g = 0.6$ Sawford (2008).
Finally, for $t \gg T$:

$$\langle (l - l_0)^2 \rangle \simeq 4 \langle u^2 \rangle T_L t \,. \tag{1.52}$$

In order that the diffusion regime can occur, it is necessary the presence of both the Eulerian and Lagrangian independence (i.e., both time and space interval sufficiently long).

Relative motions of distribution of particles

Let $N(\mathbf{x}, t)$ be the tracer distribution for a single realization of the flow. The total of particle is:

$$Q = \int \mathrm{d}\mathbf{x} N(\mathbf{x}, t) \tag{1.53}$$

and the position of their center of mass is:

$$\mathbf{c} = \frac{1}{Q} \int \mathrm{d}\mathbf{x}\ \mathbf{x} N(\mathbf{x}, t) \,. \tag{1.54}$$

In many problems, one can be interested in the dispersion of particles around their center of mass. Define $\mathbf{y}$ as the particle position with respect to the reference frame moving with $\mathbf{c}$, $\mathbf{y} = \mathbf{x} - \mathbf{c}$.

It can be proven that the absolute dispersion $\langle x_i x_j \rangle$ can be written as:

$$\langle x_i x_j \rangle = \langle c_i c_j \rangle + \langle y_i y_j \rangle \,, \tag{1.55}$$

where $\langle c_i c_j \rangle$ is called meandering(Csanady, 1973).

For the meandering, in homogeneous turbulence the following relationship holds:

$$\langle c_i^2 \rangle = \langle u_i^2 \rangle t \,, \qquad t \ll T_L \,; \tag{1.56}$$

$$\frac{\mathrm{d}\langle c_i^2 \rangle}{\mathrm{d}t} = 0 \,, \qquad t \gg T_L . \tag{1.57}$$

1.6 Turbulence Closure in Large Eddy Simulations

In a Large Eddy Simulation, the small scales of motion are removed by means of a filtering in the velocity spectrum.

This operation is usually theoretically described as (but this operation is actually done in some numerical implementations) the filtering of the velocity field by convolution with a kernel $G(\mathbf{x}, t)$.

The goal is to obtain an expression derived from the NS equation describing only large scale motion.

1.6.1 Scale Filtering

The LES scheme is based on the concept of filtering out the small scales of motion from the dynamic equations.

For a given original field ψ, the filtered field $\tilde{\psi}$ is written as the convolution of ψ with the filter $G(\mathbf{x}, t)$

$$\widetilde{\psi}(\mathbf{x}, t) = \int_{-\infty}^{+\infty} \mathrm{d}t' \int_{-\infty}^{+\infty} \mathrm{d}^3\mathbf{x}' G(\mathbf{x} - \mathbf{x}', t - t')\ \psi(\mathbf{x}', t')\mathrm{d}\mathbf{x}' \tag{1.58}$$

Since the filtering operation has to be easily used to manipulate NS equations, it is required that any filter G verify the following fundamental properties (Sagaut, 1998):

1. Linearity. Given the generic fields ψ, ϕ and constants α, β:
$$\widetilde{\alpha\psi + \beta\phi} = \alpha\widetilde{\psi} + \beta\widetilde{\phi}\,. \tag{1.59}$$
2. Conservation of constants. Given a constant α:
$$\tilde{\alpha} = \alpha \Longleftrightarrow \int_{-\infty}^{+\infty} \int_{-\infty}^{+\infty} G(\mathbf{x}, t)\mathrm{d}^3\mathbf{x}\mathrm{d}t = 1\,. \tag{1.60}$$
3. Commutation with derivation. Given $s = x_i, t$ and a field ψ:
$$\widetilde{\frac{\partial\psi}{\partial s}} = \frac{\partial\tilde{\psi}}{\partial s}\,. \tag{1.61}$$

The spatial filtering is the most used technique to obtain scale separation separation, so from now on we will limit our treatise only to them, adopting the notation:

$$G(\mathbf{x}, t) \longrightarrow G_\Delta(\mathbf{x}) \tag{1.62}$$

The considerations that follow remain the same also for time filtering. For an exhaustive treatise of causal filters refer for example to Sagaut (1998) and Pruett (2000).

Most common filters are the top-hat filter, the spectral cutoff filter and the Gaussian filter.

The top-hat (box) filter is defined as:

$$G_\Delta^{box}(\mathbf{x}) = \begin{cases} \Delta^{-3} & , \quad |x_k| < \Delta/2, \\ 0 & , \quad |x_k| \geq \Delta/2. \end{cases} \tag{1.63}$$

It is equivalent to a volume local mean, and, as such, has a good spatial localization but, because of spectral overlap, it not allows an unambiguous separation of scales of motion.

On the other hand, the box filter spectral space counterpart, the sharp spectral cutoff filter,

$$G_{\Delta}^{sp} = \Pi_{k=1}^{3} \frac{\sin(\pi x_k/\Delta)}{\pi x_k}, \tag{1.64}$$

clearly separates between the scales, but it is non-local (causing oscillatory behavior in fields around an isolated feature of the field).

The Gaussian filter:

$$G_{\Delta}^{gauss} = (6/\pi)^{3/2} \frac{1}{\Delta^3} \exp\left(-\frac{6x^2}{\Delta^2}\right), \tag{1.65}$$

has localization properties that are intermediate between the box filter and the sharp spectral filter, and it is usually preferred in most practical applications.

1.6.2 Filtered Navier Stokes equations

Applying the filtering operations to the Navier Stokes (Eq. 1.2) and continuity equations (Eq. 1.1), neglecting effects of rotation restricting the case to incompressible fluid, given the filter properties of linearity and commutation with derivative, one obtains (Pope, 2000):

$$\frac{\partial \widetilde{u_i}}{\partial t} + \frac{\partial}{\partial x_j}(\widetilde{u_i\, u_j}) = -\frac{1}{\rho}\frac{\partial \tilde{p}}{\partial x_i} + \nu \frac{\partial}{\partial x_j}\left(\frac{\partial \widetilde{u_i}}{\partial x_j} + \frac{\partial \widetilde{u_j}}{\partial x_i}\right) \quad , \tag{1.66}$$

$$\frac{\partial \widetilde{u_i}}{\partial x_i} = 0 \quad . \tag{1.67}$$

In order to express Eq. 1.66 in terms of the filtered velocity field $\tilde{\mathbf{u}}$ only, Leonard (1975) applies the following transformation (Leonard's decomposition): First $\widetilde{u_i\, u_j}$ is rewritten considering the velocity field component as the sum of the filtered and subfiltered part $u_i = \widetilde{u_i} + u_i^s$.

$$\widetilde{u_i\, u_j} = \widetilde{\widetilde{u_i}\, \widetilde{u_j}} + \widetilde{\widetilde{u_i}\, u_j^s} + \widetilde{\widetilde{u_j}\, u_i^s} + \widetilde{u_i^s u_j^s} \quad . \tag{1.68}$$

After the first substitution in eq. 1.66, a second one follows:

$$\widetilde{\widetilde{u}_i\ \widetilde{u}_j} = (\widetilde{\widetilde{u}_i\widetilde{u}_j} - \widetilde{u}_i\widetilde{u}_j) + \widetilde{u}_i\widetilde{u}_j\,. \tag{1.69}$$

The Navier-Stokes equations obtained after this operation take the form (using the continuity equation for an incompressible fluid):

$$\frac{\partial \tilde{u}_i}{\partial t} + \tilde{u}_j \frac{\partial u_i}{\partial x_j} = -\frac{1}{\rho}\frac{\partial \widetilde{p}}{\partial x_i} + \nu\,\frac{\partial}{\partial x_j}\left(\frac{\partial \widetilde{u}_i}{\partial x_j} + \frac{\partial \widetilde{u}_j}{\partial x_i}\right) - \frac{\partial \tau_{ij}^{\Delta}}{\partial x_j}\quad . \tag{1.70}$$

And τ^{Δ}, the so-called subgrid-scale(SGS) stress tensor is defined as:

$$\tau_{ij}^{\Delta} = \widetilde{u_i u_j} - \tilde{u}_i\tilde{u}_j\,. \tag{1.71}$$

The stress tensor τ^{Δ} takes into account the effects of the interaction between subgrid scales (similarly to the Reynolds stress tensor for the for the fluctuating component of the velocity field), between subgrid and filtered scales, and between the the filtered scales.

Equation 1.70 can be numerically solved with a spatial resolution of order of Δ, allowing a computational cost which is more affordable than in DNS simulations.

The effects of subgrid scale fields is now limited to the choice of the an expression for τ^{Δ}, which will provide a closure for the dynamical Equation 1.70.

1.6.3 SGS stress models

As one can expect, any affordable model for the SGS stress is bound to neglect some features of the real velocity field.

Even if τ^{Δ} (Eq. 1.71) has the same form of the Reynolds stress tensor, the SGS tensor is a fluctuating stochastic variable in nature. Moreover, similarly to the Reynolds stress tensor case, an expression for τ^{Δ} has to be chosen in order to integrate the filtered equation of motion.

Eddy viscosity models

Eddy viscosity models adopt the following closure for the deviatoric part of the SGS stress tensor, i.e. $\tau_{ij}^{\Delta} - 1/3\tau_{kk}^{\Delta}\delta_{ij}$:

$$\tau_{ij}^{\Delta,ev} = -2\nu_T \widetilde{S}_{ij}\,, \tag{1.72}$$

where:

$$\widetilde{S}_{ij} = \frac{1}{2}\left(\frac{\partial \widetilde{u}_i}{\partial x_j} + \frac{\partial \widetilde{u}_j}{\partial x_i}\right) \quad , \tag{1.73}$$

is the strain rate tensor and ν_T is called scalar eddy viscosity.

This is the simplest and most economical closure possible for the dynamic equation, but its major drawback comes from its definition itself, when comparing viscous effects and turbulence. In the case of molecular viscosity, if the control volume is large compared with the mean free path and the macroscopic shear is low compared with the inverse collision times, the relationship between the stress and shear should be deterministic and linear with very good approximation.

On the other hand, in turbulence, such a separation in length and timescale do not exist. So one can expect that, for an individual realization of the flow, the proper physics of SGS turbulence is not captured by the model (Meneveau and Katz, 2000; Clark et al., 1979; Liu et al., 1994).

The classical formulation of this type of model, known as Smagorinsky model, defines the eddy viscosity as (Smagorinsky, 1963; Lilly, 1966):

$$\nu_T = (c_S^{\Delta}\Delta)|\widetilde{S}|\,, \tag{1.74}$$

where Δ is a length scale and $\Delta|\widetilde{S}|$ is the velocity difference relative to the scale Δ, with $|\widetilde{S}| \equiv (2\ \widetilde{S}_{ij}\widetilde{S}_{ij})^{-1/2}$ (Deardorff, 1974; Scotti et al., 1993).

An interesting variant of the Smagorinsky filter is represented by the so-called kinetic energy model. In that model, an additional equation for the kinetic energy $e = 1/2\tau_{ii}^{\Delta}$ is solved, and the eddy viscosity is written as a function of e and Δ:

$$\nu_T = C_e e^{1/2}\Delta\,, \tag{1.75}$$

with $C_e = 0.1$ (Weil et al., 2004). This approach, firstly proposed by Schumann (1975), incorporates memory effects and has been popular in simulations of atmospheric flows (Moeng, 1984; Shaw and Schumann, 1992).

In the kinetic energy model, the turbulence dissipation rate ε is usually parametrized by:

$$\varepsilon = C_\epsilon \frac{e_S^{3/2}}{\mathfrak{l}} \,, \tag{1.76}$$

with $C_\epsilon = 0.93$ and the value of $\mathfrak{l}$ which varies if the conditions are neutral or unstable:

$$\mathfrak{l} = \Delta \,, \tag{1.77}$$

where Δ is the grid spacing. In case of different grid spacing in 3-D model, Δ is defined as:

$$\Delta = \left(\alpha_\Delta \prod_i \Delta_{xi} \right)^{1/3} \,. \tag{1.78}$$

Here, $\alpha_\Delta = (3/2)^2$ is included by Weil et al. (2004) to take into account dealiasing. For stable cases:

$$\mathfrak{l} = \min(\Delta, \mathfrak{l}_{st}) \tag{1.79}$$

and:

$$\mathfrak{l}_{st} = \frac{0.7 e_S^{1/2}}{[g/\Theta_0 \partial\theta_r/\partial x_3]^{1/2}} \,. \tag{1.80}$$

For an exhaustive treatment of scale separating filters, see Pope (2000), Sagaut (1998) and Meneveau and Katz (2000).

Chapter 2

Lagrangian modelling of unresolved motion

2.1 Stochastic models

With its simple implementation, great generality, intuitive concepts and strong statistical and mathematical background formulation, stochastic modelling represent a widespread and powerful technique adopted in many fields of quantitative sciences.

When considering systems with a large number of degrees of freedom (such as molecular dynamics) and/or strong nonlinearity (i.e. chaos dynamics), stochastic model do not aim to the deterministic description of a phenomenon, but to obtain a set of realizations extracted from a probability density function with features as similar as possible to the PdF of the problem varables.

Applications span from quantum physics and chaos dynamics to economics and social sciences, passing throught chemistry, biology, and, as expected, turbulence modelling.

The basic concept behind a stochastic model, it goes without saying, is the definition of a stochastic process. A simple definition for a stochasic process is that of a system which evolves in time in which stochastic variables appear.

Given a set of stochastic variable values $\mathbf{x}_i \in \Omega$ at times $t_i \in I$, with Ω and I respectively the space of all possible event $\mathbf{x}$ and the time interval, to describe the stochastic process in the interval I means to find the joint probability density:

$$p \equiv p(\mathbf{x}_1, t_1; \mathbf{x}_2, t_2; ...)\,, \tag{2.1}$$

for each set of $(\mathbf{x}_i, t_i) \in (\Omega, I)$ (Gardiner, 1990).

2.1.1 Markov processes

Consider a succession of events. Under the hypothesis that:

$$t_1 \geq t_2 \geq ... \geq \tau_1 \geq \tau_2 \geq ... \,. \tag{2.2}$$

Given $\mathbf{x}_1, t_1; \mathbf{x}_2, t_2; ...; \mathbf{y}_1, \tau_1; ...$ the states of the system at subsequent times. Eq. 2.1 can be written in terms of conditional probability densities:

$$p(\mathbf{x}_1, t_1; \mathbf{x}_2, t_2; ...; \mathbf{y}_1, \tau_1, \mathbf{y}_2, \tau_2, ...) = \frac{p(\mathbf{x}_1, t_1; \mathbf{x}_2, t_2; ...|\mathbf{y}_1, \tau_1, \mathbf{y}_2, \tau_2, ...)}{p(\mathbf{y}_1, \tau_1; \mathbf{y}_2, \tau_2; ...)}\,. \tag{2.3}$$

A stochastic process is said to be a Markov process if its conditional probability only depends on the knowledge of the most recent condition:

$$p(\mathbf{x}_1, t_1; \mathbf{x}_2, t_2; ...|\mathbf{y}_1, \tau_1, \mathbf{y}_2, \tau_2, ...) = p(\mathbf{x}_1, t_1; \mathbf{x}_2, t_2; ...|\mathbf{y}_1, \tau_1)\,. \tag{2.4}$$

The Eq. 2.4 is called Markov assumption. The Markov assumption implies that, given $t_1 \geq t_2 \geq ... \geq t_n$:

$$p(\mathbf{x}_1, t_1; \mathbf{x}_2, t_2; ...; \mathbf{x}_n, t_n) = p(\mathbf{x}_1, t_1|\mathbf{x}_2, t_2) p(\mathbf{x}_2, t_2|\mathbf{x}_3, t_3)\ ...\ p(\mathbf{x}_{n-1}, t_{n-1}|\mathbf{x}_n, t_n)\ p(\mathbf{x}_n, t_n)\,. \tag{2.5}$$

Continuous Markov processes

The Markov process itself has a discontinuous character. Markov processes do not really exist in nature, but a system can be regarded as Markov process if its memory time is much smaller than the time at which observation are carried out.

In the same condition, it is useful to describe a Markov process as continuous if, for any $\epsilon > 0$:

$$\lim_{\Delta t \to 0} \frac{1}{\Delta t} \int_{|\mathbf{x}-\mathbf{z}|>\epsilon} \mathrm{d}\mathbf{x}\, p(\mathbf{x}, t+\Delta t|\mathbf{z}, t) = 0\,. \tag{2.6}$$

2.1.2 Fokker-Planck equation and Langevin equation

From the properties of the Markov processes the relationship known as Chapman-Kolmogorov equation is obtained:

$$p(\mathbf{x}_a, t_a|\mathbf{x}_c, t_c) = \int_{-\infty}^{+\infty} \mathrm{d}\mathbf{x}_b \; p(\mathbf{x}_a, t_a|\mathbf{x}_b, t_b) p(\mathbf{x}_b, t_b|\mathbf{x}_c, t_c) \,. \tag{2.7}$$

One requires for p to satisfy the following conditions, $\forall \epsilon > 0$:

$$\lim_{\Delta t \to 0} \frac{1}{\Delta t} p(\mathbf{x}, t + \Delta t|\mathbf{z}, t) = W(\mathbf{x}|\mathbf{z}, t) \,, \tag{2.8a}$$

$$\lim_{\Delta t \to 0} \frac{1}{\Delta t} \int_{|\mathbf{x}-\mathbf{z}|<\epsilon} \mathrm{d}\mathbf{x} \; (x_i - z_i) \; p(\mathbf{x}, t + \Delta t|\mathbf{z}, t) = A_i(\mathbf{z}, t) + O(\epsilon) \,, \tag{2.8b}$$

$$\lim_{\Delta t \to 0} \frac{1}{\Delta t} \int_{|\mathbf{x}-\mathbf{z}|<\epsilon} \mathrm{d}\mathbf{x} \; (x_i - z_i)(x_j - z_j) \; p(\mathbf{x}, t + \Delta t|\mathbf{z}, t) = B_{ij}(\mathbf{z}, t) + O(\epsilon) \,. \tag{2.8c}$$

Adopting the continuity hypothesis 2.6 as well as the set of requirements Eq. 2.8 the Equation 2.7 can be written in differential form:

$$\begin{aligned} \frac{\partial}{\partial t} p(\mathbf{z}, t|\mathbf{y}, t') = & -\sum_i \frac{\partial}{\partial z_i} \left[A_i(\mathbf{z}, t) p(\mathbf{z}, t|\mathbf{y}, t') \right] \\ & + \sum_{i,j} \frac{1}{2} \frac{\partial^2}{\partial z_i \partial z_j} \left[B_{ij}(\mathbf{z}, t) p(\mathbf{z}, t|\mathbf{y}, t') \right] \\ & + \int \mathrm{d}\mathbf{x} \; \left[W(\mathbf{z}|\mathbf{x}, t) p(\mathbf{x}, t|\mathbf{y}, t') - W(\mathbf{x}|\mathbf{z}, t) p(\mathbf{z}, t|\mathbf{y}, t') \right] \,. \end{aligned} \tag{2.9}$$

If we assume $W(\mathbf{z}|\mathbf{x}, t)$ to be 0, Equation 2.9 describes a diffusion process and it is known as Fokker-Planck equation. In the equation, A_i is called the drift term, B_{ij} the Wiener term and the last term within the integral is usually called jump term.

$$\begin{aligned} \frac{\partial}{\partial t} p(\mathbf{z}, t|\mathbf{y}, t') = & -\sum_i \frac{\partial}{\partial z_i} \left[A_i(\mathbf{z}, t) p(\mathbf{z}, t|\mathbf{y}, t') \right] \\ & + \sum_{i,j} \frac{1}{2} \frac{\partial^2}{\partial z_i \partial z_j} \left[B_{ij}(\mathbf{z}, t) p(\mathbf{z}, t|\mathbf{y}, t') \right] \,. \end{aligned} \tag{2.10}$$

The equation 2.10 with the term $A_i = 0$, $B_{ij} = 1$ with the initial condition:

$$p(\mathbf{w}, t_0|\mathbf{w}_0, t_0) = \Pi_i \delta(w_i - w_{i0}) \,, \tag{2.11}$$

where $\delta(\cdot)$ is the Dirac function, has a solution:

$$p(\mathbf{w}, t|\mathbf{w}_0, t_0) = [2\pi(t - t_0)]^{-n/2}\exp\left[-\frac{(\mathbf{w} - \mathbf{w}_0)^2}{2(t - t_0)}\right] , \tag{2.12}$$

that is a multivariate Gaussian with average:

$$\langle \mathbf{w}(t) \rangle = \mathbf{w}_0 \tag{2.13}$$

and variance:

$$\langle [\mathbf{w}_i(t) - \mathbf{w}_0] \ \ [\mathbf{w}_j(t) - \mathbf{w}_0] \rangle = (t - t_0)\delta_{ij} \ . \tag{2.14}$$

One then define a function $\xi(t)$ with the following properties:

$$\langle \xi(t) \rangle = 0 \, , \tag{2.15a}$$

$$\langle \xi(t)\xi(t') \rangle = \delta(t - t') \, . \tag{2.15b}$$

The function is clearly unrealistical because of its infinite variance at $t = t'$, but it is an idealization of *white noise*. The function is clearly not differentiable, but one can require that the function integral exists. Then, we can write $\Psi(t')$, the integral of $\psi(t')$, as:

$$\Psi(t') = \lim_{\epsilon \to 0} \left[\int_0^{t-\epsilon} \mathrm{d}\tau \ \xi(\tau) \right] + \int_t^{t'} \mathrm{d}\tau \ \xi(\tau) \, , \tag{2.16}$$

where for any $\epsilon > 0$, $\xi(\tau)$ in the first integral are independent by the $\xi(\tau)$ in the second one. This means that $\Psi(t')$ is not determined by the values of $\Psi(t)$ but not from his past values, and so it is a Markov process.

In particular it can be proven that the Fokker-Planck equation for Ψ is the equation of the Wiener process $W(t)$ and one can write:

$$\int_0^t \mathrm{d}\tau \xi(\tau) = W(t) \, , \tag{2.17}$$

and from this interpretation, one defines:

$$\mathrm{d}W(t) = W(t + \Delta t) - W(t) = \xi(t)\mathrm{d}t \, . \tag{2.18}$$

Langevin equation and Itô differentiation

In the general form for a multi-variable system, one defines the Langevin equation:

$$\mathrm{d}x_i(t) = a_i(\mathbf{x}(t),t)\mathrm{d}t + b_{ij}(\mathbf{x}(t),t)\mathrm{d}W_j(t)\,. \tag{2.19}$$

Eq. 2.19 is an Itô differential equation if, for all t and t_0:

$$x_i(t) = x_i(t_0) + \int_{t_0}^{t} \mathrm{d}\tau\ a_i(\mathbf{x}(\tau),\tau) + \int_{t_0}^{t} \mathrm{d}W_j(\tau)\ b_{ij}(\mathbf{x}(\tau),\tau)\quad . \tag{2.20}$$

It can be proven that $\mathrm{d}\mathbf{W}$ is an infinitesimal of order 1/2.

$$\mathrm{d}W_i(t)\mathrm{d}W_j(t) = \delta_{ij}\mathrm{d}t\,. \tag{2.21}$$

With that knowledge, the expression for a differential $\mathrm{d}f$ of any funcion $f(\mathbf{x(t)})$ expanded to order $o(\mathrm{d}t)$ is:

$$\mathrm{d}f(\mathbf{x}(t)) = \frac{\partial}{\partial x_j}f(\mathbf{x}(t))\mathrm{d}x_j(t) + \frac{1}{2}\frac{\partial^2}{\partial x_j \partial x_i}f(\mathbf{x}(t))\mathrm{d}x_j(t)\mathrm{d}x_i(t) + O(\mathrm{d}\mathbf{x}(t)^3)\,. \tag{2.22}$$

By the substitution of Eq. 2.19 in Eq. 2.22, and Eq. 2.21, one obtains:

$$\begin{aligned}\mathrm{d}f(\mathbf{x}) = &\left[a_i(\mathbf{x}(t),t)f(\mathbf{x}(t)) + \frac{1}{2}b_{ik}(\mathbf{x}(t),t)b_{kj}(\mathbf{x}(t),t)\frac{\partial^2}{\partial x_i \partial x_j}f(\mathbf{x}(t))\right]\ \mathrm{d}t \\ &+ b_{ij}(\mathbf{x}(t),t)\frac{\partial}{\partial x_i}f(\mathbf{x}(t))\ \mathrm{d}W_j\,.\end{aligned} \tag{2.23}$$

Equation 2.23 shows that, unless $f(\mathbf{x})$ is linear in $\mathbf{x}(t)$, the ordinary calculus chain rule is not valid with stochastic equations.

Given the Itô formula, Eq. 2.23, the Fokker-Planck equation, Eq. 2.10 , and considering the differential of a generic function $f(\mathbf{x}(t))$:

$$\left\langle \frac{\mathrm{d}f(\mathbf{x}(t))}{\mathrm{d}t} \right\rangle = \frac{\mathrm{d}\langle f(\mathbf{x}(t))\rangle}{\mathrm{d}t}\quad , \tag{2.24}$$

it is possible to show that the Langevin equation describes a stochastic process whose FPE is described by:

$$\frac{\partial}{\partial t}p(\mathbf{x},t|\mathbf{x}_0,t_0) = -\frac{\partial}{\partial x_i}[a_i(\mathbf{x},t)p(\mathbf{x},t|\mathbf{x}_0,t_0)] + \frac{1}{2}\frac{\partial^2}{\partial x_i \partial x_j}\left\{[b_{ik}b_{kj}](\mathbf{x},t)p(\mathbf{x},t|\mathbf{x}_0,t_0)\right\} \quad . \tag{2.25}$$

This relationship between Langevin equation and FP equation is fundamental for the development of Lagrangian Stochastic Models.

2.2 Stochastic models for the description of turbulent dispersion

2.2.1 Markov order of the process

In the deterministic framework, the evolution of a point cartesian postion and its derivatives $x_i^{(j)} = \mathrm{d}^j x_i/\mathrm{d}t^j$ can be described by the set of equations:

$$\mathrm{d}x_i^{(j)} = x_i^{(j+1)}\mathrm{d}t\,, \quad j = 0, n. \tag{2.26}$$

Where usually the system is described by equation up to the order $j = 1$ with $x_i^{(2)}$ given by the Second Law of Dynamics.

In Lagrangian Stochastic Models for the description of turbulent dispersion the approach is similar, but, in general, uses a set of equations of the form of eq. 2.19. chosen the maximum order n, the equation for $\mathrm{d}x^{(n)}$ is described by eq.2.19. The maximum order of the derivative described by this system si called the Markov order of the stochastic equation. In applications concerning particle dispersion, the Wiener term b is null up to the maximum order derivative equation.

In a LSM of Markov order n, the evolution of the $x_i^{(n)}$ is independent of its increments at previous time. This assumption is valid if, for a given time interval Δt_s at which the process quantities are sampled, the Lagrangian correlation timescale of the derivatives of order $n+1$ is much smaller:

$$\Delta t_s >> T^{(n+1)}\,. \tag{2.27}$$

In the usual conditions, in the atmosphere, the viscous forces act on timescales of the order of the Kolmogorov timescale, that, for high Re flows, is $\tau_\eta \approx 10^{-2}\ s$. On the other hand, the velocity correlation timescales are of the order of $10^2\ s$ in the PBL.

It follows from this reasoning that the most natural choice for the description of fluid particle dispersion in the atmosphere, in case where the boundary layer turbulence is involved, is the Lagrangian stochastic model of order 1.

Model of order 0 can still used in absence of strong turbulence and for long time simulations, during which the behaviour of the LSM of Markovian order 1 relaxes on the diffusive behaviour of of Markovian order 0 model. The need of Markov order 2 models can arise in cases in which forces other than the viscous one are involved, or the particle simulated are inertial.

2.2.2 Well Mixed Condition

For stochastic processes of a given order n, the expression for the coefficients **a** and **b** is uniquely determined by making use of a number of additional conditions. Among them, one is a requirement for an asymptotic properties of the system of fluid tracers that is of particular relevance in this work.

Invoked when dealing with particle tracers with the same properties of the fluid particles in which they are immersed, the Well Mixed Condition requires that, if at any time the particles are homogeneously distributed within the fluid, in average, then for any subsequent time they remain homogeneously distributed.

For a Markovian model of order 1, denoting with g_f the density function in the phase space for the particle of the fluid, and denoting with g_t the particle of tracers, one has that:

$$\int \mathrm{d}^3\mathbf{u}\ g_f(\mathbf{x}, \mathbf{u}, t) = \langle \rho \rangle\,, \tag{2.28}$$

$$\int \mathrm{d}^3\mathbf{u}\ g_t(\mathbf{x}, \mathbf{u}, t) = \langle c \rangle\,. \tag{2.29}$$

Here, $\langle \rho \rangle$ and $\langle c \rangle$ are the averaged density and concentration of tracer.

The WMC states that, if g_t is a solution of the FPE, Eq. 2.10, then also g_f must be a solution, as well.

In the Markov order 0 model, the WMC simply state that if $\langle c\rangle$ is a solution of the Equation 2.10, then $\langle\rho\rangle$ is a solution as well.

For Random Flight models, from Eq. 2.10, with the substitution of $P \to g_f$, it is possible to obtain an expression for the drift coefficient $\mathbf{a}$:

$$a_i g_f = \frac{\partial}{\partial u_j}(B_{ij} g_f) + \Phi_i(\mathbf{x}, \mathbf{u}, t)\,, \tag{2.30}$$

where Φ satisfies:

$$\frac{\partial \Phi_i}{\partial u_i} = -\frac{\partial g_f}{\partial t} - \frac{\partial}{\partial x_i}(u_i g_f)\,. \tag{2.31}$$

It has to be observed that the WMC do not, in the general case, assure a unique solution. From the Equation 2.31 one sees that Φ is defined with a free choice of a solenoidal term $\partial\psi/\partial u_i = 0$. This ambiguity is automatically solved in the 1-dimensional case only. In models with more than one dimension, other conditions have to be chosen.

The derivation of the Langevin equation for a stochastic process of order 0 taking into account the variation of the fluid density ρ was first derived by Venkatram (1993) and rederived in a more general form by Thomson (1995).

In this case, the FPE equation with the substitution $P \to \langle\rho\rangle$, becomes:

$$\frac{\partial\langle\rho\rangle}{\partial t} = -\frac{\partial}{\partial x_i}(a_i\ \langle\rho\rangle) + \frac{\partial^2}{\partial x_i \partial x_j}(b_{ij}\langle\rho\rangle)\,. \tag{2.32}$$

Brackets around quantities $\langle\cdot\rangle$ denote ensemble averages.

2.2.3 Additional conditions

In order to find an expression for a and b, assumptions on the pdf have to be made.

The coefficients for the Random Flight Model

The expression of the Wiener term coefficient for the RFM is deduced from the small time structure function of the velocity. If particles are in the inertial subrange, from the expression for the structure function, Eq. 1.34, it has to be:

$$2\langle B_{ij}\rangle = \delta_{ij} C_0 \epsilon\,, \tag{2.33}$$

where $B_{ij} = 1/2 b_{ik} b_{jk}$.

The choice of the drift term is usually made by defining a form for the velocity pdf. For a Gaussian distribution of the Eulerian velocity probability density function $p_G(\mathbf{u})$, with $\mathbf{u} = \langle \mathbf{u} \rangle + \mathbf{u}'$, average $\langle \mathbf{u}(\mathbf{x}, t) \rangle$ and covariance tensor $V_{ij}(\mathbf{x}, t) = \langle u'_i u'_j \rangle$:

$$p_F(\mathbf{u}) = \frac{1}{(2\pi)^{3/2} \det(V)^{1/2}} \exp\left(-\frac{1}{2} u'_i (V^{-1})_{ij} u'_j \right) . \tag{2.34}$$

With this choice for the PdF, the drift term a_i can be rewritten as follows:

$$a_i = -\frac{b^2}{2} (V^{-1})_{ik} u'_k + \frac{\Phi_i}{p_G} , \tag{2.35}$$

where:

$$\frac{\Phi_i}{p_G} = \frac{1}{2} \frac{\partial V_{il}}{\partial x_l} + \frac{\mathrm{d}\langle u_i \rangle}{}, \mathrm{d}t + \frac{1}{2} (V^{-1})_{lj} \frac{\mathrm{d}V_{il}}{\mathrm{d}t} u'_j , \tag{2.36}$$

with:

$$\frac{\mathrm{d}}{\mathrm{d}t} = \frac{\partial}{\partial t} + u_j \frac{\partial}{\partial x_j} \equiv \frac{\partial}{\partial t} + (\langle u_j \rangle + u'_j) \frac{\partial}{\partial x_j} . \tag{2.37}$$

Now,

$$\mathrm{d}u_i = \mathrm{d}\langle u_i \rangle + \mathrm{d}u'_i = \frac{\mathrm{d}\langle u_i \rangle}{\mathrm{d}t} \mathrm{d}t + \mathrm{d}u'_i , \tag{2.38}$$

thus, the Langevin equation for the velocity reads:

$$\mathrm{d}u'_i = a_i \mathrm{d}t - \frac{\mathrm{d}\langle u_i \rangle}{\mathrm{d}t} \mathrm{d}t + b_{ij} \mathrm{d}W_j(t) . \tag{2.39}$$

Using eqs. 2.35 and 2.36, eq. 2.39 reads:

$$\mathrm{d}u'_i = \left[-\frac{b^2}{2} (V^{-1})_{ik} u'_k + \frac{1}{2} \frac{\partial V_{il}}{\partial x_l} + \frac{1}{2} (V^{-1})_{lk} \frac{\mathrm{d}V_{il}}{\mathrm{d}t} u'_k \right] \mathrm{d}t + b \mathrm{d}W_i(t) . \tag{2.40}$$

Including third- and fourth-order velocity moments

In many applications, such as the dispersion in a CBL, assuming a Gaussian velocity pdf is inappropriated.

In cases where the third and fourth order moments are far from gaussian, different approaches are available.

In order to describe an Eulerian velocity pdf with third and fourth order moments other than Gaussian, it is possible to assume a form for the pdf P as a sum of two Gaussian distributions (Luhar and Britter, 1989):

$$P_S = C_A P_A + C_B P_B \, , \tag{2.41}$$

where (with $\Lambda = A, B$) C_Λ are constants and P_Λ are gaussian distribution characterized by $\langle u \rangle_\Lambda$ and $\sigma^2_{u3\Lambda}$, of the form:

$$P_\Lambda = \frac{1}{(2\pi)^{1/2}\sqrt{\sigma^2_{u3\Lambda}}} \exp\left[-\frac{(u_3 - \langle u_3 \rangle_\Lambda)^2}{2\sigma^2_{u3\Lambda}} \right] \, . \tag{2.42}$$

With this choice, with the hypothesis of time stationarity and horizontal homogeneity, the drift term a of the Langevin equation takes the form:

$$a = \frac{C_0 \varepsilon}{2} \frac{\mathrm{d}}{\mathrm{d}u_3} \ln(p_E) + \Phi_A + \Phi_B \, , \tag{2.43}$$

with:

$$\begin{aligned}
\Phi_\Lambda = {} & \frac{\mathrm{d}C_\Lambda}{\mathrm{d}x_3} P_\Lambda \sigma^2_{u3\Lambda} + \\
& + C_\Lambda \left[\frac{1}{2} \frac{\mathrm{d}\sigma^2_{u3\Lambda}}{\mathrm{d}x_3} + (u_3 - \langle u_3 \rangle_\Lambda) \frac{\mathrm{d}\langle u_3 \rangle_\Lambda}{\mathrm{d}x_3} + \frac{(u_3 - \langle u_3 \rangle_\Lambda)^2}{2\sigma^2_{u3\Lambda}} \frac{\mathrm{d}\sigma^2_{u3\Lambda}}{\mathrm{d}z} \right] P_\Lambda + \\
& + \frac{1}{2} C_\Lambda \mathrm{erf} \left[\frac{-(u_3 - \langle u_3 \rangle_\Lambda)}{2\sigma^2_{u3\Lambda}} + 1 \right] \frac{\mathrm{d}\langle u_3 \rangle_\Lambda}{\mathrm{d}x_3} + \\
& + \frac{1}{2} \langle u_3 \rangle_\Lambda \mathrm{erf} \left(\frac{-(u_3 - \langle u_3 \rangle_\Lambda)}{2\sigma^2_{u3\Lambda}} \right) \frac{\mathrm{d}C_\Lambda}{\mathrm{d}x_3} + \\
& + \frac{1}{2} \langle u_3 \rangle_\Lambda C_\Lambda \frac{\mathrm{d}}{\mathrm{d}x_3} \left\{ \mathrm{erf} \left[\frac{-(u_3 - \langle u_3 \rangle_\Lambda)}{2\sigma^2_{u3\Lambda}} \right] \right\} \, .
\end{aligned} \tag{2.44}$$

Adopting a different approach, Franzese et al. (1999) approximate the drift term as a quadratic function of the velocity instead of fixing a functional form for the velocity Pdf.

The Coefficients of the Random Displacement Model

If the density is constant, the FPE has the same form of the diffusion equation. Is thus a natural choice to assume $b_{ij} = 2K_{ij}$, where K_{ij} is the diffusion coefficient.

To obtain the expression for the drift coefficient a, an additional condition is given by the continuity equation, written by Thomson (1995) in the form:

$$\frac{\partial \langle \rho \rangle}{\partial t} = -\frac{\partial}{\partial x_i} \left(\overline{u}_i \langle \rho \rangle \right) \, . \tag{2.45}$$

Here, $\overline{u}_i$ is defined to be the density weighted velocity i-th component of the velocity field,

$$\overline{u}_i = \frac{\langle u_i \rho \rangle}{\rho} = \langle u_i \rangle + \frac{\langle u_i' \rho' \rangle}{\langle \rho \rangle} \, . \tag{2.46}$$

With this choice, the following expression for the drift term a is obtained:

$$a_i = \frac{\partial K_{ij}}{\partial x_j} + \frac{K_{ij}}{\langle \rho \rangle} \frac{\partial \langle \rho \rangle}{\partial x_j} + \overline{u}_i \, . \tag{2.47}$$

Chapter 3

Numerical Techniques

3.1 Introduction

In the computations made in this work, an extended use of general numerical technique has been made. Among them, functional evaluation algorithms, fast fourier transfrom, polynomial equation solvers, integration and derivation techniques have been applied (Press et al., 1992).

It is useful to describe two more specific subjects. The following sections present an overview of the schemes used for the integration of stochastic equations and the polynomial interpolation scheme used in the computations.

3.2 Numerical algorithms for the integration of Stochastic equations

Because of the non-deterministic nature of the SDE, there is the need of defining specifically suited numerical integration methods. The accuracy of a numerical algorithm for SDE, in the same way, has to be evaluated using statistical tools.

3.2.1 Strong and weak convergence

An evaluation criterion is the requirement that every trajectory of the numerical approximation converge to the analytical trajectory path for a sufficiently small integration step. Given a succession of N integration steps, if X_i and Y_i are the analytic and numerical approximated solution of a SDE at the steps i respectively, the integration scheme producing Y_i values is said to converge in the strong sense with order γ if, given $\delta_0 > 0$ and $\alpha > 0$, the expectation value:

$$E(|X_N - Y_N|)\,,$$

respects the relation:

$$E(|X_N - Y_N|) \leq \alpha\delta^{\gamma}\ ,\ \ \forall\delta \in]0, \delta_0[\ . \tag{3.1}$$

In cases where it is not necessary to have a close pathwise approximation of a stochastic process, a less strict convergence definition can be adopted. The comparison between $\mathbf{Y}$ and $\mathbf{X}$ can be made by comparing some function g of $\mathbf{Y}$ and $\mathbf{X}$, instead.

The discrete approximation $\mathbf{Y}$ is said to converge to $\mathbf{X}$ in the weak sense with order β if,for any polynomial function g , there exist $\delta_0 > 0$, $\alpha > 0$ such that:

$$|E(g(X_N)) - E(g(Y_N))| \leq \alpha\delta^{\beta}\ ,\ \ \forall\delta \in]0, \delta_0[\ . \tag{3.2}$$

When referring to algorithm for the integration of SDE, in the remainder of this text, an algorithm that converges in the strong sense with order γ will be simply called a ‘strong order γ’ algorithm. In the same way, an algorithm that converges in the weak sense with order β will be simply called a ‘weak order β’ algorithm.

3.2.2 Finite difference schemes

In order to obtain an expression for many finite differences scheme, the more general and direct way is to obtain each scheme by truncating the stochastic Taylor formula (Kloeden and Platen, 1992a,b).

Let one, for simplicity, considers the Langevin Equation 2.19 in the one-dimensional form. The simplest forward scheme for the integration of this equation is the Euler-Maruyama scheme:

$$Y_{n+1} = Y_n + a\Delta_n + b\Delta W_n \ , \tag{3.3}$$

where Δ_n is the integration timestep. This scheme can also be obtained heuristically as the stochastic equivalent of the ODE Euler integration scheme. Coming to stochastic equations, this is a strong order 0.5 scheme. In order to obtain a strong order 1 scheme an additional term is needed, and the algorithm, known as the Milstein scheme, reads:

$$Y_{n+1} = Y_n + a\Delta_n + \frac{1}{2}bb'\Delta_n + b\Delta W_n \ , \tag{3.4}$$

where $b' = \mathrm{d}b/\mathrm{d}x$. Because it includes the Stochastic Taylor expansion up to the first order, the Milstein scheme is the stochastic counterpart to the Euler finite difference scheme for ODEs.

Schemes of higher order exists, which are suited for solving specific problem with the algorithms, such as implicit scheme (for problem affected by stiffness) and/or higher order multistep schemes.

In this work, since most of the complexities are left to the resolved velocity fields and the computational cost of the unresolved motion modelling has to be kept as low as possible, the Euler-Maruyama and the Milstein scheme are the only two considered.

3.3 Interpolation

In practical application, it is usual to have values of a field F defined on a set of points organized in a grid. This is the case for variables of an Eulerian model. Lagrangian models need to compute the field values at any point in the domain.

Given a set $x_0 < x_1 < ... < x_n$ of points, and a set $F_0, F_1, ..., F_n$ of values. The skill of an interpolating function $f(x)$ with $f(x_1) = F_1$, ..., $f(x_n) = F_n$ in describing the values of the field F for $x \in [x_i, x_{i+1}]$ can sometimes have strong influence on further numerical results.

Many interpolation methods exist. Among the functional forms used, the most common are polynomials, quotients of polynomials (rational functions), trigonometric functions and spline. An interpolation method can emphasize some features of the interpolating function. Some of the more common required properties are listed below (Akima, 1991).

- Continuity. If, for a small change of the input data correspond a small change in the interpolated curve, the method is said to be continuous.
- Linearity. This properties is respected if, for all node points i, if $y_i = af(x_i)+bf(x_i)$ then for any point in the interval $[x_0, x_n]$ it also holds the relationship: $y_i = af(x_i) + bf(x_i)$.
- Monotonicity preservation. The monotonicity dictates that if a set of two consecutive data points has the same value of $f(x)$, then the portion between the two points must be an horizontal segment.
- Positivity. Some data distribution represents quantities that are not supposed to get negative value. In that case, the method used in the interpolation has to mantain this properties.

Local interpolating algorithms, which use a finite number of interpolation points near the point of interest x, in general do not ensure the continuity of the derivatives of the function. When, in some application, the continuity of the derivative of the interpolating function is of concern, it has to be chosen an appropriate method, which involve a non-local choice of the parameters.

3.3.1 Polynomial interpolation

In polynomial interpolation, the values of a function of which is known a set of $n+1$ points, is represented by a polynomial $\mathcal{P}_n(x) \in \mathbb{P}_n$, where $\mathbb{P}_n$ is the set of polynomial of degree n. $\mathcal{P}_n(x)$ has the properties that:

$$\mathcal{P}_n(x_i) = f(x_i)\,. \tag{3.5}$$

With the choice of a base $\{l_i\}_{i=0}^{n}$ for the polynomial $\mathcal{P}_n(x)$, $l_i \in \mathbb{P}_n$ defined as:

$$l_i(x) = \prod_{j=0, j\neq i}^{n} \frac{x - x_j}{x_i - x_j}. \tag{3.6}$$

The polynomial $\mathcal{P}_n(x)$ can be rewritten as:

$$\mathcal{P}_n(x) = \sum_{i=0}^{n} f(x_i) l_i(x) \tag{3.7}$$

Eq. 3.7 is known as Lagrange form of the polynomial $\mathcal{P}_n$.

The polynomial interpolation is unstable (can give rise to unnatural fluctuation in the interpolated values) for large n. Because of that, it is natural to define a subset of the points $[x_i, x_j] \subset [x_0, x_{n+1}]$ and to use Lagrangian interpolation on every subset.

The most simple and ecomomical approximation is the linear approximation: in this case, $n = 0$ and, for $x \in [x_i, x_i + 1]$ Eq. 3.7 is simply expressed by:

$$f(x) = f(x_i) l_i + f(x_{i+1}) l_{i+1}\,, \tag{3.8}$$

and:

$$\begin{aligned} l_i &= \frac{x - x_i}{x_{i+1} - x_i}\,, \\ l_{i+1} &= \frac{x_{i+1} - x}{x_{i+1} - x_i} = 1 - l_i\,. \end{aligned} \tag{3.9}$$

3.3.2 Hermite-Birchoff interpolation

If the derivative at the nodes x_i are available, the Lagrange polynomial interpolation can be generalized.

If the data $(x_i, f^{(k)}(x_i))$ are available, where $i = 0, n$ is the number of distinct points and $k = 0, m$ is the order of the known f derivatives , one defines $N = \sum_{i=0}^{n} m_i$. It can be shown that exist a unique polynomial $H_{N-1} \in \mathbb{P}_{N-1}$ with the proprety that:

$$H_{N-1}^{(k)}(x_i) = f^{(k)}(x_i); \qquad\qquad i = 0, n;\ k = 0, m\,. \tag{3.10}$$

H_{N-1} is called Hermite interpolating polynomial.

Hermite polynomial interpolation applied with a knowledge of the derivative up to the order m, ensure the consistency between the values of the interpolating function and its derivative up to the order m between the nodes and within the order $m - 1$ at the node points.

3.3.3 Spline

The continuity and derivability on the whole interval $[x_0, x_n]$ can be obtained by using a non-local algorithm, and the interpolation parameters are computed as a succession of connected curve. This method is known a spline interpolation:

Given the set of points $x_i \in \{x_0, x_n\}$ a function $s_k(x)$ is defined to be a spline of degree k if, for every subinterval $S_j = [x_j, x_j + 1]$:

$$s_k|_{Sj} \in \mathbb{P}_k, \qquad j = 0, 1, ..., n-1\,, \tag{3.11}$$

$$s_k \in C^{k-1}[x_0, x_n] \qquad . \tag{3.12}$$

From the definition above a spline function of order k cannot be uniquely defined. The polynomial spline of order k can be written in general form as:

$$s_k|_{Sj}(x) = \sum_{i=0}^{k} s_{ij}(x - x_j)^i \tag{3.13}$$

for $x \in [x_j, x_{j+1}]$. The problem has $(k+1)n$ degrees of freedom. From the definition of spline, Eq. 3.12, it follows that:

$$\frac{\mathrm{d}^m s_k|_{Sj-1}(x_j)}{\mathrm{d}x^m} = \frac{\mathrm{d}^m s_k|_{Sj}(x_j)}{\mathrm{d}x^m}\,, \tag{3.14}$$

which poses $k(n-1)$ additional constraints. With the requirement of having an interpolating spline, for which $s_k(x_j) = f(x_j)$ at the nodes, other n constraints are required. The problem of finding an interpolating spline meeting those requirements has still $k-1$ degrees of freedom left.
The uniqueness of the solution is usually achieved by adding conditions on the extremes of the interpolation domain, such as periodic conditions.

The spline interpolation presents some disadvantages: in presence of strong gradient in the function points, the resulting interpolated values presents strong innatural oscillation. Moreover, in some application, is not possible or practically useful to consider the whole domain for applying the interpolation.

3.3.4 Akima local algorithm

In the following section a class of method (based on similar principles of the Hermite-Birchoff methods) devised by Akima (1970) and subsequently reviewed by Akima (1991).

Akima algorithm is a local interpolation method based on the idea of obtaining a fitting curve with not excessives unnatural obscillations (a 'natural looking curve', Akima (1970)). This is obtained by choosing a condition for the selection of the curve parameter in such a way that 3 (Akima, 1970) or 4(Akima, 1991) collinear point must result in a straight line.

The curve is a third degree polynomial:

$$f(x) = a_0 + a_1(x - x_i) + a_2(x - x_i)^2 + a_3(x - x_i)^3 \,, \tag{3.15}$$

where the coefficients are:

$$\begin{aligned}
a_0 &= f(x_i)\,, \\
a_1 &= f'(x_i)\,, \\
a_2 &= -[2(f'(x_i) - m_i) + (f'(x_{i+1}) - m_i)]/(x_{i+1} - x_i)\,, \\
a_3 &= -[(f'(x_i) - m_i) + (f'(x_{i+1}) - m_i)]/(x_{i+1} - x_i)^2\,,
\end{aligned} \tag{3.16}$$

where m_i is the slope of the line segment connecting $\{x_i, f(x_i)\}$ and $\{x_{i+1}, f(x_{i+1})\}$ (compute as the finite two-point finite differences value).

In the computation of the first order derivatives $f'(x_i)$ and $f'(x_{i+1})$ lies the difference between the two Akima method. The principle on which are built both variants is to express the the derivative at a node as the weighted average of the numerical derivatives computed at a number of neighboring nodes.

In Akima (1970), for each point x_i, the values of the derivative is estimated from the values of the function at 4 intervals around x_i (this estimate involve the evaluation of the function at five nodes):

$$f'(x_i) = \frac{m_{i-1}\omega_{i-1} + m_i\omega_i}{\omega_{i-1} + \omega_i}\,, \tag{3.17}$$

$$\begin{aligned}\omega_{i-1} &= 1/|m_{i-2} - m_{i-1}|\,,\\ \omega_i &= 1/|m_i - m_{i+1}|\,. \end{aligned} \tag{3.18}$$

In the second variant, Akima (1991), the derivative of the function at the point x_i is computed as a combination of finite differences at 6 different intervals surrounding the data point, for a total of 7 nodes involved in the computation.

$$f'(x_i) = \left(\sum_{k=-2}^{1} {y'_i}^{\,i+k}\omega_{i+k}\right) / \left(\sum_{k=-2}^{1}\omega_{i+k}\right)\,. \tag{3.19}$$

Here, the weight factor ω , which can be written as:

$$\begin{aligned}\omega_{i-2} &= 1/\left(V(i,i-3,i-2,i-1)D(i,i-3,i-2,i-1)\right)\,,\\ \omega_{i-1} &= 1/\left(V(i,i-2,i-1,i+1)D(i,i-2,i-1,i+1)\right)\,,\\ \omega_{i} &= 1/\left(V(i,i-1,i+1,i+2)D(i,i-1,i+1,i+2)\right)\,,\\ \omega_{i+1} &= 1/\left(V(i,i+1,i+2,i+3)D(i,i+1,i+2,i+3)\right)\,. \end{aligned} \tag{3.20}$$

In Equation 3.20, V is a square difference factor computed respect to the linearity:

$$V(i,j,k,l) = \sum_{m=min\{i,j,k,l\}}^{max\{i,j,k,l\}} \left[f(x_m) - b_0 - b_1x_m\right]^2\,, \tag{3.21}$$

Here,writing for notational simplicity:

$$\sum_m = \sum_{m=min\{i,j,k,l\}}^{max\{i,j,k,l\}}\,,$$

The b factors are computed as follow:

$$\begin{aligned} b_0 &= \left[\sum_m x_m^2 \sum_m f(x_m) - \sum_m x_m \sum_m x_m f(x_m)\right] / \left[4\sum_m x_m^2 - \left(\sum_m x_m\right)^2\right]\,,\\ b_1 &= \left[4\sum_m x_m f(x_m) - \sum_m x_m \sum_m f(x_m)\right] / \left[4\sum_m x_m^2 - \left(\sum_m x_m\right)^2\right]\,. \end{aligned} \tag{3.22}$$

The parameter D is chosen ad the quadratic distance between the reference point $\{x_i, f(x_i)\}$ and the other three points:

$$D(i,j,k,l) = (x_j - x_i)^2 + (x_k - x_i)^2 + (x_l - x_i)^2 \tag{3.23}$$

Finally, the first derivative at the data point $\{x_i, f(x_i)\}$, computed as the derivative of a third degree polynomial fitted to a set of four data points, is represented by:

$$\begin{aligned} F(i,j,k,l) = \big[&(f(x_j) - f(x_i))(x_k - x_i)^2(x_l - x_i)^2(x_l - x_k) \\ &+ (f(x_k) - f(x_i))(x_l - x_i)^2(x_j - x_i)^2(x_j - x_l) \\ &+ (f(x_l) - f(x_i))(x_j - x_i)^2(x_k - x_i)^2(x_k - x_j)\big] \\ &/[(x_j - x_i)(x_k - x_i)(x_l - x_i)(x_k - x_j)(x_l - x_k)(x_l - x_j)] \end{aligned} \tag{3.24}$$

When a set of four data points is collinear, the V value is zero and the weight becomes infinite[1]. This method, thus, has the properties that a linear segment is produced whenever 4 data points are collinear.

Akima (1991) algorithm is consistent with a third-degree polynomial interpolation accuracy. When interpolating a generic function, it has continuous first order derivatives but, in general, discontinuous second order derivatives at the nodes.

3.3.5 Positivity requirements

In most of the interpolation, and, more generally, function approximation techniques, there are additional requirements on the final features, properties and general appearence of the function.

The shape preserving methods and approximation have been developed for the needs of preserving relevant properties such as monotonicity, convexity, reduce oscillation (like Akima (1970, 1991) algorithms, and non-negativity.

The last property (non-negativity) is of particular importance when dealing with physical quantities that must be, by their nature, non-negative.

---

[1] When this happens, in practical application the infinite coefficient is set to 1 and the finite ones are set to 0

Mathematically speaking, when requiring an interpolation function $f(x)$ to be positive, one requires that, for given a set of points $\mathcal{I} = \{x_i, y_i\}_{i=0,n} \subseteq \mathcal{L}$ where $y_i \geq 0 \ \forall x_i \in \mathcal{I}$, f has the properties of an interpolating function and:

$$f(x) \geq 0 \ \ \forall x \in \mathcal{L}\,. \tag{3.25}$$

A vast number of available techniques exists, based on different kinds of interpolation and different approximation. Many involve spline interpolation algorithm, and the techniques are based on spline under tension (Riedel, 2005), rational spline (Gregory, 1986; Hussain and Sarfraz, 2008) and/or the addition of suitable supplementary interpolating points(Riedel, 2005; Hussain and Sarfraz, 2008).

Schmidt and Heß (1987) studied necessary and sufficient conditions for the positivity of quadratic spline interpolation, and Schmidt and Heß (1988) defined suitable condition for cubic polynomial spline to mantain non-negativity.

Fischer et al. (1991) propose a local algorithm for the construction of a non-negative spline.

A properties of natural spline is that, given a spline s defined in the whole interpolation interval $[x_0, x_n]$, has the properties that the integral:

$$\int_{x0}^{xn} \mathrm{d}x \ (s''(x))^2, \tag{3.26}$$

is minimized. From a geometrical point of view, $s''(x)$, the Expression 3.26 represents the curvature of the spline. This means that the choice natural spline minimize the tension of the spline curve.

Under the hypothesis that the polynomial function takes negative values between two consecutive data points x_i, x_{i+1}, the Fischer et al. (1991) method search for a function $\widetilde{s}(x)$ which is non-negative and minimizes the condition:

$$\int_{xi}^{xi+1} \mathrm{d}x \ (s''(x))^2, \tag{3.27}$$

Fischer et al. (1991) show that the goal is accomplished by selecting a function that, depending on the condition, takes a value of 0 between two additional nodes inserted in the interval, or, has a single zero on a single node [2]. The function is defined in such a way that the values of $\widetilde{s}$, $\widetilde{s}'$, $\widetilde{s}''$, matches the value of the original function at the extremes x_i, x_{i+1}.

Now, we rename for the sake of brevity the extremes of the function:

$$\begin{aligned} p_0 &= x_i\,, \\ \sigma_0 &= s(p_0)\,, \\ \sigma_0' &= s'(p_0)\,, \\ p_1 &= x_{i+1}\,, \\ \sigma_1 &= s(p_1)\,, \\ \sigma_1' &= s'(p_1)\,. \end{aligned}$$

If the conditions:

$$\sigma_0' < 0, \quad \sigma_1' > 0, \quad p_1 - p_0 > 3\left(\frac{\sigma_1}{\sigma_1'} - \frac{\sigma_0}{\sigma_0'}\right)\,, \tag{3.28}$$

are satisfied, the non-negative curve $\widetilde{s} : [p_0, p_1] \to \mathbb{R}^+$ is defined with two additional internal points, ξ_l, ξ_r:

$$\xi_l = p_0 - \frac{3\sigma_0}{\sigma_0'}, \quad \xi_r = p_1 - \frac{3\sigma_1}{\sigma_1'}. \tag{3.29}$$

And $\widetilde{s}(x)$ has the form:

$$\widetilde{s}(x) = \begin{cases} \widetilde{s}_l(x) = a_l(\xi_l - x)^3 & ,\ x \in [p_0, \xi_l], \\ 0 & ,\ x \in [\xi_l, \xi_r], \\ \widetilde{s}_r(x) = a_r(x - \xi_r)^3 & ,\ x \in [\xi_r, p_1]. \end{cases} \tag{3.30}$$

with the coefficients:

$$a_l = -\frac{{\sigma_0'}^{\,3}}{27\sigma_0^2}, \quad a_r = \frac{{\sigma_1'}^{\,3}}{27\sigma_1^2}. \tag{3.31}$$

If the Conditions 3.28 are not met, there is only to define a single internal point which is a zero of the cubic polynomial[3]:

$$g(\xi) = (p_1 - \xi)^2\ (3\sigma_0 + \sigma_0'\ (\xi - p_0)) - (\xi - u)^2\ (3\sigma_1 - \sigma_1'\ (p_1 - \xi)) \tag{3.32}$$

---

[2] They defined this spline as a spline with a contact arc or a boundary line.

[3] The polynomial of eq. 3.32 has always at least one zero in $]p_0, p_1[$ since $g(p_0) > 0$ and $g(p_1) < 0$ (Fischer et al., 1991).

And $\widetilde{s}(x)$ has the form:

$$\widetilde{s}(x) = \begin{cases} \widetilde{s}_l(x) = a_l(\xi - x)^3 + b_l(\xi - x)^2 & , \quad x \in [p_0, \xi], \\ \widetilde{s}_r(x) = a_r(x - \xi)^3 + b_l(x - \xi)^2 & , \quad x \in [\xi, p_1]. \end{cases} \tag{3.33}$$

Here, the coefficients are:

$$b_l = \frac{(p_1 - \xi)^2[3\sigma_0 + \sigma_0'(\xi - p_0)]}{(\xi - p_0)(p_1 - \xi)}\,. \tag{3.34}$$

The plot in Fig. 3.1 show the interpolating function generated by the Akima (1970) and Akima (1991) algorithms for a set of data. For both the interpolating functions, anegative fluctuation appears between $\sigma = 0.9$ $\sigma = 0.92$ Also shown the Akima (1970) interpolating function after the application of Fischer et al. (1991) algorithm for ensuring positivity.

In Fig. 3.2 a the same functions are shown, but the domain is restricted in the negative fluctuation area.

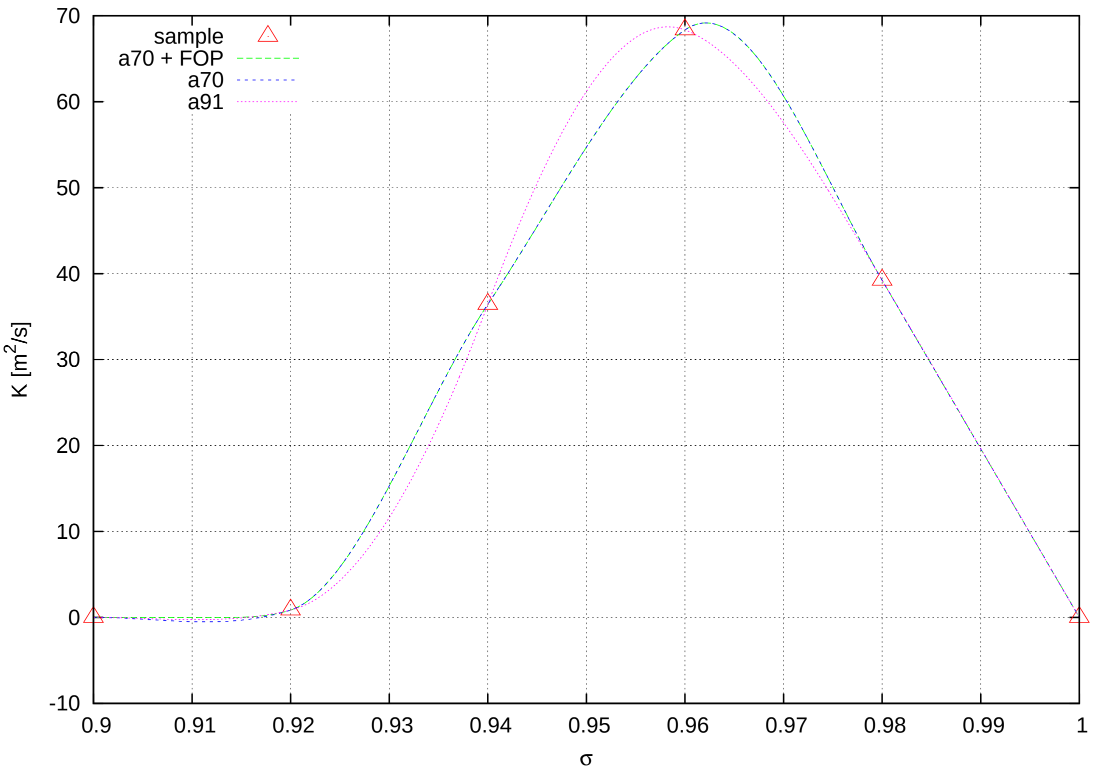

Figure 3.1: Interpolating function of the data (red triangles) computed with the Akima (1970) (blue line) and Akima (1991)(purple line) algorithms. The green line shows the Akima (1970) interpolation function applied with the positivity control algorithm proposed by Fischer et al. (1991).

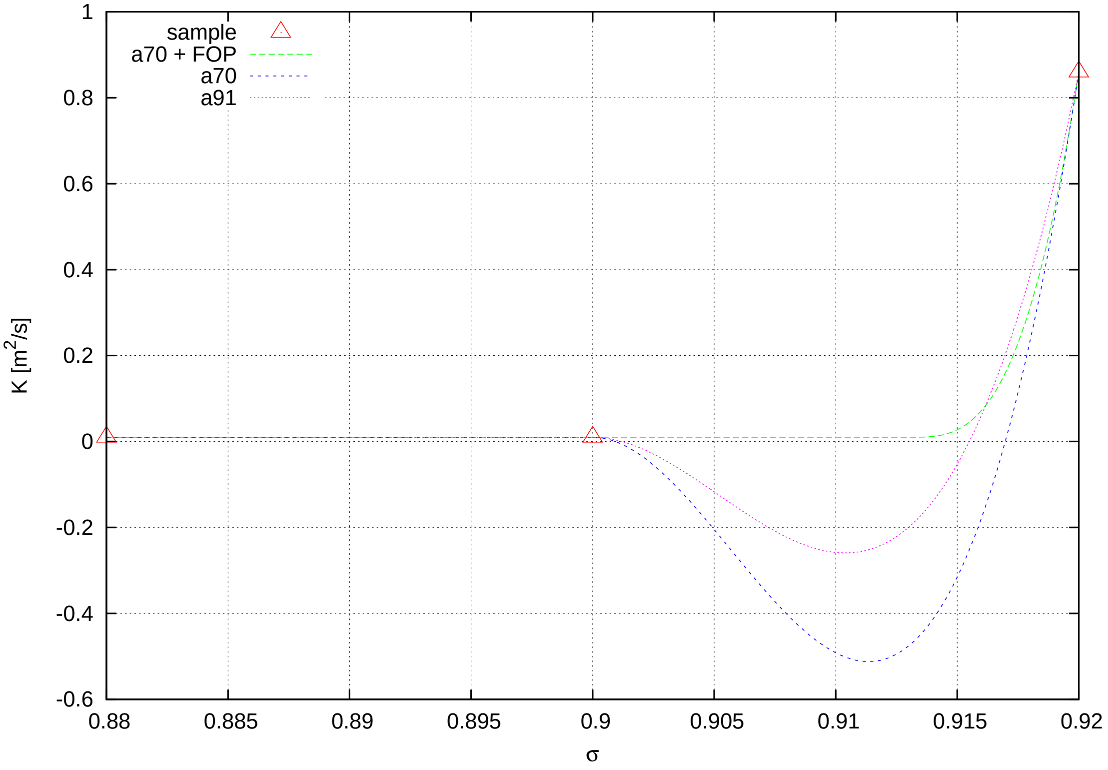

Figure 3.2: Interpolating function of the data (red triangles) computed with the Akima (1970) (blue line) and Akima (1991)(purple line) algorithms. The green line shows the Akima (1970) interpolation function applied with the positivity control algorithm proposed by Fischer et al. (1991).

Part II

Models and Experiments

Chapter 4

Implementation of the models

4.1 Introduction

One can roughly separate the factors influencing the model development between four different aspects

- The properties of the flow to be reproduced, such as velocity moments and dispersion statistics.

  In our case, there is a basic properties that every selected model is required to fulfill, and it is the well mixed condition. In some applications, for computational or practical reason, a deviation from this condition can be permitted if it is not influent on the experiment results, but there must exist a feasible numerical experiment that show the model consistency with the WMC.

- Characteristics of the dynamical model that have influence on the LPDM.

  Since every dynamical model considered here use some parameterization for the small scale turbulence, it fall within this aspect the choice of an unresolved motion model.

- Numerical efficiency and low computational cost of the model.

  Efficiency and accuracy of the model are going to be evaluated considering that a low computational cost has to be mantained, both for time savings and for obtaining a better statistics from experiments (using more particles). In principle, a LPDM can be run at the same time of a dynamical model and has to use only a small fraction of the computing power of a machine.

- The needs for generality and adaptability to different Eulerian models and settings of the LPDM code.

  With reference to the last point, the models implemented in this work do not aim for generality, favouring, where possible, the maintainance of an internal consistency with their reference Eulerian model.

Among the dynamical models where to implement a LPDM, the choice involved two models that represent two extremes of resolution within the class of models with a turbulence parameterization (i.e., that are not Direct Numerical Simulations (DNS)): a LES and a General Circulation Model(GCM).

In the LES, part of the small scale turbulence can be explicitly described and the resolution limit lies in the inertial subrange, the K41 theory constitutes the basis on many consideration about unresolved turbulence statistics. The LPDM has to be implemented to describe with good accuracy the inertial subrange effect, and the specific properties of the flow are easily computed and can be taken into account.

The general circulation model has resolution of tenth of kilometers (hundredths in some configurations) and covers every kind of limit condition for turbulence. The unresolved motion parameterization have been chosen to be consistent with the subgrid vertical transport closure of the global scale model. Since the sampling times on which the general circulation model usually work is usually larger than the correlation time of most of the small scale turbulence, one can expect the simply diffusive model to describe adequately the unresolved motion. Parameterization more suited for the description of CBL dispersion, mesoscale effects and deep moist convection, that can display a Lagrangian timescale of the order of the Eulerian integration timestep, can be added in the future.

The aim of this chapter is to offer to the reader, after a short review of existing models and applications of LPDM in geophysical and environmental problems, a description of the unresolved field model parameterizations adopted in this work, and their implementation.

4.2 Overview of existing Lagrangian Particle Dispersion Models

4.2.1 Large eddy simulations studies on dispersion

Because of the widespread use of LES, it gives a frame for modelling dispersion of tracers in various conditions. The explicit description of the large scale eddies is expected to improve the skill of the dispersion modelling, and to allow to explicity deal with effects like meandering (Csanady, 1973).

The use of a LES to describe particle dispersion was firstly proposed by Lamb (1978). Other works followed (e.g. Henn and Sykes (1992); Dosio et al. (2003); Dosio and de Arellano (2006)). Among these, the works of Weil et al. (2004); Vinkovic et al. (2006a); Cai and Leclerc (2006); Weil et al. (2012) used a Lagrangian Stochastic model to describe the effects of unresolved motion on the dispersion of particles.

Thomson (1987) seminal paper indicates a procedure for the formulation of the noise and drift terms in a LSM using a Langevin equation for the velocity increments, which allows to reproduce the Eulerian velocity statistics and requires the existence of an inertial subrange in the velocity field.

4.2.2 Trajectory models for long range transport studies

Trajectory models have been used to study transport processes in the atmosphere for several decades now. The technique was firstly proposed by Pettersen(1940). With the increment of available data and computing resources [1], trajectory modelling is now a widely used tool in many fields of atmospheric sciences.

Trajectory models are used to establish a source-receptor relationship for pollutants or natural particles (Stohl and Trickl, 1999; Cape et al., 2000; Izquierdo et al., 2011;

---

[1] The computing has seen an increase of a factor 2 every 18 months. The phenomenon is known as Moore's law(Lloyd, 2000)

Wotawa et al., 2000), to identify pathways of water vapor transport, and to study the dispersion of tracers from natural events or human-related incidents (Damoah et al., 2004; Haszpra and Tel, 2011; Srinivas et al., 2012). Other applications can study the influence of climate phenomena on air transport.

Validations of the model skill often make use of data from long range experiments, such as CAPTEX, ANATEX and ETEX, where the horizontal dispersion of emission of organic tracers were studied on scales of 100-1000 km (Stohl et al., 1998).

4.3 Eulerian models considered in this work

4.3.1 Large Eddy Simulation

The well known Weather Research and Forecasting (WRF) Model, ver. 3.0, has been used to obtain the velocity fields data. This model (Grell et al., 2005) solves the fully compressible, nonhydrostatic equations of motion in a terrain-following hydrostatic-pressure coordinate.

A Runge-Kutta second or third order time-integration scheme and a second to sixth order spatial discretization scheme for the advection term are implemented in WRF. The model uses a time-splitting scheme, in which fast acoustic and gravity wave modes are computed with a smaller time step.

WRF can configured as a Large Eddy Simulation (LES), which means that the turbulent motion of eddies responsible for the boundary layer dynamics is explicitly resolved (Moeng and Wyngaard, 1988; Moeng et al., 2007; Antonelli and Rotunno, 2007; Catalano and Moeng, 2010).

For the development of the LPDM, we used the output produced by this model. The output consisted in the resolved velocity fields u_{Ri} for the three velocity components, and in the subgrid kinetic energy field e_S. The fields are sampled on Cartesian coordinates both in the horizontal and vertical direction.

Forecast	n. long.	n. lat.	n. σ	long. res.	lat. res. [km]	Δt
Monthly	362	242	50	78 km	165 km	432 s
Monthly (high res.)	450	322	50	63 km	124 km	360 s
Operational	898	626	60	31 km	63 km	180 s
Experimental(high res.)	1202	818	60	24 km	49 km	150 s

Table 4.1: Resolution settings adopted by GLOBO. Longitude resolution refers to a 45° latitude.

4.3.2 GLOBO, general atmospheric circulation model

GLOBO (Malguzzi et al., 2011) is a global scale model developed at the institute ISAC of the National Council of Research of Italy. It is derived from the grid point limited area meteorological model BOLAM (Buzzi et al., 1994) developed in the same insitute, from which GLOBO takes the numerical schemes and physical parameterizations. The general circulation model has been running experimentally since August 2009.

GLOBO implements a latitude-longitude coordinate system and a split-explicit time scheme[2].

The dynamical equation are integrated over a hybrid vertical coordinate system where the terrain-following coordinate σ $(0 < \sigma < 1)$ smoothly tends to a pressure coordinate p with height above the ground, according to:

$$p = p_0\sigma - (p_0 - p_S)\sigma^\alpha \ , \tag{4.1}$$

where p_0 is a reference pressure (tipically 1000 hPa), p_S is the surface pressure and α is a parameter that drives the transition from classical σ for $\alpha = 1$ (Phillips, 1957). The parameter α depends on the orography and, consequently, on resolution. It is limited by the relationship:

$$\alpha \leq \frac{p_0}{p_0 - \min(p_S)} \ , \tag{4.2}$$

---

[2] The use of explicit time scheme requires shorter time steps than semi-implicit and semi-Lagrangian methods but has the advantage of a much simpler implementation and a more accurate numerical description of the phase speed of gravity waves. The application of the domain decomposition to such a model is also straightforwardly done.

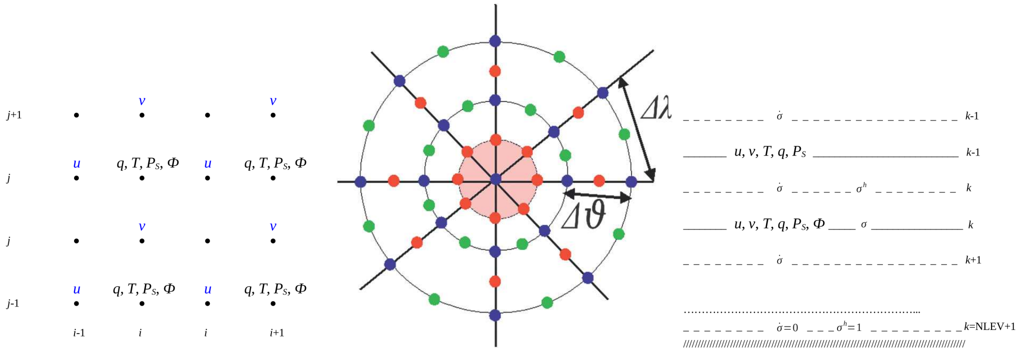

Figure 4.1: **Left**: Horizontal discretization of fields on the Arakawa-C grid of GLOBO. **Center**: Arakawa-C grid at the poles. Blue, red and green dots are T,U and V points, respectively. The red shaded area is the polar volume. **Right**: Vertical discretization of GLOBO field variables between σ integer and semi-integer levels.

which is satisfied by the typical setting $\alpha = 2$ used for a wide range of resolutions in GLOBO applications (Malguzzi et al., 2011).

The horizontal discretization is based on a staggered Arakawa-C grid. The north and south poles carry T points only.

Figure 4.1 shows a stencil of the Arakawa-C grid variable attribution, on the left, and the distribution of the field variables at the poles in the center.

In the vertical, the GLOBO prognostic variables are distributed on a Lorenz (1960) grid: all the quantities are defined on "integer" levels σ_i except vertical velocity, turbulent kinetc energy and mixing length and diffusion coefficients, which are located at "semi-integer" levels $\sigma_i^{(1/2)}$. The graphic on the right in fig. 4.1 shows the positions of the σ integer and semi-integer levels. The boundary condition for the velocity $\dot{\sigma}$, is $\dot{\sigma} = 0$ both at the bottom (semi-integer σ level NLEV+1) and at the top (semi-integer σ level 1).

In typical applications, GLOBO vertical grid is regularly spaced in σ, although it is possible to use a variable grid spacing as in its limited area version BOLAM (Buzzi et al., 1994). In the latter case, the position of the i-th ($i = 1, \mathrm{NLEV} + 1$) semi-integer level $\sigma_i^{(1/2)}$ in terms of σ coordinate, is defined by a quadratic polynomial function of the form:

$$\sigma_i^{(1/2)} = \beta\zeta + \gamma\zeta^3 + \delta\zeta^4 \ , \tag{4.3}$$

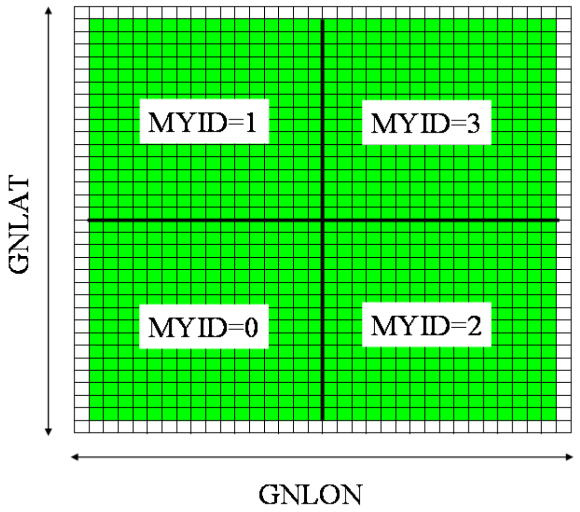

Figure 4.2: GLOBO domain parallelization. MYID is the processor identification number.

where $\zeta = i/(\text{NLEV} + 1)$ and the values of the parameters are usually $\beta = 0.78$, $\gamma = 1.44$ and $\delta = 1.22$.

GLOBO can be run on parallel architectures, and adopts a domain decomposition parallelization. The domain decomposition between processors is schematized in fig. 4.2. The prognostic variable values are distributed at the grid nodes, and the values at the boundaries (thick lines in the figure) are saved by all the neighboring processors.

4.4 Models implemented in this work

4.4.1 Subgrid Motion parameterization on LES fields

The velocity is divided into resolved and subgrid parts $\mathbf{u} = \mathbf{u}_R + \mathbf{u}_S$ with the hypotesis of statistical independence of the two parts $\langle u_{Ri} u_{Sj} \rangle = 0$.

The whole velocity field (see Eq. 1.34) is required to be consistent with Kolmogorov

(1941):

$$\langle \mathrm{d}u_i^2 \rangle \equiv \langle \mathrm{d}u_{Ri}^2 \rangle + \langle \mathrm{d}u_{Si}^2 \rangle \simeq C_0 \varepsilon \mathrm{d}t \ . \tag{4.4}$$

When it comes the computation of the subgrid velocity contribution, in Weil et al. (2004), the correlation functions for both the resolved and subgrid part of the velocity are assumed to have the same exponential form (Eq. 1.38), so that for small times:

$$\frac{R_R(t)}{\langle u_{Ri}^2 \rangle} = \frac{R_S(t)}{\langle u_{Si}^2 \rangle} \simeq 1 - t/T_L \ . \tag{4.5}$$

From Eqs. 4.4 and 4.5:

$$C_0 \varepsilon = \frac{2}{T_L} [\langle u_{Ri}^2 \rangle + \langle u_{Si}^2 \rangle] \tag{4.6}$$

With Eq. 4.6, a unique Lagrangian correlation time is assumed for the resolved and subgrid part.

Then, the authors identify $\langle u_i \rangle = u_{Ri}$, and $u_i' = u_{Si}$ in order to use the resolved velocity and the subgrid correlation tensor given by the LSM in Eq. 2.40 (Note that $\langle u_i' \rangle = 0$, whereas this is not true in general for $\langle u_{Si} \rangle$). Assuming a diagonal form of the covariance tensor for the subgrid velocities $\langle u_{Si} u_{Sj} \rangle = \langle u_S^2 \rangle \delta_{ij}$ the authors write, from Eqs. 4.4 and 4.6:

$$\overline{\mathrm{d}u_{Si}^2} = \frac{2\langle u_S^2 \rangle}{T_L} \mathrm{d}t \ , \forall i \ , \tag{4.7}$$

so that it results:

$$b^2 = \frac{2\langle u_S^2 \rangle}{T_L} \ , \tag{4.8}$$

and finally Eq. 2.40 reads:

$$\mathrm{d}u_{Si} = \left[-\frac{u_{Si}}{T_L} + \frac{1}{2} \frac{\partial \langle u_S^2 \rangle}{\partial x_i} + \frac{1}{2\langle u_S^2 \rangle} \frac{\mathrm{d}\langle u_S^2 \rangle}{\mathrm{d}t} u_{Si} \right] \mathrm{d}t + \left(\frac{2\langle u_S^2 \rangle}{T_L} \right)^{1/2} \mathrm{d}W_i(t) \ . \tag{4.9}$$

This is Eq. 15 with hypotesis Eq. 21 by Weil et al. (2004).

This approach makes a partition of the dissipation rate, partly due to the subgrid velocities, partly due to the resolved field. In this interpretation both $\mathbf{u}_R$ and $\mathbf{u}_S$ are treated as stochastic variables. This means that, in principle, the WMC is going to be satisfied if and only if all the possible realizations of resolved velocity field are sampled.

One shall consider the possibility of investigating dispersion around a single realization of the resolved velocity. WMC will be applied to the Eulerian *pdf* of the subgrid velocity, whereas the resolved part is considered deterministic.

Moreover one imposes the dissipative range to be characterised by the unique value of ε (see sec. 1.3.2).

The identification of resolved velocity with average velocity, fluctuating velocity with subgrid velocity, and the assumption of the diagonal form for the covariance tensor are made as in the previous model formulation.

Thus Eq. 2.40 with Eq. 1.34 leads to the following expression for $\mathrm{d}u_{Si}$:

$$\mathrm{d}u_{Si} = \left[-\frac{C_0\varepsilon}{2\langle u_S^2\rangle} u_{Si} + \frac{1}{2}\frac{\partial \langle u_S^2\rangle}{\partial x_i} + \frac{1}{2\langle u_S^2\rangle}\frac{\mathrm{d}\langle u_S^2\rangle}{\mathrm{d}t} u_{Si} \right] \mathrm{d}t + (C_0\varepsilon)^{1/2}\,\mathrm{d}W_i(t) \tag{4.10}$$

Note that Eq. 4.10 differs from Eq. 4.9 because of the first term in the drift coefficient and of the diffusion coefficient. Here, a new time scale appears:

$$T_S = \frac{2\langle u_{Si}^2\rangle}{C_0\varepsilon} \tag{4.11}$$

Eq. 4.10 can be rewritten introducing the timescale T_S to highlight the formal differences with eq. 4.9:

$$\mathrm{d}u_{Si} = \left[-\frac{u_{Si}}{T_S} + \frac{1}{2}\frac{\partial \langle u_S^2\rangle}{\partial x_i} + \frac{1}{2\langle u_S^2\rangle}\frac{\mathrm{d}\langle u_S^2\rangle}{\mathrm{d}t} u_{Si} \right] \mathrm{d}t + \left(\frac{2\langle u_S^2\rangle}{T_S} \right)^{1/2} \mathrm{d}W_i(t) \tag{4.12}$$

Eq. 4.12 is the same used in Vinkovic et al. (2006b).

4.4.2 Random displacement model implemented in IL-GLOBO

The Integrated Lagrangian GLOBO model, which has been implemented as part of this PhD, includes a module for the description of the vertical motion of particles. The equation, written for the particle Cartesian coordinate x_3, reads:

$$\mathrm{d}x_3 = \left(u_{R3} + \frac{\partial K}{\partial x_3} + \frac{K}{\langle\rho\rangle}\frac{\partial\langle\rho\rangle}{\partial x_3} \right) \mathrm{d}t + \sqrt{2K}\mathrm{d}W \tag{4.13}$$

Where u_{R3} is the resolved vertical velocity.

Another form of the equation can be written for the native σ coordinate of GLOBO:

$$\mathrm{d}\sigma = \left[\dot{\sigma} + \frac{K}{\rho}\frac{\partial\rho}{\partial\sigma} + \frac{\partial K}{\partial\sigma} + K\frac{\partial^2\sigma}{\partial x_3^2} \right] \mathrm{d}t + \sqrt{2K}\mathrm{d}W \tag{4.14}$$

where $\dot{\sigma}$ is the vertical velocity in the σ coordinate system and $x_3 = \Phi/g$.

The additional term appearing in the drift is due to the application of the the Itô chain rule (see Eq. 2.23), being not $\sigma(x_3)$ a linear function, in general.

The vertical Lagrangian coordinate σ is connected to the Lagrangian vertical position x_3 through Equation (4.1) and the hydrostatic relationship.

4.5 Structure of dynamical fields

4.5.1 LES output fields and settings

Settings

The LES run simulates the Convective Boundary Layer (CBL) over an homogeneous surface with a fixed heat flux $q_* = 0.24Km/s$ at the ground. The total integration time is 2 h with a time step of 0.25 s. The spatial grid is made of $128 \times 128 \times 128$ nodes and the model domain is about 4000 m $\times$ 4000 $m\times$ 2000 m with the following mesh lenghts:

$$\Delta x_1 = \Delta x_2 = 32\ m \quad \Delta x_3 = 15.5\ m \tag{4.15}$$

The geostrophic wind in the model is set to 0. The initial potential temperature is put constant and equal to 300 K from the ground to $925m$, then it presents a capping inversion of $8K$ $150m$ thick, and above it increases linearly of $3K/km$. A random homogeneous perturbation with amplitude $0.1K$ has been added at the initial time to the temperature field to activate turbulence.

After 1 hour the model reaches an almost steady condition. For the next 3600 s the three velocity components u_{R1}, u_{R2}, u_{R3} and the residual kinetic energy field e_S are recorded at 1 s intervals.

Velocity moments and spectra of the LES

The horizontally averaged kinetic energy profile of the LES is shown in Fig. 4.3 as function of height. Values are averaged horizontally and over the entire time of the available dataset (3600 s, 1 frame per second). The graphic shows the resolved velocity fields contribution to the energy, as well as the subgrid energy field profile and the total energy profile computed as:

$$e_T = \sum_{i=1}^{3} \frac{1}{2} u_{Ri}^2 + e_S \ . \tag{4.16}$$

The subgrid turbulent kinetic energy averaged considering only the mixing layer has a value of $\overline{e_S} = 0.25\ m^2/s^2$. Over the mixing layer top the total turbulent kinetic energy (e_T) strongly decreases, as expected. Considering the initial profile of potential temperature, an estimate for the CBL height is $h_i = 1000$ m, leading to $w_* = 2\ m/s$. In this work, the choice has been made to attribute the CBL height h_i according to the middle of the abrubpt decrease of kinetic energy shown in Fig. 4.3, leading to a value of $h_i = 1100$ m. The new h_i, substituted in eq. 1.45, leads to a $w_* = 2.06 \approx 2$. From Eq. 1.76, the value of $\bar{\epsilon}$ averaged in the mixing layer is $\bar{\epsilon} = 9\ 10^{-3} m^2/s^3$. All the three distributions display a maximun in the energy near the ground. This can be addressed to the horizontal shear produced by the eddies turnover, increasing both the variance of the horizontal velocities and the dissipation of energy due to the Eddy-Viscosity closure near the ground. It is worth noting that the first data level is 7.75 m above the ground ($1/2\ \Delta x_3$), so that the horizontal velocity is not forced to be null at that level. Figures 4.4, 4.5 and 4.6 show the resolved velocity moments of order 2, 3 and 4 respectively.

In Fig. 4.4 the second order velocity moments are plotted, normalized with w_*, as a function of the adimensional height x_3/h_i. Profiles are averaged over the entire sampled simulation time. The contribution of the filtered velocity has been assumed isotropic and added to the each component profiles as $2/3\ e_S$. The vertical velocity field variance has a maximum at $\approx 0.3h_i$ and goes to 0 at the ground. Variances of the horizontal components have maximum near the ground and at the top of the boundary layer, whereas in the body of the mixing layer $\langle u_1'^2 \rangle$ and $\langle u_2'^2 \rangle$ keep a constant value. As stated when commenting the kinetic energy profiles, maxima in the horizontal velocity components can be attributed to the eddy turnover near the ground and at the top of the mixing layer. From similarities of horizontal profile can be evinced the expected isotropy of the horizontal fields.

Fig.s 4.5 and 4.6 show the third and fourth order moments for the vertical velocities adimensionalized with w_* in the top plot, and the same moments normalized with the vertical velocity variance (skewness and kurtosis). The third order moment has a maximum located at $\approx 0.5h_i$, above the height of the second order one. The maxima of

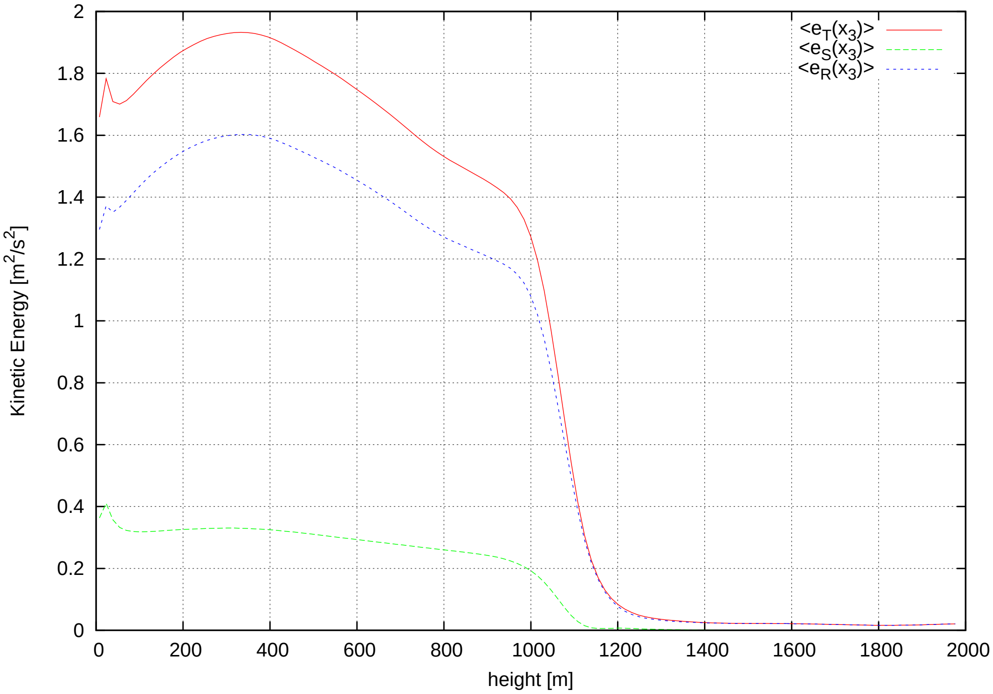

Figure 4.3: Total (red continuous line), subgrid (green dashed line) and resolved (blue dotted line) kinetic energy (averaged over horizontal planes) as function of height. Values averaged on the whole dataset.

the fourth order moment is at $\approx 0.4h_i$. The oscillations in skewness and kurtosis profiles for $x_3/h_i > 1$ are caused by the values of the normalizing vertical velocity variance approaching zero.

The fitting empirical functions shown in figures 4.4, 4.5 and 4.6 have been proposed by Lenschow et al. (1980) and Gryanik and Hartmann (2002), and have been modified slightly in order to better fit the LES data. Their expressions are:

$$\frac{\mu_2(\xi)}{w_*^2} = a_2\xi^{2/3}(1-b_2\xi)^2 \ \mathrm{cut}(\xi,d) \tag{4.17}$$

$$\frac{\mu_3(\xi)}{w_*^3} = a_3\xi(1-b_3\xi)^3(1+c_3\xi) \ \mathrm{cut}(\xi,d) \tag{4.18}$$

$$\frac{\mu_4(\xi)}{w_*^4} = a_4\xi^{4/3}(1-b_4\xi)^4(1+c_4\xi) \ \mathrm{cut}(\xi,d) \tag{4.19}$$

where $\xi = x_3/h_i$ is the adimensionalized height and the parameters take values $a_2 = 2.03$, $b_2 = 0.8$, $a_3 = 1.11$, $b_3 = 0.81$, $c_3 = 2.0$, $a_4 = 6.76$, $b_4 = 0.81$ and $c_4 = 1.5$. The function $\mathrm{cut}(\xi,d)$ is included to smoothly reduce the moments to 0 above the mixing layer height, were the function have not defined values. It has the form:

$$\mathrm{cut}(\xi,d) = \frac{1}{\pi}\left[\tan^{-1}(-(\xi-1)d) + \frac{\pi}{2}\right] \tag{4.20}$$

and $d = 30.0$.

Fig. 4.7 shows the logitudinal spectra of the LES velocity fields. The Fourier analysis is restricted to the lower 64 point of the domain, including most of the mixing layer. The ideal K41 spectrum is also shown, with $C_K = 1.0$, chosen as the best fitted value from inspections of compensated power spectra. Note that for wavenumbers larger than about $4\ 10^{-3}\ m$, corresponding to a spatial resolution of $4\Delta \sim 125\ m$, the spectra show less energy than the $k^{-5/3}$ inertial subrange.

The viscosity ν_T of the eddy-viscosity closure of the LES is described by Eq. 1.75, and introduces a Kolmogorov-like lengthscale:

$$\eta_S = \sqrt[4]{\frac{\nu_T^3}{\epsilon}} \tag{4.21}$$

Substituting the subgrid kinetic energy averaged over the whole model domain in Eq.

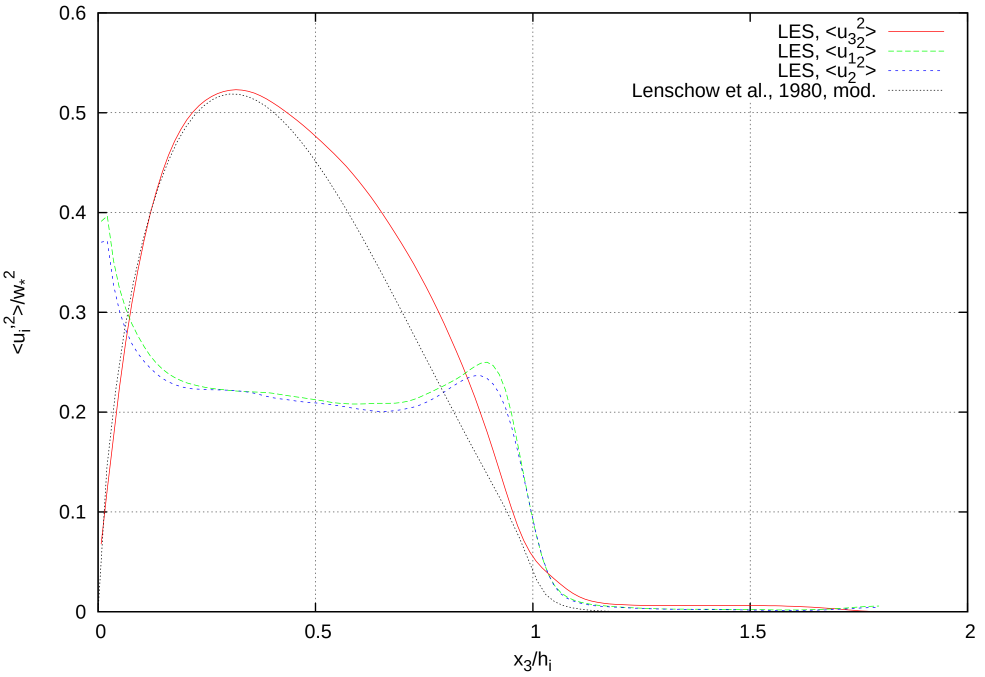

Figure 4.4: Second order velocity moments $\langle u_3'^2 \rangle$, $\langle u_1'^2 \rangle$, $\langle u_2'^2 \rangle$ and the empirical function proposed by (Lenschow et al., 1980) and slightly modified as shown in eq. 4.17.

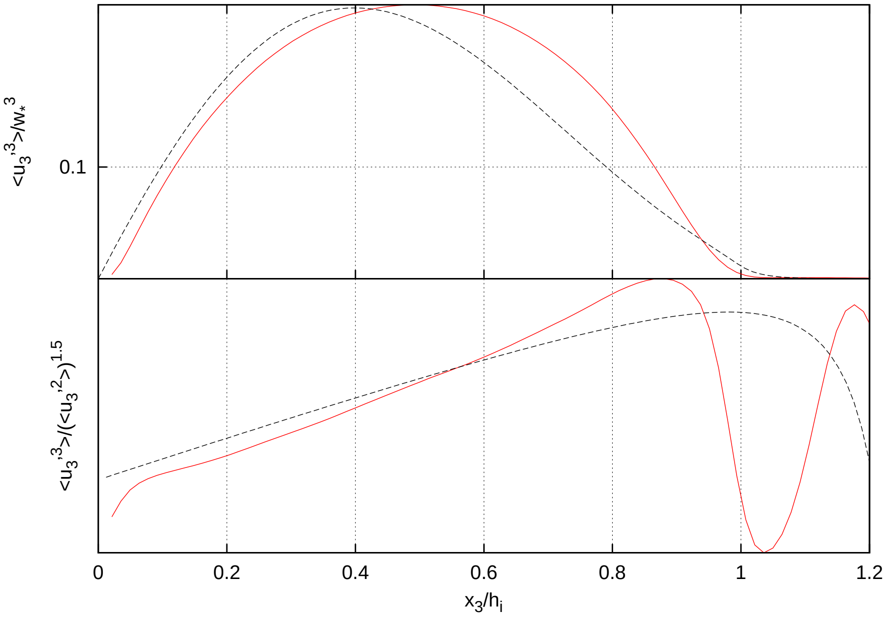

Figure 4.5: In the upper panel: third order velocity moment $\langle u_3'^3 / w_*^3 \rangle$ (red curve) and the empirical function proposed by (Lenschow et al., 1980) (black curve) and slightly modified as shown in eq. 4.18. In the lower panel: Skewness values of the same data.

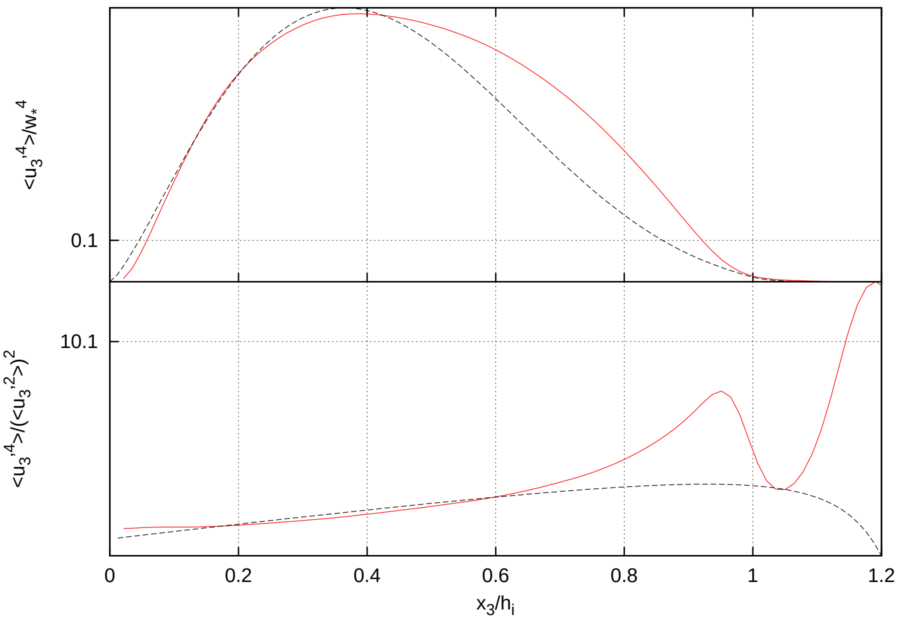

Figure 4.6: In the upper panel: fourth order velocity moment $\langle u_3'^4/w_*^4\rangle$ (red curve) and the empirical function proposed by (Lenschow et al., 1980) (black curve) and slightly modified as shown in eq. 4.19. In the lower panel: kurtosis values of the same data.

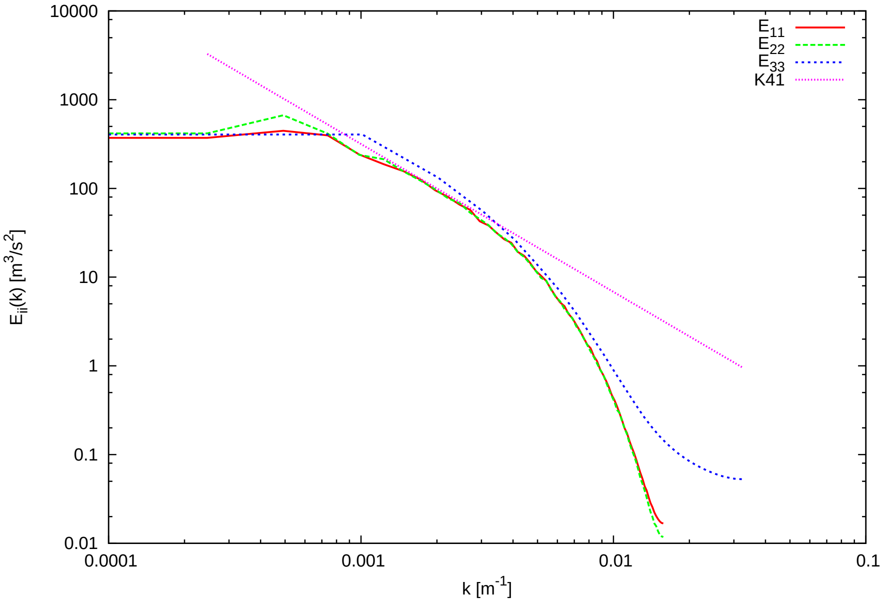

Figure 4.7: Longitudinal power spectra for the three velocity components as a function of k. Different linestyles refer to different components. The K41 spectrum is also reported, with $C_K = 1.0$

4.21 ($e_S \sim \overline{e_S}$), using also Eq.1.76 it results:

$$\nu_T \sim 0.5 \frac{m^2}{s} \tag{4.22}$$

and

$$\eta_S \sim 4.0m \tag{4.23}$$

Thus, the viscosity length scale is 1/4 of the resolution: the spectrum at large wavenumbers is thus consistent with a viscous decay, much larger than the inertial one.

4.5.2 Test run of GLOBO

GLOBO has been run with the low resolution settings with data of the period 03/11/2011 - 03/18/2011. The aim of this run has been the computation of the dynamical field profiles. GLOBO settings were those used for monthly forecast, with the horizontal grid of 362×242 cells and 50 vertical levels evenly spaced in σ.

Globally averaged vertical profiles of K, ρ and ϕ have been computed as a function of σ. The computation of profiles started after 6 h from the beginning of the run, and the profiles have been averaged for 6 h. Figures 4.8 and 4.9 report the K profile and the ρ and geopotential height ϕ/g average profiles, respectively.

The profiles have been fitted with analitical functions. With regard to the K profile, the function:

$$e(z) = Az \exp\left[-(Bz)^C\right] \tag{4.24}$$

has been used, with $A = 0.23$ determined according to GLOBO average surface-layer (the first GLOBO vertical level) and the other two parameters let to vary giving $B = 3.8\ 10^{-3}$ and $C = 1.3$. It can be observed that the given A corresponds to a friction velocity $u_* \simeq 0.5$.

Similarly, functions for profiles of the geopotential field ϕ and density field ρ have been adopted. These expressions are obtained by considering a fluid in hydrostatic equilibrium with a linearly decreasing temperature profile:

$$\phi(\sigma) = \frac{(\sigma^{(-R_d\Gamma/g)} - 1)T_0 g}{\Gamma} \tag{4.25}$$

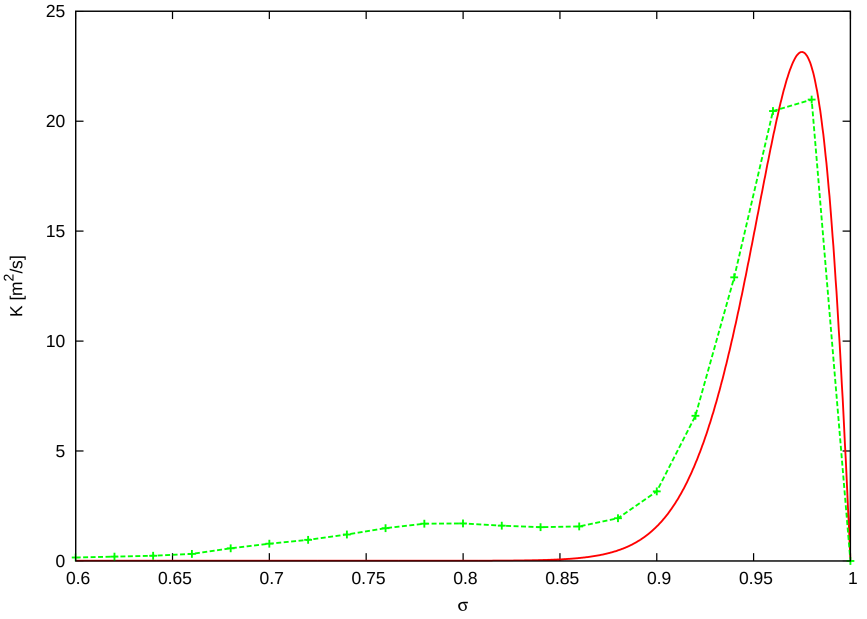

Figure 4.8: Diffusivity profiles. The green line with points shows the diffusivity profile K averaged over the model domain. The red curve represents the fit with the averaged data made with function 4.24.

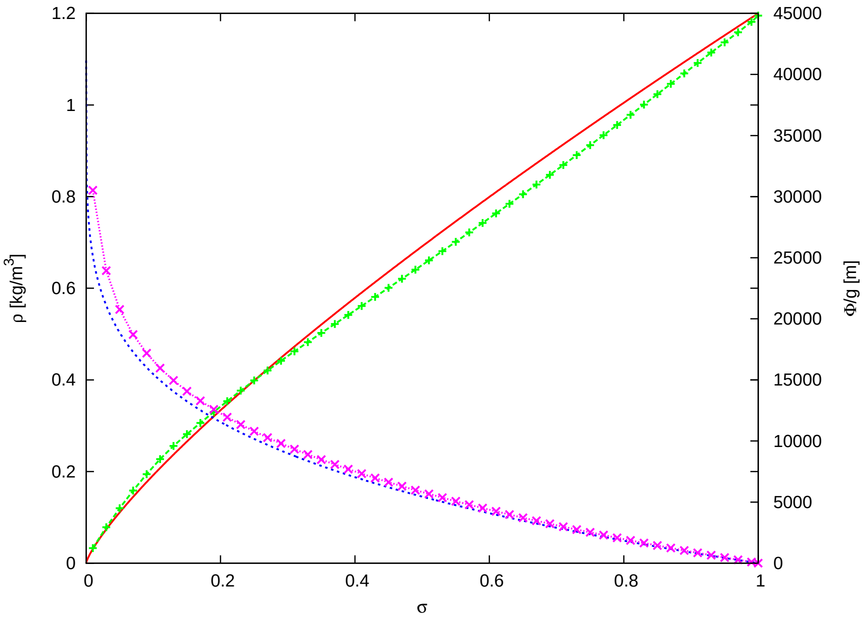

Figure 4.9: Profiles of ρ (green line) and ϕ (purple line) averaged over the whole GLOBO domain as a function of vertical coordinate σ. Also shown analitical approximation for the curves, defined by equations 4.26 and 4.25, respectively.

and

$$\rho(\sigma) = \rho_0 \left(\frac{(T_0 + \Gamma\ x_3(\sigma))}{T_0}\right)^{-(1+g/(R_d\ \Gamma))} \tag{4.26}$$

The fitting curves are obtained with values $T_0 = 288.0\ K$, $\rho_0 = 1.2 kg/m^3$, $\Gamma = -0.007 K/m$ and:

$$x_3(\sigma) = \frac{\phi(\sigma)}{g}\ . \tag{4.27}$$

It can be observed that, expressing the density ρ in sigma vertical units ($\rho_\sigma = \rho\,\left|\frac{\mathrm{d}z}{\mathrm{d}\sigma}\right|$), using Equations (4.25) and (4.26), it gives the constant value:

$$\rho_\sigma = \frac{\rho_0 R_d T_0}{g}\,. \tag{4.28}$$

4.6 Numerical implementation of the models

4.6.1 Interpolation and derivation

IL-GLOBO

IL-GLOBO implements both a linear interpolation scheme and an Akima (1991), and a third order polynomial scheme based on the Akima (1970) spline scheme, completed with the control for non negativity proposed by Fischer et al. (1991). These techniques are explained in details in section 3.3.5. The choice of Akima (1991, 1970) interpolation scheme provides an automatic consistency between field values and its first vertical derivatives in exchange to greater memory allocation and computational cost.

In the 3-D interpolation, in order to apply the 1-D Akima spline a 'slab model' approximation has been adopted, where in each horizontal cell the values of the interpolated field is considered constant with values averaged between adjacent points.

When the linear interpolation algorithm is applied, the first and second order derivatives are computed using a centered 3 point scheme, of order $\mathcal{O}(\Delta\sigma^2)$ and then interpolated linearly on the particle position σ_p. At the lower boundary ($\sigma = 1$, semi-integer level NLEV + 1) two different boundary condition can be imposed on the derivatives.

The first condition, given a generic field Ψ and a generic coordinate γ, requires that the first derivative at the ground is constant and computed as:

$$\frac{\partial\Psi}{\partial\gamma}|_{NLEV+1} = \frac{\Psi_{NLEV+1} - \Psi_{NLEV}}{\gamma_{NLEV+1} - \gamma_{NLEV}} \tag{4.29}$$

For the second condition, the value of the second derivative is considered constant and equal to its value at the level above:

$$\frac{\partial^2\Psi}{\partial\gamma^2}|_{NLEV+1} = \frac{\partial^2\Psi}{\partial\gamma^2}|_{NLEV}\,. \tag{4.30}$$

With this choice, the first order derivative at the ground is written as:

$$\frac{\partial\Psi}{\partial\gamma}|_{NLEV+1} = \frac{\partial\Psi}{\partial\gamma}|_{NLEV} + \frac{\partial^2\Psi}{\partial\gamma^2}|_{NLEV} * (\gamma_{NLEV+1} - \gamma_{NLEV})\,. \tag{4.31}$$

In the default configuration of IL-GLOBO, Eq.s 4.31 and 4.30 are adopted to compute derivative at the lower boundary for the density and geopotential, respectively. Derivative are computed using Eq. 4.29, instead, when dealing with the diffusivity field K. With this choice, the derivative is consistent with a linear profile of K near the ground.

Random Flight Model on LES

The interpolation of the LES field is made using a 3D linear interpolation.

The values of the derivative of the kinetic turbulent subgrid energy e_S at the boundaries are made considering the derivative to be 0. This choice is consistent both with the surface layer hypothesis and the fact that e_S goes to 0 above the mixing layer height.

4.6.2 Integration scheme

IL-GLOBO

IL-GLOBO implements two finite differences integration scheme, the Euler-Maruyama scheme and the Milstein scheme, for the equations 4.13 and 4.14. The details for these schemes are shown in section 3.2. The stochastic model is applied only on the vertical position.

At the boundaries, reflective condition on the σ or cartesian coordinate are adopted. Note that in case of non-homogeneous K at reflecting boundaries, a correct numerical implementation would require that Δt vanish as the particle approaches the boundary (Ermak and Nasstrom, 2000). With the dynamical timestep selection algorithm described in the following section, this necessity has been taken into account while mantaining a low computational cost.

IL-GLOBO is also parallelized in the same way of its parent model, GLOBO. When particles cross the boundaries of a processor domain, exiting and entering particles are transmitted to the other processor. Since the efficiency of parallelization strongly depends on the frequency of communications between processors during the run, the passage of particle is made only once per processor per dynamical model timestep (see table 4.1).

RFM-LES

All the Lagrangian random flight models using LES fields implement an Euler-Maruyama scheme (see sect. 3.2). The stochastic model integrate particle motion for the three dimensions. The equations implemented are eq. 4.9, 4.10 and the bi-Gaussian pdf equation described in eq.s 2.43 and 2.44.

The bi-Gaussian pdf equations adopt the MMI algorithm for the definition of a free parameter as described by Maurizi (1998). The model needs the prescription of third and fourth order moment profiles. In the first four level above the ground, for the sake of computational stability of the method, the velocity variance is considered constant and the moments of order 3 and 4 are considered to be Gaussian.

A reflective condition is applied for particle crossing vertical boundaries. The timestep used in the integration of the models has been considered sufficiently short for the need of well representing the boundaries (Wilson and Flesch, 1993).

On the horizontal, the domain of the LES have been considere periodical (as it is for the dynamical simulation itself), so boundary condition are not needed.

4.6.3 Selection of the timestep

The integration of the Langevin equation is not made on a fixed grid, so a condition like the Courant number do not exist.

In general, the finite difference approximation works well for a fixed timestep as much as the field is slow varying in the integration step length.

When dishomogeneities and strong gradients in the variable arise, the timestep limitation can become very strict. Some strategies are needed for obtaining an acceptable accuracy in computation while mantaining an affordable computational cost.

Dynamical time step selection for IL-GLOBO

The choice has been made for a dynamical timestep selection algorithm, that locally selects the time interval to use for the integration step.

Among the fields involved with the integration of eq. 4.14, the diffusion coefficient is by far the fastest changing. So the variation of the other fields can be neglected when evaluating the timestep conditions.

The first timestep constraint involve the diffusivity derivative and requires the time step satisfying the condition:

$$\sqrt{2K\Delta t_1} \ll K\left(\frac{\partial K}{\partial x_3}\right)^{-1} \tag{4.32}$$

(see, *e.g.*, Wilson and Yee, 2007) which expresses the fact that the average root-mean square step length must be much smaller than the scale of the variations of K.

The condition expressed by Equation (4.32) makes Δt_1 to vanish for $x_3 \to 0$. This behaviour ensures the WMC to be satisfied theoretically but clearly poses problems for numerical implementation (Ermak and Nasstrom, 2000; Wilson and Yee, 2007). A Δt_{min} need to be selected, small enough for the solution to be within the accepted error and, at the same time, large enough to not impact negatively on the overall computational cost.

Moreover, at maxima (or minima), Equation (4.32) give an unlimited Δt_1 which is not suitable for the integration of the model, because particle can have a large integration step where the fields are still rapidly varying.

To avoid this problem, a constraint is adopted, based on a spatial scale that gives an estimation of the width of the maximum, namely, the normalised second-order derivative:

$$2K\Delta t_2 = C_T K \left|\frac{\partial^2 K}{\partial z^2}\right|^{-1} \tag{4.33}$$

with $C_T \ll 1$. The above Equation has the property of limiting Δt_2 according to the strength of the peak of $K(z)$.

Taking the minimum among ΔT, Δt_1 and Δt_2, Equations (4.32) and (4.33)) give:

$$\Delta t = \min\left[\Delta T,\ \frac{C_T}{2}K\left(\frac{\partial K}{\partial z}\right)^{-2},\ \frac{C_T}{2}\left|\frac{\partial^2 K}{\partial z^2}\right|^{-1}\right] \tag{4.34}$$

where the paramter C_T quantifies the "much less" condition and, therefore, must be smaller than 0.1. No other arbitrary assumptions is needed to define this criterion. Its performances will be evaluated in subsequent sections.

Figure 4.10 shows the resulting integration timestep profile for the fitted average profile of GLOBO. The contribution of each term of eq. 4.34 is shown in a separate curve. It can be observed that at high levels, both constraints tends to the same value due to the vanishing of K and their derivatives, and at $\sigma \simeq 0.87$ they become larger than the Eulerian time step ΔT. Around the maximum of K, Δt_2 becomes small and dominates in Equation (4.34). Finaly, near the ground, the linear decrease of K with height, makes Δt_1 dominant.

A practical consideration has to be made about parallelization of the code. Because of the passage of particle between processors is made once per dynamical timestep (macrostep), the horizontal integration timestep cannot be easily reduced. Because of this, the integration of the Langevin equation is made first in the vertical direction for the duration of a macrostep, then particles are advected horizontally.

Timestep selection for RFM on LES fields

For a Langevin model of Markovian order 1, the relevant conditions for the selection of timestep can be written as (Thomson, 1987; Rotach et al., 1996; Schwere et al., 2002):

$$\Delta t_{max} = \min\left(\frac{\gamma^2\epsilon}{|u_3\partial\epsilon/\partial z|}, \frac{\gamma\sigma_{ui}}{a_{ui}}, \frac{\gamma^2\sigma_{ui}}{|u_3\partial\sigma_{ui}/\partial x_3|}, \left|\frac{u}{u_3\partial u/\partial z}\right|, \frac{\gamma^2\sigma_{u3}^2}{1/2b^2}\right) \tag{4.35}$$

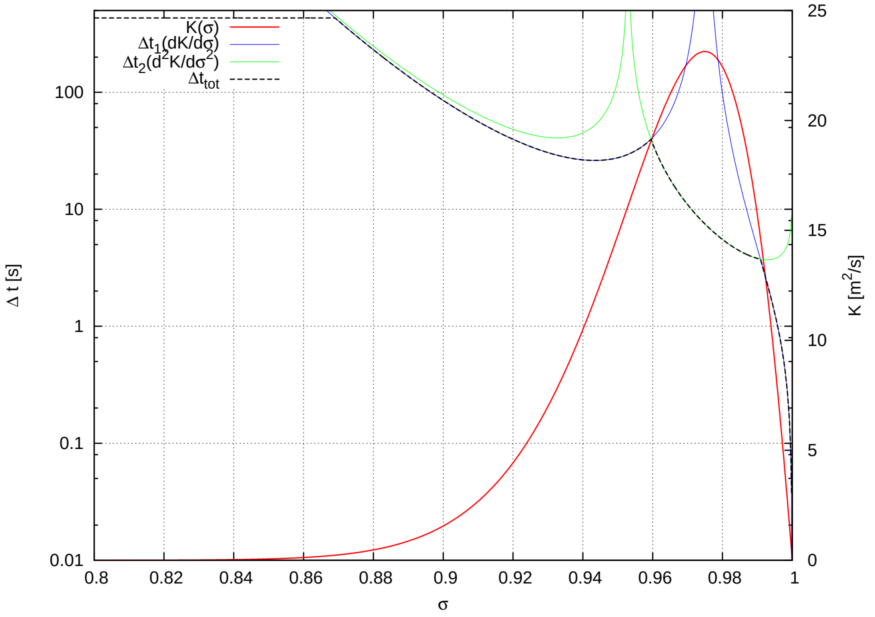

Figure 4.10: Contribution of the different requirements on the selection of integration timestep Δt. The green line shows the values for the second order derivative dependent condition (Eq. 4.33), the blue line describes the first order derivative dependent condition (Eq. 4.32), and the black dashed line shows the combined condition for the Δt (Eq. 4.34). The K profile is also shown, for reference (red line).

where $\gamma \ll 1$, a_{ui} and b are the drift and Wiener terms of the Langevin equation.

In the LPDM implemented in the LES, the timestep of 1 s, corresponding to the time lapse between the available fields, it has been found to be sufficiently short to obtain a sufficiently accurate integration. When necessity arises, the timestep is reduced for the whole model.

The possibility of the use of a dynamical timestep selection has been considered, but has not been implemented yet.

Chapter 5

Experiments

5.1 Introduction

This chapter describes the validation tests and results obtained with the models described in Chapter 4. The numerical experiments have been made with different purposes: the tuning of parameters for the numerical implementation (Sect. 5.3), the study of effects of different parameterizations on particle statistics (Sect. 5.4), the evaluation of the model consistency adopting different configurations (Sect. 5.5), and the comparation of model results with real experiments (Sec. 5.6).

5.2 Settings of the LPDM

5.2.1 Il-GLOBO

Given the difficulties and unknown factors arising during the testing of IL-GLOBO in its 3D version, a simplified 1-D model implementing the algorithms for the vertical dispersion of IL-GLOBO 3D has been used.

The model IL-GLOBO-1D runs offline with prescribed field profiles. Values of fields can both be interpolated from an array of data or computed analitically from prescribed functions.

The analytical functions used have been desctribed in Sect. 4.5.2, with the addition

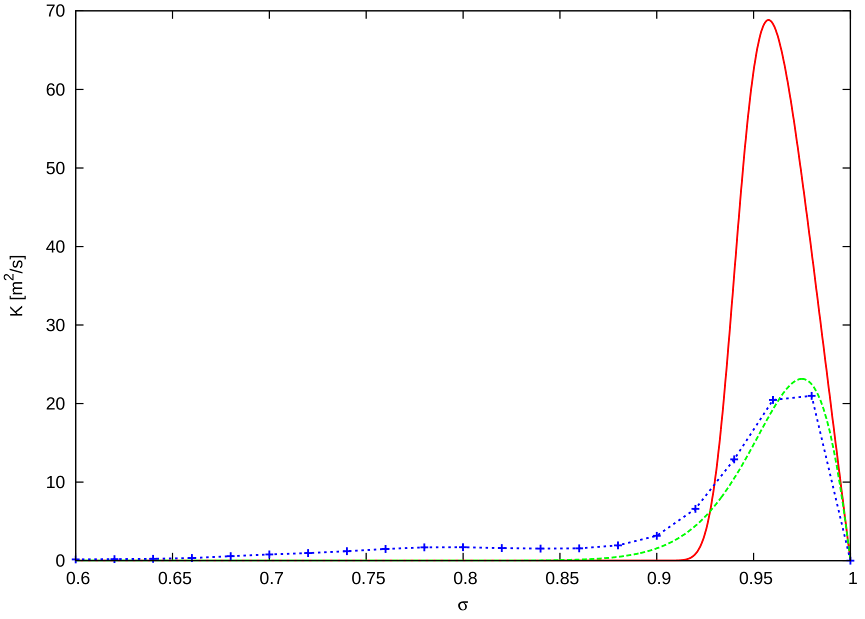

Figure 5.1: Diffusivity profiles. Blue lines with point show the average K profile in GLOBO averaged over the model domain. The curve in green represents the fit with the averaged data made with function 4.24. The red curve represents another, more peaked profile used to test the limit of the scheme.

of an alternative profile for K used to test the model in extreme situation. In fact, it has been observed that, locally, GLOBO sometimes display diffusivity profiles with isolated, strong maxima at the second level above the model surface. This second profile is obtained from Equation 4.24 with $B = 2.0\ 10^{-3}$ and $C = 5.0$. The profile is shown in figure 5.1.

5.2.2 Random Flight Model on LES data

For the Random Flight Model on LES data (RFM+LES) case, different settings for the Lagrangian model have been tested, in order to evaluate how the different models describe the statistical properties of the turbulence and how they perform in comparison with experiments.

Five different settings have been used.

- Model A : The motion of the subgrid part is neglected. Particles are solely driven by the resolved velocity field.
- Model E : Particle motion is driven by the resolved velocity field combined with a subgrid velocity computed by the model described by Eq. 4.10.
- Model F: Same as model E, but the subgrid velocity is computed using the Weil et al. (2004)-type subgrid model, Eq. 4.9.
- Model Ga: The model do not use directly the LES fields, but describe the particle motion using as input a vertical profile for the velocity variance (different for the 3 velocity components).

  A stochastic model with a gaussian pdf is prescribed for the horizontal velocities, and a bi-gaussian pdf is prescribed for the vertical velocities.

  The profiles are defined analitically by Equations: 4.17, 4.18 and 4.19. The functions are sampled on a grid with the same resolution of the LES model and the variable values are then interpolated during the run.
- Model Gn: The same as model Ga, but directly uses the horizontally averaged fields computed from the LES.

Note that, since for models Ga and Gn the subgrid velocity variance fields correspond to the total velocity variance field and so $T_S = T_L$, there is no distinction between the Weil et al. (2004) model and the other in that case.

During the first testings with model Gn, a large number of particle exiting the mixing layer was found. The problem could be addressed to the poor description of the variance gradient at the top of the boundary layer in the model or the to the presence of higher value of velocity variance above the limit of the CBL with respect to the fields used by the model Ga. None of the previous justification is completely satisfactory On one hand, the profile of velocity variance is, by its definition, the same of model E and F that, in turn, do not show this kind of problem. On the other hand, the Gradient of Ga, althought relative to an analytical function, is very similar to the one of Gn, and Ga too do not show any problem with the mixing layer limit. A possible explanation is that the non zero variance displayed by the vertical profile is the result of isolated and unconnected areas with positive variance in the 3D fields. Then, the profile of variance actually overestimate the dispersion properties in this area. This hypothesis has not been tested yet.

In any case, the results given by experiment Gn are clearly not suited to describe the dispersion in the CBL, and thus have been dismissed in the rest of this work.

5.3 Tuning of IL-GLOBO dynamic timestep selector

The first series of experiments with IL-GLOBO-1D concerns the optimization of the adaptive scheme for Δt, *i.e.*, the selection of the coefficient C_T (see Eq. 4.34).

Simulations were performed distributing particles with concentration proportional to ρ. For the WMC to be satisfied, this distribution must be statistically maintained as the time evolves. A number of about 400000 particles was used for all of the test. IL-GLOBO-1D have been run for a simulation time of 24 h. The density, geopotential and diffusivity distributions were defined by the analitical functions: Eq. 4.26, Eq. 4.25 and Eq. 4.24, respectively. The parameters of the diffusivity profiles are those of the fitted GLOBO average.

Note that, when expressed in a σ-coordinate defined from Eq. 4.25, the profile of density, defined in the cartesian coordinates by Eq. 4.26, becomes a constant.

For the simulations 4 cores of a Intel Xeon multi-CPU, multicore machine was used. Five different values of C_T have been tested, with values of 0.5, 0.1, 0.01, 0.001.

Concentration profiles have been computed by dividing the number of particle between 200 bins regularly spaced in σ. The deviation of the model from the WMC has been evaluated considering how much the particle distribution at the end of the run differed from the normalized (and constant in σ) density profile.

Figure 5.2 reports the different profiles of concentration after 24 hours of simulation for different values of C_T (Lower panel). The shaded area indicate the error within 3 standard deviations for the distribution of particles. Also reported in the figure the timestep profiles for the different choices of C_T and the diffusivity profile (upper panel).

Values of the RMSE are reported in Table 5.1 along with the computation time.

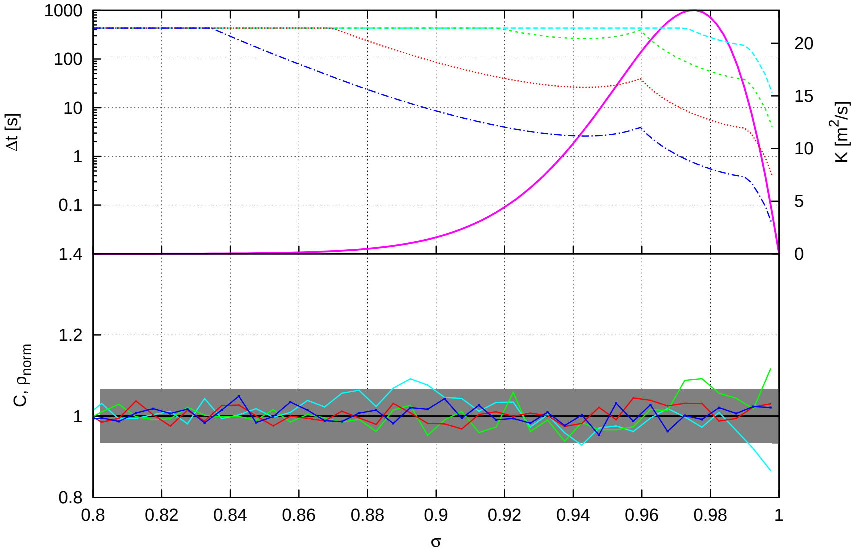

Figure 5.2: Top graphic: Timestep profiles for different choices of C_T: light blue $C_T = 0.5$, green $C_T = 0.1$, red $C_T = 0.01$, blue $C_T = 0.001$. The K profile is also shown. Bottom graphic: Normalized concentration profiles for different C_T (colors as defined above) and normalized density profile (horizontal black line). The shaded area indicates the error between 3 standard deviations.

Both experiments with $C_T = 0.01$ and $C_T = 0.001$ have the same value of RMSE. That value can be interpreted as the statistical limit given the number of particles and vertical resolution when computing the concentration.

Since results do not improve reducing the parameter below $C_T = 0.01$, this value have been chosen for all the following experiments.

5.4 Moments and statistics of RFM+LES for different configurations

A comparative study between the different model listed in Sect. 5.2.2 has been made with the purpose to evaluate their description of particle motion. The second, third

C_T	RMSE	Time [s]
0.5	0.044	76
0.1	0.037	238
0.01	0.021	1172
0.001	0.021	7317

Table 5.1: RMSE and execution time for different C_T.

and fourth order velocity moments, Lagrangian correlations and velocity pdfs have been evaluated for the models A, E, F and Ga.

The experiment have been made by dispersing 400000 particles homogeneously distributed in the mixing layer (including all the independent point in the horizontal periodic domain), between 8 m (the lower boundaries) and 1000 m. After 600 s, the particle have been considered having filled the mixing layer and reached equilibrium with the fields. Then, for 1200s the position and velocity values have been saved. The values have been sampled every second for the first 60 s, then every 10 second up to 600 s, then every 60 s.

Velocity moment profiles have been computed considering the particles between two vertical mesh point, and also averaging over time. The velocity pdfs have been computed similarly, obtaining a velocity pdf for every 15 m up to the mixing layer height.

Figures 5.3 and 5.4 show the model second and third order velocity moment profiles respectively. The values of the variance of A are lower, as expected, because of the absence of subgrid turbulent kinetic energy contribution.

Fluctuating values above $x_3/h_i = 1.1$ are due to the low number of particle in that area causing statistical noise. The effect do not appear in model Ga and with less intensity in model A because no particle reach that height.

In general, all models reproduce adequately well the velocity moments predicted, and thus are consistent with the Eulerian fields.

Examples of probability density function for the vertical velocity are shown in Fig. 5.5, for different heights. It is evident that, even if the biGaussian pdf modelled in experiment

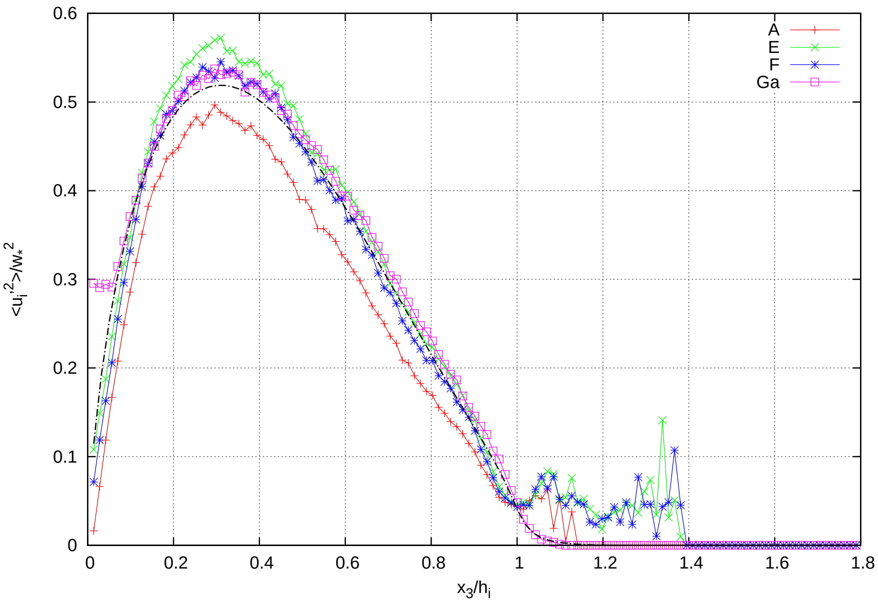

Figure 5.3: Vertical velocity variance profiles computed from Lagrangian velocities. Different colors denote different model settings: Red, mod. A; Green, mod. E; Blue, mod. F; purple, mod. Ga. Black line plot the analytical function Eq. 4.17

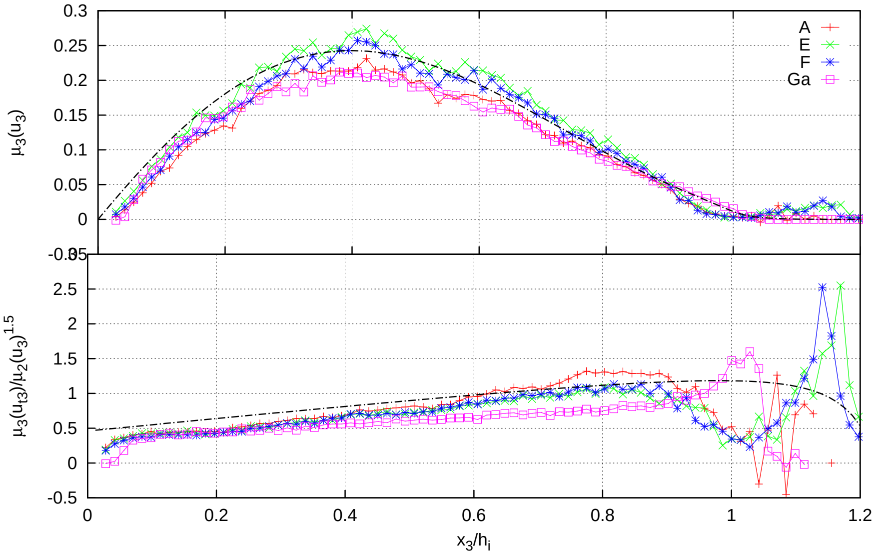

Figure 5.4: Upper panel Third order vertical velocity moment profile computed from Lagrangian velocities. Different colors denote different experiments: Red, mod. A; Green, mod. E; Blue, mod. F; purple, mod. Ga. Black line plot the analytical function Eq. 4.18. Lower panel: Same data and colours, but showing the skewness.

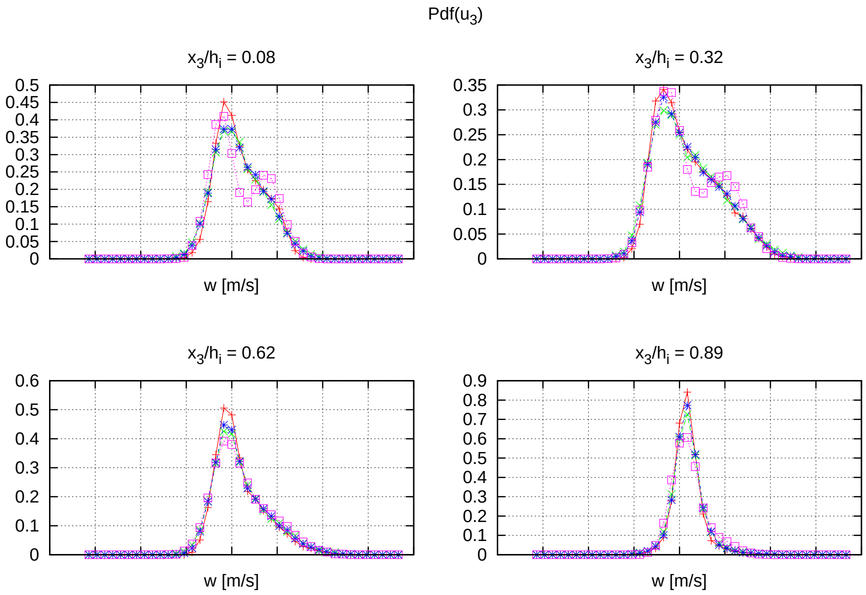

Figure 5.5: Probability density functions at 320m computed from tracer velocities. Different colors denote different experiments, as in Fig. 5.3

Ga represents well the velocity moments up to the fourth order, an unnatural bimodality is present.

The correlation functions have been computed by considering the i-th velocity component of the n-th particle at initial time as $u_i^{[n]}(t_0)$ and then, for each $t > t_0$, the correlation function is obtained as:

$$\tilde{R}(t-t_0;t_0) = \frac{1}{\sum_n \left(u_i^{[n]}(t_0)u_i^{[n]}(t_0)\right)} \sum_n \left(u_i^{[n]}(t-t_0)u_i^{[n]}(t_0)\right) \tag{5.1}$$

Where the sums are intended over the whole set of particles. The correlations have been computed separately for the subgrid, resolved and total velocity of the particle.

Results for the horizontal velocity are shown in Figure 5.6. From the values of ε, $\langle u_{Sh}^2 \rangle$ and $\langle u_{Rh}^2 \rangle$ $(h = 1,2)$ computed from the data shown in Fig.s 4.3 and 4.4 and using Eq.s 1.39 and 1.38, the expected values for the Lagrangian timescale adopted from models are: $T_S \sim 30\ s$ and $T_L \sim 100\ s$.

The correlations of the subgrid velocities are consistent with this prediction, with models Ga and F that well reproduce the Gifford (1982) correlation with Lagrangian timescale T_L, and model E that reproduces the same correlation function with Lagrangian timescale T_S.

Considering the correlation functions of the total velocity, it can be seen that the presence of a subgrid scale velocity reduces the correlation. It is interesting to notice that the final correlation function is not consistent with the total correlation timescale T_L, that has been computed from the dissipation rate ϵ coming from the same simulation.

Lagrangian correlations of vertical velocities also show the same correlation reduction for short times. The form of the correlation strongly differs from the Gifford (1982) because of the absence of homogeneity in the vertical direction.

5.5 IL-GLOBO 1D: Effects of the resolution on the WMC

One can expect that, indipendently from the timestep choice, the errors in the computation of the derivative and the ones produced during the interpolation can hinder the skill of a model in fullfilling the WMC.

A set of numerical experiments have been performed with the purpose of evaluating IL-GLOBO resolution requirements for maintaining consistency with the WMC.

Under the same experimental conditions described in Sect. 5.3, different resolutions have been tested.

The experiments have been set as follow. First, analytical fields were sampled on a grid, according to the resolution of each experiments. Then the IL-GLOBO-1D was run with the desired resolution, computing the field values with the linear interpolation algorithm as described in Sect. 4.6.1. The experiments tested both the GLOBO averaged and peaked diffusivity distribution.

The resolutions considered were (here expressed by the number of point of the σ array): 50 points (the same resolution of the GLOBO monthly forecast), 50 points on a non regular grid (with higher resolution near the ground), 100 points, 100 points on a non-regular grid, 200 points and 500 points.

Results for the GLOBO averaged diffusivity distribution (the green curve in Fig. 5.1) are shown in fig. 5.7. The experiment with interpolation over 50 regularly spaced points

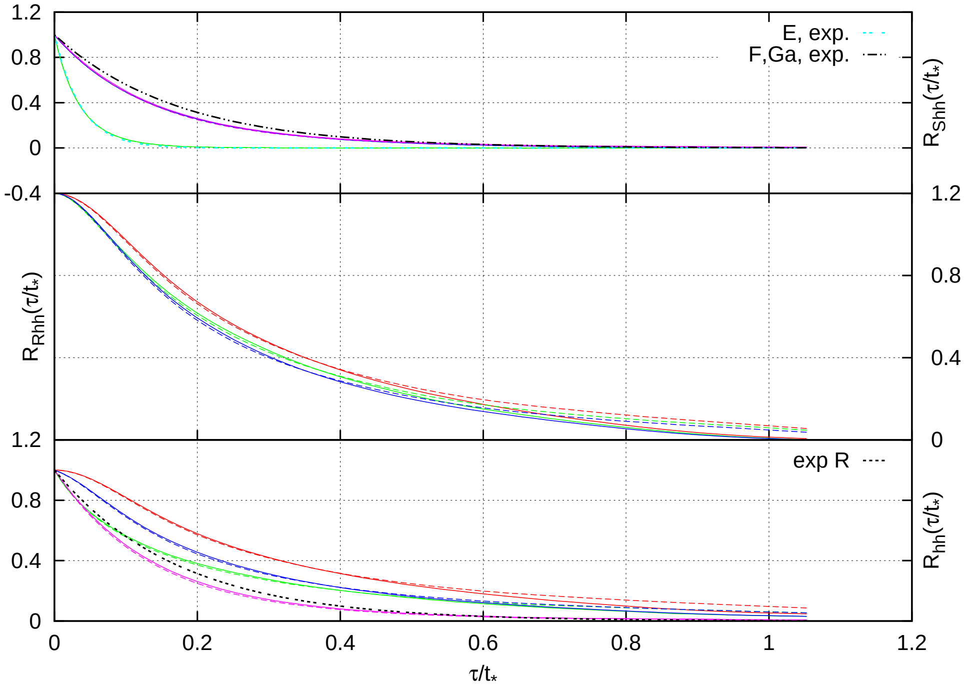

Figure 5.6: Lagrangian horizontal velocity correlations. In the upper panel, correlations of the subgrid velocity components. In the center panel, correlations of the resolved velocity components. In the lower pane, correlation of the total velocity components. Different colors denote different models: A, red; E, green; F, blue; Ga, purple. Also plotted the expected correlation function (eq. 1.38) given the integral Lagrangian timescale for each experiment.

shows accumulation of particle near the ground and above the diffusivity maximum. The experiment with 50 points on a non-regular grid perform better not accumulating particles near the ground thanks to the increased resolution, but has the same problem of the previous one for the higher levels. The other resolutions perform within the 3 standard deviation error-bar.

The accuracy of IL-GLOBO with the default resolution is thus near the limit of the description of the WMC for the average GLOBO diffusivity distribution.

Fig. 5.8 shows the results for the peaked diffusivity distribution (the red curve in Fig. 5.1). All the experiments clearly break the WMC. The problem has been addressed to inconsistency between the values of diffusivity and the values of its first derivative. The fact that also the 500 point resolution experiment is not WMC compliant suggests that the sensibility of the model to this error very high. A third set of tests have been executed using the Akima (1970) and Akima (1991) algorithms for the interpolation. These interpolation algorithm permit to compute analytically the values of the diffusivity derivatives. In this case, the experiments do not show any deviation from the WMC above the statistical limit, thus reinforcing the idea that the error in the WMC is due to the value-derivative inconsistency in the linear interpolation method.

The computational cost of the Akima (1970, 1991) and the linear interpolation algorithm have been compared. Model with Akima (1970, 1991) algorithms and the linear interpolation algorithms have been run with resolutions of 50 and 100 point with regularly spaced grid. The diffusivity distribution used was the GLOBO averaged. Results are reported in Tab. 5.2. The experiments using Akima (1970, 1991) interpolation respect the WMC for any resolution, and the computational time they require is higher of only $\sim 10\%$ with respect to the other one. This make the interpolation algorithm suitable for its implementation in 3D applications.

5.6 Experiments with localized source with the RFM

The models A, E, F, Ga have been tested comparing their predictions of absolute and relative dispersion of tracers in an experiment with localized sources with an equivalent real experiment.

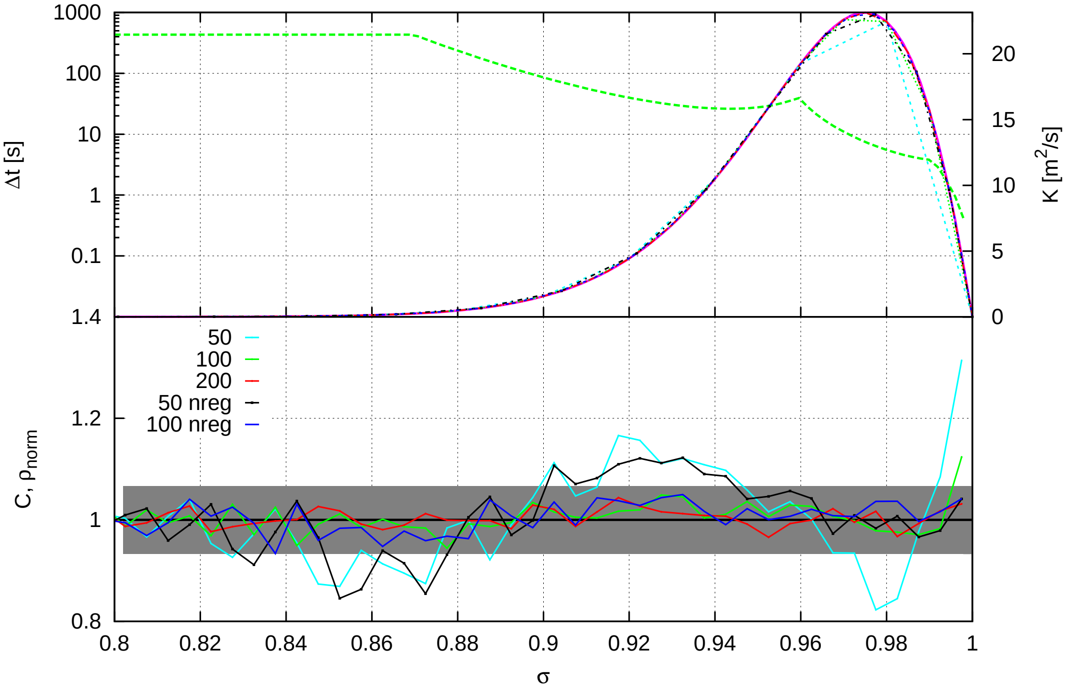

Figure 5.7: Numerical experiment with interpolated fields. GLOBO-Averaged diffusivity distribution. Upper panel: integration Δt profile and diffusivity profile. Lower panel: normalized concentration results for simulations at different resolution: 50 points (light blue), 100 points (green), 200 points (red), 50 points non regularly spaced (black), 100 points non regularly spaced (blue). The shaded area indicates the error between 3 standard deviations.

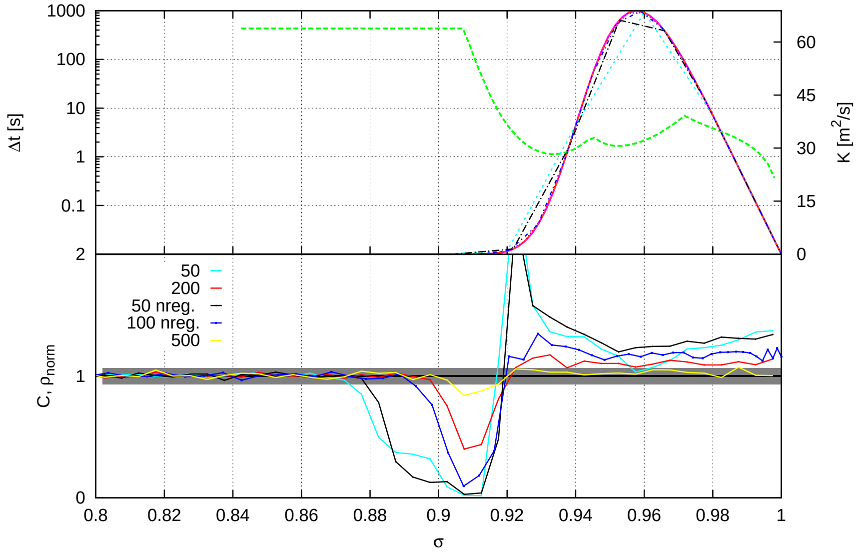

Figure 5.8: Numerical experiment with interpolated fields. Peaked diffusivity distribution. Upper panel: integration Δt profile and diffusivity profile. Lower panel: normalized concentration results for simulations at different resolution: 50 points (light blue), 100 points (green), 200 points (red), 50 points non regularly spaced (black), 100 points non regularly spaced (blue), 500 points(yellow). The shaded area indicates the error between 3 standard deviations. .

Interpolation algorithm	n. points	exec. time	rmsqe
Akima-70	50	332 s	0.024
Akima-91	50	327 s	0.023
Linear	50	293 s	0.097
Akima-70	100	582 s	0.022
Akima-91	100	578 s	0.022
Linear	100	497 s	0.059

Table 5.2: Computational cost and performance of numerical algorithms with Akima and linear interpolation, for different resolution settings.

The data used come from the water tank experiments of Weil et al. (2002) and Willis and Deardorff (1976).

5.6.1 Water tank experiments

The convection water tank had an initial temperature stratification, and the convection was driven by an electrically heated bottom surface. The h_i for the experiment was chosen as the height of intersection between the well mixed temperature profile and the linear temperature profile aloft.

In order to reproduce the dispersion downwind to a continuous source, since the tank had not a mean flow, the source was towed along one of its axis. The source emitted a mixture containing Rhodamine dye. A laser mounted outside the tank was towed with the same speed of the source in order to illuminate the transversal plane at a fixed distance downstream to the source.

Weil et al. (2002) estimated the velocity standard deviation in the mixed layer as:

$$\sigma_{ui} \sim 0.51 w_* \ , \tag{5.2}$$

and the Lagrangian timescale as:

$$T_L = 0.62 h_i / w_* \ . \tag{5.3}$$

Finally, the results of Weil et al. (2002) are expressed in nondimensional form using the relationship:

$$\hat{x} = \frac{w_* x}{U h_i} \ , \tag{5.4}$$

where U is the velocity of the mean flow.

5.6.2 Settings of the numerical experiments

The data of absolute dispersion, meandering, relative dispersion and concentration obtained from the water tank experiment are compared with the same quantities reproduced by our experiments.

In order to obtain a good sampling of the LES resolved fields, particles are emitted on spherical surfaces of radius of 8 m, with sphere centres distributed equally spaced on a grid of 128 x 128 point covering the whole horizontal surface. Each source consists of 64 particles. Experiments have been made with sphere centres starting at two different height: 0.32 h_i and 0.07 h_i. Results from emissions of 0.32 h_i are meant to be compared with relative dispersion and meandering data, the others with data of concentration profiles.

The data are adimensionalized using the equation:

$$t_* = tw_*/h_i \tag{5.5}$$

that is the instantaneous source equivalent adimensionalization of Eq. 5.4 (Weil et al., 2002).

Three different quantities have been computed. Elements of the theory of turbulent dispersion can be found in Sec. 1.5. For simplicity, in this section, we denote the root mean square meander in the i-th direction with σ_{mi}, the relative rms dispersion with σ_{ri} and the absolute dispersion with σ_{ai}. Let the position of a particle emitted in a given release (puff or cloud or particle) be x_{pi} and the position of the center of mass of each release be $\overline{x_{pi}}$. With the usual meaning of the ensemble mean for $\langle\cdot\rangle$, the above quantities are computed as:

$$\sigma_{mi}^2 = \langle(\overline{x_{pi}} - \langle\overline{x_{pi}}\rangle)^2\rangle \tag{5.6}$$

$$\sigma_{ri}^2 = \langle(x_{pi} - \overline{x_{pi}})^2\rangle \tag{5.7}$$

$$\sigma_{ai}^2 = \langle x_{pi}^2\rangle \tag{5.8}$$

Fig. 5.9 show the vertical rms meander normalized with h_i for model A, E and F. Model A shows the largest values of meandering, model F the smallest and model E gives results intermediate between the two. Fig. 5.10 shows normalized rms horizontal meander for data and numerical experiments. The data are overestimated by all the numerical models. F results are the nearest to the data. In both vertical and horizontal cases, a small scale velocity noise added to resolved velocity fields, has the effect to reduce the meander. This effect is stronger increasing the Lagrangian timescale of the subgrid velocity field.

From Fig. 5.10 can clearly be evinced an effect of anisotropy between the two horizontal component of the velocity field. The source of this behavior is not clear.

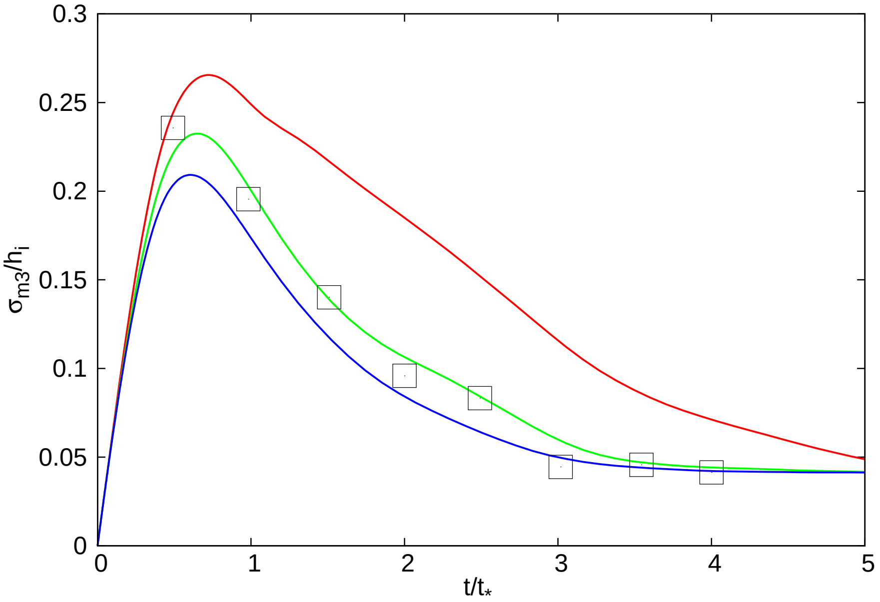

Figure 5.9: Vertical rms meander normalized with h_i, as function of the normalized timestep t/t_*. Black squares represent Weil et al. (2002) data. Different colors denote different models. Red, model A; green, model E; blue, model F.

The averaged velocity profile is nearly 0 for both u_{R1} and u_{R2}, and their variance profiles and correlation function are almost identical. The particles also are sampling all the horizontal domain. Its presence in all the experiment that included the resolved fields seem to point to an instantaneous inhomogeneity in the circulation. In the simulation the typical distance between two updraft is of $\approx 2000\ m$, implying that the domain of the LES is not large enough to avoid instantaneous fluctuations of the fields about their average. Since the particles are emitted at the beginning of the simulation in compact sources, and the meander increases at the initial time but remains constant for longer times (when particles are well mixed in the flow) an initial dishomogeneity could present itself without being eliminated (up to the limit of the domain) in the meandering statistics. This effect also disappear in the absolute dispersion statistics for long times, reinforcing this hypothesis.

The horizontal relative dispersion results are shown in Fig. 5.10. In order to highlight

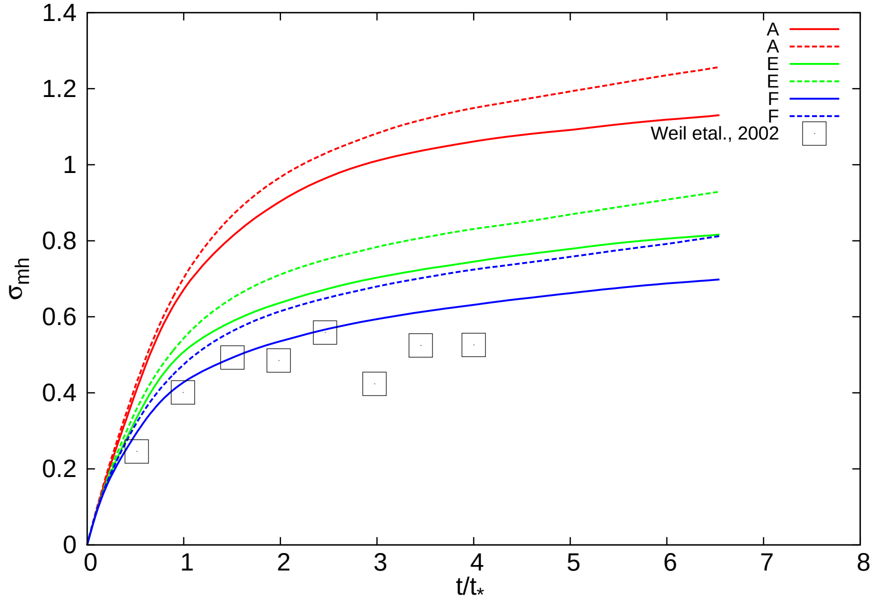

Figure 5.10: Horizontal rms meander normalized with h_i, as function of the normalized timestep t/t_*. Black squares represent Weil et al. (2002) data. Different colors denote different models. Red, model A; green, model E; blue, model F. Continuous lines denote direction σ_{m1}, dashed lines direction σ_{m2}.

the asymptotic behaviour of the dispersing particles, results have been normalized with the dispersion coefficients. In formula:

$$\sigma_{\lambda i*} = \frac{\sigma_{\lambda i}}{\sqrt{2\langle u_i^2 \rangle T_{Li} t}} \ , \tag{5.9}$$

where T_{Li} is the Lagrangian timescale relative to the i-th component of the velocity. The T_{Li} used in this operation have been computed as the Lagrangian integral timescale, i.e., integrating the correlation functions computed in the previous experiment (see Sect. 5.4).

With respect to the meandering case, the inclusion of a subgrid velocity parameterization have an opposite effect on relative dispersion statistics. Model F shows the highest values, followed by model E. Model A strongly underestimate the relative dispersion.

Even if none of the subgrid velocity model implemented in this work describes directly any relative dispersion effects, it enhance the initial growth of clouds of particle near to each other. Then the dishomogeneity in the resolved turbulence take place, thus increasing the relative dispersion.

Fig. 5.12 shows results for the absolute horizontal dispersion. The models describe adequately the long times asymptotic behaviour with an underestimation of the experimental data. The subgrid velocity parameterization can have a strong influence on the description of the meandering and relative dispersion, but not on the description of absolute dispersion, where the effect of largest eddies dominate.

Finally, fig. 5.13 shows the concentration profiles computed from the emission at 0.07 h_i compared with Weil et al. (2002) data. All the models using the LES resolved velocity field show a good accordance with the experimental data, but, among them, the best results are obtained from model A.

Model Ga shows an innatural double maxima feature in the concentration profile. Since both the first four velocity moments and the Lagrangian correlation are well simulated, we can address the problem to the anomalous form of Ga vertical velocity pdfs (see Fig. 5.5).

The accumulation of particle for $t_* = 2.55$ in model F and E has to be addressed to

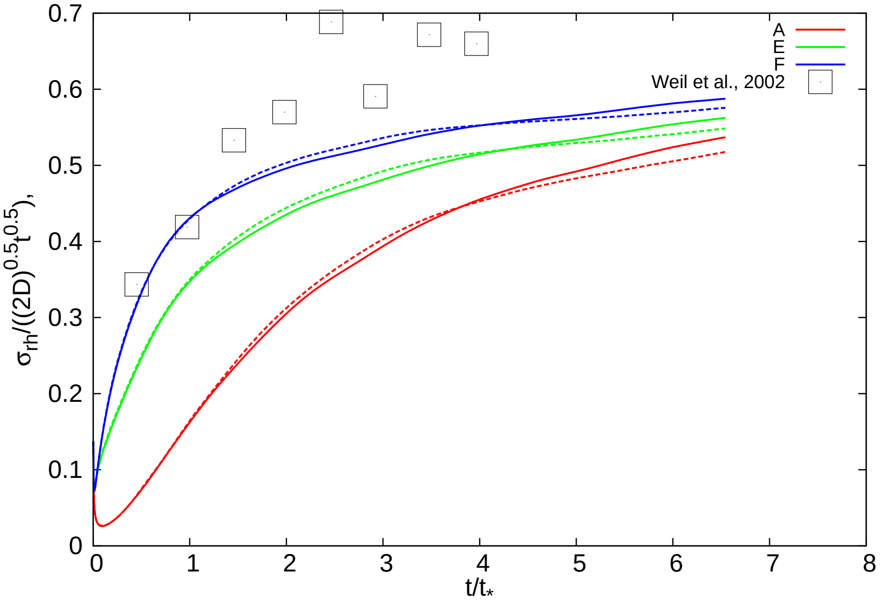

Figure 5.11: Horizontal relative rms dispersion normalized applying eq. 5.9, as function of the normalized timestep t/t_*. Black squares represent Weil et al. (2002) data. Different colors denote different models. Red, model A; green, model E; blue, model F. Continuous lines denote direction σ_{r1}, dashed lines direction σ_{r2}.

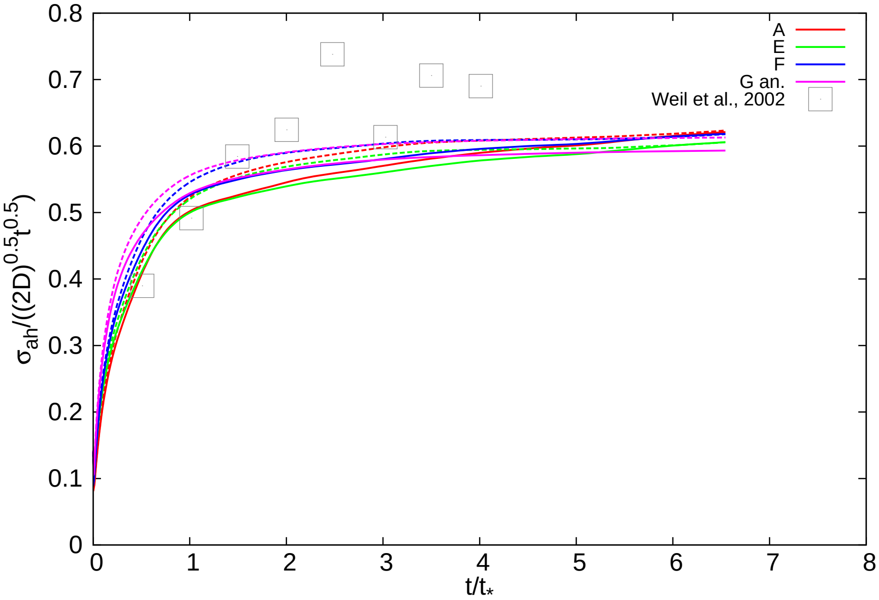

Figure 5.12: Horizontal absolute rms dispersion normalized with eq. 5.9, as function of the normalized timestep t/t_*. Black squares represent Weil et al. (2002) data. Different colors denote different models. Red, model A; green, model E; blue, model F; purple, model Ga. Continuous line denote direction σ_{a1}, dashed lines direction σ_{a2}.

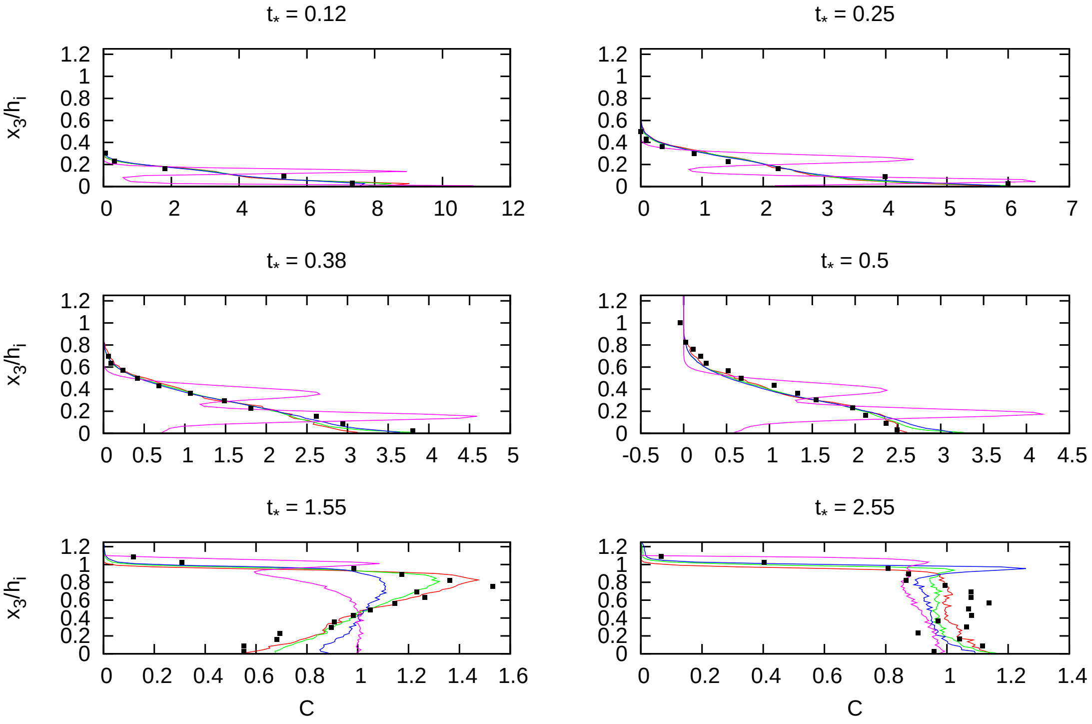

Figure 5.13: Concentration profiles of the numerical experiment compared with the data obtained by Weil et al. (2002). Different color denotes different experiments: red, model A; green, model E; blue, model F; purple, model Ga.

the choice of the integration timestep of 1s. This choice has been made to speed up the simulation, since the problem present itself only for long times.

Part III

Conclusions

Chapter 6

Conclusions

Lagrangian Particle Dispersion Models (LPDMs) driven by Eulerian model outputs have been studied and implemented in this work. The design of such models is strictly related to the type of the Eulerian model used. Since the dynamical model used in the description of the atmosphere do not describe the complete spectrum of the turbulent motions, but only the largest scales, and adopt physical parameterizations to describe the smaller ones, a very relevant part in the design of a LPDM is the modellization of unresolved motion. In this regard, basically, one has to choose between two different design strategies. The first is to implement a LPDM small scale closure consistently with the Eulerian model one. The other is to describe the unresolved motion with a parameterization that reproduce features expected from the small (subgrid) scale turbulence.

The dynamical models also describe the variable fields at discrete points in space, and the step used to integrate the equation of motion is selected on the basis of internal criteria. On the other hand, the LPDMs describe the flow as a continuum and, in general, they require an integration timestep computed considering their own features. Thus, methods for the Lagragian model integration and the interpolation of variables between grid points are the other aspects to consider when implementing models of this kind.

The present work aimed to study, develop and validate, some viable and efficient options for LPDM implementation using Lagrangian Stochastic Models (LSMs) for the description of unresolved motions. The primary requirement on which model are validated is the fullfillment of the Well Mixed Condition, namely, the properties of the simulated particle of keeping the same statistical distribution of flow particles once they reach it.

In order to compare methods for very different conditions, data of two dynamical models have been considered, namely a Large Eddy Simulation(LES) and a General Circulation Model(GCM).

Given the time and space scales of the GCM, the LSM implemented on it has been chosen to be of Markov order 0, consistent with the eddy-diffusivity closure of GLOBO. It also maintains the WMC in the general case of a variable density field. As input, it uses the dynamical model density, diffusivity and geopotential fields. The Lagrangian module reproduces the same code parallelization and its default implementation run online with the GCM, creating a fully integrated Eulerian-Lagrangian model.

In the case of the LES, a good amount of information on the subgrid field is known. The LES resolution lies inside the inertial subrange, and usually the statistical features of the fields are easily assessed. Because of this, the Lagrangian model paired with LES fields uses a LSM of Markov order 1 where the velocities at two different times can be correlated. This is not consistent with the LES parameterization of the subgrid motion effects, but should reproduce correctly the subgrid turbulence properties. The turbulent kinetic energy field produced by the LES gives information about the magnitude of small scale turbulence and its dissipation rate, but not on the finer characteristics of its structure, such as its correlation timescale and higher order moments. These information have to be evinced indirectly from the fields. In the literature, two different unresolved velocity parameterization have been proposed for this model: one considers the small scale motion having the same Lagrangian timescale of the large scale (our model F), and the other considers the dissipation to be specific of small scales and introduces a shorter timescale (our model E). The LPDM implements both of them in the aim to understand difference in their effect on the final description of turbulent dispersion.

The integration of the diffusive model shows some critical issues related to its computational efficiency and the robustness of its WMC compliance. This is due, on one hand, to the necessity for the model to cover a wide range of conditions (expecially regarding the shape of the diffusivity profiles produced by the GCM), and on the other hand, by the direct influence of the stochastic noise on the particle position. In order to implement the model, an efficient integration timestep selection algorithm has been developed and tested, which selects the step lengths on the base of the diffusion coefficient profile shape. During the WMC validation tests, the need for a consistency between diffusivity and its derivative is evidenced. Experimental results suggests that the linear interpolation algorithm is not able to produce values that let the LSM to fulfill the WMC if the diffusion coefficient profiles has strong variations. A computationally efficient modified Akima spline algorithm is shown to produce good results with only a moderate increase in the computational costs.

The Random Flight Model on LES fields seems to be less influenced by error in derivation and computation of fields when tested for its consistency with the WMC. As previously stated, since the parameterization for the unresolved velocity fields in the LES is required to reproduce formally the correct subgrid statistics (K41 compliance) it is not in general consistent with the eddy-viscosity LES closure. From this situation, necessity arises to select freely some statistical parameters of the subgrid field (in our case, the Lagrangian timescale). Model E and F have been compared in experiments of absolute and relative dispersion with the reference of experimental data. The absolute dispersion is poorly affected by the unresolved velocity parameterization chosen, and it is influenced only by the large scale motions. The unresolved scale velocities simulated by model E and F influence the relative dispersion and meandering, with the relative dispersion that increase as the Lagrangian timescale increase. The meander compensate this effect decreasing when relative dispersion increase. It can also be observed that, as expected, the stochastic noise imposed on the subgrid velocity has an effect on the reduction of the total Lagrangian correlation. It is not straightforward, althought, to evaluate quantitatively how the definition of a given Lagrangian timescale for the subgrid motion influences the total correlation (and thus, the total Lagrangian timescale). Furthermore, none between model E and F is shown to perform better when comparing numerical experiment results with real experiment ones. It can't be excluded that, given the highly detailed description of coherent eddy motion made by a LES of sufficiently high resolution, a simple stochastic model describing the absolute dispersion statistics is unfitted for giving a better representation of the turbulent motion.

As a concluding remark, we observe that many different model similar to the ones described in this work have been developed and used in many applications. Anyway, innovation can be stimulated by critical examination, and this work suggests that, in order to increase the performance skill of these Lagrangian models, the connection between the input-giving Eulerian model and the Lagrangian dispersion model should be accurately explored. An atmospheric dynamical model, not describing the full spectrum of real atmospheric motion, can produce only a peculiar representation of that motion. A LPDM can compensate for the Eulerian model approximation or can aim to a full consistency with their assumption. The first choice surely can give better results in (some) applications, while the second one should produce more predictable results, and, maybe, lead to a jointed improvement of both models.

Appendix A

FLEXPART and HYSPLIT implementation: an overview

In the last decade, a fair number of models for the description of trajectory in the atmosphere has been implemented and applied.

Some of these models are widely used on many problem and have been adapted to work on various data and implementation. Before describing the model implemented by the PhD candidate, a short review of implementation of two of the most popular and widely known model, HYSPLIT and FLEXPART, will be given.

These models can be used for deterministic trajectories (without subgrid models) or with modules for subgrid motion. Both backward and forward trajectories can be computed and the models are adaptable to different coordinate systems.

A.1 Unresolved vertical motion description

The unresolved motion in the PBL is computed introducing noise in the velocity fields by the introduction of a stochastic equation of Markov order 1. The expression for the Langevin equation is (Wilson et al., 1983; Thomson, 1987; Fay et al., 1995) :

$$d\left(\frac{w}{\sigma_w}\right) = -\frac{w}{\sigma_w}\frac{\mathrm{d}t}{\tau_w} + \frac{\partial \sigma_w}{\partial z}\mathrm{d}t + \frac{\sigma_w}{\rho}\frac{\partial \rho}{\partial z}\mathrm{d}t + \sqrt{\frac{2}{\tau_w}}\mathrm{d}W \tag{A.1}$$

The model implemented by HYSPLIT omits the third term on the rhs of eq. A.1, which include effects of density variations.

The finite difference algorithm implemented by both the models for the description of velocity fluctuation make the assumption that σ_w and τ_w take constant values along the partcle path for the integration step and update the vertical velocity with a single timestep using the integral formulation of eq. A.1.

HYSPLIT implements:

$$\begin{aligned}\left(\frac{w}{\sigma_w}\right)(t+\Delta t) = R_w(\Delta t)\left(\frac{w}{\sigma_w}\right)(t) + \tau_w(t)(1-R(\Delta t))\frac{\partial \sigma_w}{\partial z}(t) + \\ + \sqrt{(1-R_w(\Delta t)^2)}\zeta \qquad \text{(A.2)}\end{aligned}$$

whereas FLEXPART:

$$\begin{aligned}\left(\frac{w}{\sigma_w}\right)(t+\Delta t) &= R_w(\Delta t)\left(\frac{w}{\sigma_w}\right)(t) + \\ &+ \tau_w(t)(1-R(\Delta t))\left(\frac{\partial \sigma_w}{\partial z}(t) + \frac{\sigma_w(t)}{\rho(t)}\frac{\partial \rho}{\partial z}(t)\right) + \\ &+ \sqrt{(1-R_w(\Delta t)^2)}\zeta \qquad \text{(A.3)}\end{aligned}$$

Where ζ is a gaussian noise with zero mean and unit variance

For an integration timestep $\Delta t < 0.5\tau_w$ FLEXPART use the finite difference approximation of A.1 in order to save computational time.

A.2 Input fields and parameters. The PBL

In HYSPLIT, vertical Lagrangian timescale is defined as $\tau_w = 100s$. The horizontal $\tau_i = 1/f$

Velocity variances can be computed in two different ways. The first one consist in computing a mixing coefficient from momentum fluxes or, if not availables, from Richardson number [computed using the first two level (nearest to the ground) of the resolved fields] and stability functions (Troen and Mahrt, 1986; Holstag and Boville, 1993; Beljaars and Betts, 1993). The passage to velocity variances is then made by:

$$\sigma_j^2 = \frac{K_j}{\tau_j} \qquad \text{(A.4)}$$

With this option the diffusivity is obtained as a single averaged values for all the boundary layer (in the same vertical column).

The second way to compute σ_i values is to use Turbulent Kinetic Energy fields when available, following (Kantha and Clayson, 2000). In this case a value for the velocity variances is each PBL level.

FLEXPART computes u_*, θ_*, L_{MO} from surface and near-surface (model level 1-2) data. It then computes σ_i and τ_i as function of u_*, w_*, h_i, stability and z throught empirical relations (Hanna, 1982).

FLEXPART uses a qualitative scheme to compute the effective boundary layer height (H_{env}) in order to take into account topography and time variation effects:

$$H_{env} = h_i + \min(\sigma_Z, C_T V/N) \tag{A.5}$$

In the above equation σ_Z is the standard deviation of the dynamical model subgrid topography, $C_T = 2.0$ is a constant and V/N is the rate of wind speed V at h_i over Brunt-Vaisala frequency N (local Froude number).

The maximum H_{env} value of the grid points surrounding the particle position in space and time is taken, instead of interpolating it.

H_{env} is used in place of h_i for all FLEXPART computations.

A.3 Above the PBL

For taking account of vertical motion above the PBL, HYSPLIT compute a mixing coefficient defined as:

$$K = \mathfrak{l}^2 |\frac{\partial V}{\partial z}| \phi_h(l/L_{MO}) \tag{A.6}$$

where V is the meridional velocity, ϕ_h is the stability function (in the same form used for stable surface layer) and:

$$\mathfrak{l}^{-1} = kz^{-1} + 150^{-1} \tag{A.7}$$

l/L_{MO} is chosen as function of Ri_b.

In FLEXPART manual there is no mention of a value chosen for σ_w in the free troposphere.

A.4 Horizontal Motions

HYSPLIT computes a subgrid-scale horizontal mixing coefficient based on velocity deformation (Smagorinsky, 1963; Deardorff, 1973).

$$K_{hor} = \frac{1}{\sqrt{2}}(c\Delta X_d)^2 \sqrt{\left(\frac{\partial v}{\partial x} + \frac{\partial u}{\partial y}\right)^2 + \left(\frac{\partial u}{\partial x} + \frac{\partial v}{\partial y}\right)^2} \tag{A.8}$$

Where ΔX_d is the meteorological data grid size and $c = 0.14$.

In FLEXPART, the computation of horizontal velocity variances and Lagrangian timestep come from empirical relations similar to the one used in the vertical direction, as far as the PBL is concerned. The FLEXPART model includes also effects of mesoscale fluctuation. It solves an independent stochastic equation for the mesoscale velocity component. The mesoscale wind standard deviation is qualitatively defined as a constant c_m times the standard deviation of grid points surrounding the particle position. The Lagrangian timescale in the equation is chosen to be half of the time interval at which dynamical fields are available.

A.5 Choice of integration timestep

HYSPLIT requires a timestep which do not violate the condition

$$\Delta z_p < 0.5\Delta z_m \tag{A.9}$$

where Δz_m is the mesh length, and Δz_p is the particle displacement after a timestep. For this condition to be respected, it is required that:

$$\Delta t = \frac{(\Delta z)^2}{8\sigma_w^2 \tau_w} \tag{A.10}$$

FLEXPART has two option for timestep computation.

1. Do not adapt the computation timestep and simply use timestep of a synchroniziation time interval (usually 900 s)

2. Compute the timestep Δt as:

$$\Delta t = \frac{1}{c_{tl}} \min \left(\tau_w \, , \, \frac{h_i}{2w} \, , \, 0.5 \left(\frac{\partial \sigma_w}{\partial z} \right)^{-1} \right)$$

and fix a minimum timestep as 1 s for horizontal motion and $1/$*ifine* for vertical motion. *ifine* and c_{tl} are user defined parameters.

A.6 Deep Convection Effect Parametrization

FLEXPART deep convection effect scheme is based on the Emanule Zivkovic-Rothman scheme (Emanuel, 1991; Emanuel and Zivkovic-Rothman, 1999). When convection is triggered by the parametrization, a matrix $M_{i,j}$ is computed, which represents the saturated upward and downward mass fluxes within clouds.

The elements of the matrix $M_{i,j}$ are the mass fraction displaced from source level i to destination level j.

FLEXPART computes a probability matrix for the displacement of a particle in convective environment and then apply a Monte-Carlo scheme using the obtained probability matrix (Forster et al., 2007). The matrix is computed as the rate of mass displaced from level i to level j in a timestep Δt, $M_{i,j}\Delta t$, over the mass over square meter of the dynamical model, computed (from the hydrostatic relation) as:

$$m_i = (p_{i-1/2} - p_{i+1/2})/g \tag{A.11}$$

with $p_{i-1/2}$, $p_{i+1/2}$ are the pressure one-half level below and abole level i respectively, and g is gravity.

The probability $\mathcal{P}_{i,j}$ for a particle to be moved from level i to level j because of saturated up and downdraft for these scheme is:

$$\mathcal{P}_{i,j} = \frac{M_{i,j}\Delta t}{m_i} \tag{A.12}$$

The Monte-Carlo scheme extracts a random number $\eta \in [0, 1]$ and the particle is displaced at the level j_d at which

$$\eta < \sum_{j=jb}^{jd} \mathcal{P}_{i,j} \tag{A.13}$$

is first satisfied, where j_b is the lowest cloud level.

In order to obtain a mass conserving scheme, FLEXPART model assumes that saturated up- and down-drafts in the cloud are compensated by a subsidence mass flux in the cloud-free environment. After the Monte-Carlo algorithm is used, the saturated mass flux are computed at each level and a compensating velocity acts on the particle that have not been displaced from their initial level.

Bibliography

, 1924: *Differentialgleichung fur die turbulente Bewegung einer kompressiblen Flussigkeit*, Delft.

Akima, H., 1970: A new method of interpolation and smooth curve fitting based on local procedures. *J. of the Association for Computing Machinery*, **17**, 589–602.

Akima, H., 1991: A method of univariate interpolation that has the accuracy of a third-degree polynomial. *ACM Transactions on Mathematical Software*, **17**, 341–366.

Antonelli, M. and R. Rotunno, 2007: Large-eddy simulation of the onset of the sea breeze. *J. Atmos. Sci.*, **64**, 4445–4457.

Beljaars, A. and A. K. Betts, 1993: Validation of the boundary layer representation in the ecmwf model. *Proceedings, ECMWF Seminar of Validation of Models over Europe*, **II**, 159–195.

Buzzi, A., M. Fantini, P. Malguzzi, and P. Nerozzi, 1994: Validation of a limited area model in cases of mediterranean cyclogenesis: surface fields and precipitation scores. *Meteorol. Atmos. Phys.*, **53**, 137–153.

Cai, X. and M. Y. Leclerc, 2006: Forward-in-time and backward-in-time dispersion of the convective boundary layer: the concentration footprint. *Boundary-Layer Meteorol.*, **123**, 201–218.

Cape, J. N., J. Methven, and L. E. Hudson, 2000: The use of trajectory cluster analysis to interpret trace gas measurements at mace head, ireland. *Atmospheric Environment*, **34**, 3651–3663.

Catalano, F. and C.-H. Moeng, 2010: Large-eddy simulation of the daytime boundary layer in an idealized valley using the weather research and forecasting numerical model. *Boundary-layer Meteorology*, **137**, 49–75.

Chandrasekar, S., 1961: *Hydrodynamic and hydromagnetic stability*, Oxford University Press.

Clark, R. A., J. H. Ferziger, and W. C. Reynolds, 1979: Evaluation of subgrid-scale models using an accurately simulated turbulent flow. *J. Fluid Mech.*, **91**, 1–16.

Csanady, G. T., 1973: *Turbulent diffusion in the environment*, D. Reidel Pu. Co., Dordrecht.

Damoah, R., N. Spichtinger, C. Forster, P. James, I. Mattis, U. Wandinger, S. Beirle, T. Wagner, and A. Stohl, 2004: Around the world in 17 days hemispheric-scale transport of forest fire smoke from russia in may 2003. *Atmos. Chem. Phys.*, **4**, 1311–1321.

Deardorff, J. W., 1973: Three-dimensional numerical modeling of the planetary boundary layer. *Workshop on Micrometeorology*, 271 – 311.

Deardorff, J. W., 1974: Three-dimensional numerical study of the height and mean structure of a heated planetary boundary layer. *Bound. Layer Meteorol.*, **7**, 81–106.

Dosio, A. and J. V. G. de Arellano, 2006: Statistics of absolute and relative dispersion in the atmospheric convective boundary layer. *J. Atmos. Sci.*, 1253–1272.

Dosio, A., J. V. G. de Arellano, A. A. M. Holstag, and P. J. H. Builtjes, 2003: Dispersion of a passive tracer in buoyancy and shear driven boundary layers. *J. Appl. Meteorol.*, 1116–1130.

Durbin, P. A., 1980: A stochastic model for two-particle dispersion and concentration fluctuations in homogeneous turbulence. *J. Fluid Mech.*, **100**, 279–302.

Emanuel, K. A., 1991: A scheme for representing cumulus convection in large-scale models. *J. Atmos. Sci.*, **48**, 2313–2335.

Emanuel, K. A. and M. Zivkovic-Rothman, 1999: Development and evaluation of a convection scheme for use in climate models. *J. Atmos. Sci.*, **56**, 1766–1782.

Ermak, D. L. and J. S. Nasstrom, 2000: A lagrangian stochastic diffusion method for inhomogeneous turbulence. *Atmospheric Environment*, **34**, 1059–1068.

Fay, B., H. Glaab, I. Jacobsen, and R. Schrodin, 1995: Evaluation of eulerian and lagrangian atmospheric transport models at the deutscher wetterdienst using anatex surface tracer data. *Atmos. Environ.*, **29**, 2485–2497.

Fischer, B., G. Opfer, and M. L. Puri, 1991: A local algorithm for constructing non-negative cubic splines. *J. Approx. Theory*, **64**, 1–16.

Forster, C., A. Stohl, and P. Seibert, 2007: Parameterization of convective transport in a lagrangian particle dispersion model and its evaluation. *Journal of Applied Meteorology and Climatology*, **46**, 403.

Franzese, P., A. K. Luhar, and M. S. Borgas, 1999: An efficient Lagrangian stochastc model of vertical dispersion in the convective boundary layer. *Atmos. Environ.*, **33**, 2337–2345.

Gardiner, C. W., 1990: *Handbook of Stochastic Methods for Physics, Chemistry and the Natural Sciences*, 2nd ed., Springer-Verlag.

Gifford, F. A., 1982: Horizontal diffusion in the atmosphere: a Lagrangian-dynamical theory. *Atmos. Environ.*, **15**, 505–512.

Gregory, J. A., 1986: Shape preserving spline interpolation. *Computer-aided Design*, **18**, 53–57.

Grell, G. A., S. E. Peckham, R. Schmitz, S. A. McKeen, G. Frost, W. C. Skamarock, and B. Eder, 2005: Fully coupled "online" chemistry within the wrf model. *Atmos. Environ.*, 6957–6975.

Gryanik, V. and J. Hartmann, 2002: A turbulence closure for the convective boundary layer based on a two-scale mass-flux approach. *Journal of the Atmospheric Sciences*, **59**, 2729–2744.

Hanna, S. R., 1982: *Application in air pollution modelling*, D. Reidel Publishing Company, Dordrecht, Holland.

Haszpra, T. and T. Tel, 2011: Volcanic ash in the free atmosphere: A dynamical systems approach. *J. Phys.: Conf. Ser.*, **333**.

Henn, D. S. and R. I. Sykes, 1992: Large-eddy simulation of dispersion in the convective boundary layer. *Atmos. Environ.*, **26**, 3145–3159.

Holstag, A. A. M. and B. A. Boville, 1993: Local versus nonlocal boundary-layer diffusion in a global climate model. *J. Climate*, **6**, 1825–1842.

Hussain, M. Z. and M. Sarfraz, 2008: Positivity preserving interpolation of positive data by rational cubics. *J. of Computational and Applied Math.*, **218**, 446–458.

Izquierdo, R., J. Belmonte, A. Avila, M. Alarcón, E. Cuevas, and S. Alonso-Perez, 2011: Source areas and long-range transport of pollen from continental land to tenerife (canary islands). *Int. J. Biometeorol.*, **55**, 67–85.

Kantha, L. H. and C. A. Clayson, 2000: *Small Scale Processes in Geophysical Fluid Flows*, vol. 67 of *International Geophysics Series*, Academic Press, San Diego, CA.

Kloeden, P. E. and E. Platen, 1992a: Higher-order implicit strong numerical schemes for stochastic differential equations. *J. of Statistical Physics*, **66**, 283–314.

Kloeden, P. E. and E. Platen, 1992b: *Numerical Solution of Stochastic Differential Equations*, no. 23 in Applications of Mathematics, Springer-Verlag.

Kolmogorov, A. N., 1941: The local structure of turbulence in incompressible viscous fluid for very large Reynolds numbers. *Dokl. Akad. Nauk SSSR*, **30**, 301.

Lamb, R. G., 1978: A numerical simulation of dispersion from an elevated point source in the convective planetary boundary layer. *Atmospheric Environment*, **12**, 1297–1304.

Landau, L. D. and E. M. Lifshitz, 1959: *Fluid mechanics*, vol. 6 of *Course of theoretical physics*, Pergamon Press.

Lenschow, D. H., J. C. Wyngaard, and W. T. Pennel, 1980: Mean field and second moment budgets in a baroclinic, convective boundary layer. *J. Atmos. Sci.*, **37**, 1313–1326.

Leonard, A., 1975: Energy cascade in large-eddy simulations of turbulent fluid flows. *Adv. in Geophysics*, **18**, 237–248.

Lilly, D. K., 1966: On the application of the eddy viscosity concept in the inertial subrange of turbulence, NCAR Tech. Rep. 123, National Center for Atmspheric Research, 18 pages.

Liu, S., C. Meneveau, and J. Katz, 1994: On the properties of similarity subgrid-scale models as deduced from measurements in a turbulent jet. *J. Fluid Mech.*, **275**, 83–119.

Lloyd, S., 2000: Ultimate physical limits to computation. *Nature*, **406**, 1047–1054.

Lorenz, E. N., 1960: Energy and numerical weather prediction. *tellus*, **12**, 364–373.

Luhar, A. K. and R. E. Britter, 1989: A random walk model for dispersion in inhomogeneous turbulence in a convective boundary layer. *Atmos. Environ.*, **23**, 1911–1924.

Malguzzi, P., A. Buzzi, and O. Drofa, 2011: The meteorological global model globo at the isac-cnr of italy assessment of 1.5 yr of experimental use for medium-range weather forecasts. *weather and forecasting*, **26**, 1045–1055.

Maurizi, A., 1998: A new probability density function closure model for lagrangian stochastic dispersion simulation. *Air Pollution VI: Modelling, monitoring, management*, 879,888.

Meneveau, C. and J. Katz, 2000: Scale-invariance and turbulence models for large-eddy simulation. *Annu. Rev. Fluid Mech.*, **32**, 1 – 32.

Moeng, C.-H., 1984: A large-eddy-simulation model for the study of planetary boundary-layer turbulence. *journal of the atmospheric science*, **41**, 2052–2062.

Moeng, C.-H., J. Dudhia, J. B. Klemp, and P. P. Sullivan, 2007: Examining Two-Way Grid Nesting for Large Eddy Simulation of the PBL Using the WRF model. *Mon. Wea. Rev.*, **135**, 2295–2311.

Moeng, C.-H. and J. C. Wyngaard, 1988: Spectral analysis of large-eddy simulations of the convective boundary layer. *J. Atmos. Sci.*, **45**, 1573–1587.

Monin, A. S. and A. M. Yaglom, 1971: *Statistical fluid mechanics*, vol. I, MIT Press, Cambridge, 769 pp.

Monin, A. S. and A. M. Yaglom, 1975: *Statistical fluid mechanics*, vol. II, MIT Press, Cambridge, 874 pp.

Ouellette, N. T., H. T. Xu, M. Bourgoin, and E. Bodenschatz, 2006: Small-scale anisotropy in lagrangian turbulence. *New Journal of Physics*, **8**.

Phillips, N. A., 1957: A coordinate system having some special advantages for numerical forecasting. *Journal of Meteorology*, **14**, 184185.

Pope, S., 2000: *Turbulent Flows*, Cambridge University Press.

Prandtl, L., 1925: Bericht uber untersuchungen zur ausgebildeten turbulenz. *Zs. angew. Math. Mech.*, **5**, 136–139.

Press, W. H., S. A. Teukolsky, W. T. Vetterling, and B. P. Flannery, 1992: *Numerical Recipes in FORTRAN*, 2nd ed., Cambridge University Press.

Pruett, C. D., 2000: Eulerian time-domain filtering for spatial large-eddy simulation. *AIAA Journal*, **38**, 1634–1642.

Richardson, L. F., 1926: Atmospheric diffusion shown on a distance-neighbor graph. *Proc. R. Soc. London Ser. A*, **110**, 709–737.

Riedel, K. O., 2005: Locally optimal knots and tension parameters for exponential splines. *J. of Computational and Applied Math.*, **196**, 94–114.

Rotach, M. W., S. E. Gryning, and C. Tassone, 1996: A two-dimensional lagrangian stochastic dispersion model for daytime conditions. *Quarterly Journal Royal Meteorol. Soc.*, **122**, 367–389.

Sagaut, P., 1998: *Large Eddy Simulation for Incompressible Flows*, Springer.

Sawford, B. L., 2008: Reynolds number dependence of relative dispersion statistics in isotropic turbulence. *Physics of Fluids*, in press.

Schmidt, J. W. and W. Heß, 1987: Positive interpolation with rational quadratic splines. *Computing*, **38**, 261–267.

Schmidt, J. W. and W. Heß, 1988: Positivity of cubic polynomials on intervals and positive spline interpolation. *BIT Numerical Mathematics*, **28**, 340–352.

Schumann, U., 1975: Subgrid scale model for finite difference simulations of turbulent flows in plane channels and annuli. *J. Comp. Phys.*, **18**, 376–404.

Schwere, S., A. Stohl, and M. W. Rotach, 2002: Practical considerations to speed up lagrangian stochastic particle models. *Computer & Geosciences*, **28**, 143–154.

Scotti, A., C. Meneveau, and D. K. Lilly, 1993: Generalized smagorinsky model for anisotropic grids. *Phys. Fluids A*, **5**, 2306.

Shaw, R. and U. Schumann, 1992: Large-eddy simulation of turbulent flow above and within a forest. *Boundary Layer Meteorol.*, **61**, 47–64.

Smagorinsky, J., 1963: General circulation experiments with the primitive equations: I. the basic experiment. *Mon. Weather Rev.*, **91**, 99–164.

Srinivas, C. V., R. Venkatesan, R. Baskaran, V. Rajagopal, and B. Venkatraman, 2012: Regional scale atmospheric dispersion simulation of accidental releases of radionuclides from fukushima dai-ichi reactor. *Atmospheric Environment*, **61**, 66–84.

Stohl, A., M. Hittenberger, and G. Wotawa, 1998: Validation of the Lagrangian Particle Dispersion Model FLEXPART Against Large-Scale Tracer Experiment Data. *Atmospheric Environment*, **32**, 4245–4264.

Stohl, A. and T. Trickl, 1999: A textbook example of long-range transport: Simultaneous observation of ozone maxima of stratospheric and north american origin in the free troposphere over europe. *J. Geophys. Res.*, **104**, 30445, 30462.

Stull, R. B., 1988: *An introduction to boundary layer meteorology*, Kluwer Academic Publishers.

Taylor, G. I., 1921: Diffusion by continuos movements. *Proc. London Math. Soc.*, **20**, 196–211.

Taylor, G. I., 1935: Statistical theory of turbulence. *Proceedings of the Royal Society of London. Series A, Mathematical and Physical Sciences*, **151**, 421–444.

Thomson, D. J., 1987: Criteria for the selection of stochastic models of particle trajectories in turbulent flows. *J. Fluid Mech.*, **180**, 529–556.

Thomson, D. J., 1995: Discussion. *Atmos. Environ.*, **29**, 1343.

Troen, I. and L. Mahrt, 1986: A simple model of the atmospheric boundary layer: sensitivity to surface evaporation. *Boundary-Layer Meteorol.*, 129–148.

Van der Hoven, J., 1957: Power spectrum of horizontal wind speed in the frequency range from 0.0007 to 900 cycles per hour. *Journal of Meteorology*, **14**, 160–164.

Venkatram, A., 1993: The parameterization of the vertical dispersion of a scalar in the atmospheric boundary layer. *Atmospheric Environment*, **27A**, 1963–1966.

Vinkovic, I., C. Aguirre, M. Ayrault, and S. Simoens, 2006a: Large-eddy simulation of the dispersion of solid particles in a turbulent boundary layer. *Boundary Layer Meteorology*, **121**, 283311.

Vinkovic, I., C. Aguirre, and S. Simoens, 2006b: Large-eddy similation and lagrangian stochastic modeling of passive scalar dispersion in a turbulent boundary layer. *Journal of Turbulence*, **7**, 1–14.

Weil, J. C., W. H. Snyder, R. E. Lawson, jr., and M. S. Shipman, 2002: Experiments on buoyant plume dispersion in a laboratory convection tank. *Boundary-Layer Meteorol.*, **102**, 367–414.

Weil, J. C., P. P. Sullivan, and C.-H. Moeng, 2004: The use of large-eddy simulations in lagragian particle dispersion models. *Journal of the Atmospheric Sciences*, **61**, 2877–2887.

Weil, J. C., P. P. Sullivan, E. G. Patton, and C.-H. Moeng, 2012: Statistical variability of dispersion in the convective boundary layer: Ensembles of simulations and observations. *Boundary-Layer Meteorol*, **145**, 185–210.

Willis, G. and J. W. Deardorff, 1976: A laboratory model of diffusion into the convective planetary boundary layer. *Q. Journal Roy. Meteorol. Soc.*, **102**, 427–445.

Wilson, D. J. and E. Yee, 2007: A critical examination of the random displacement model of turbulent dispersion. *Boundary-Layer Meteorol.*, **125**, 399–416.

Wilson, J. D. and T. K. Flesch, 1993: Flow boundaries in random flight dispersion models: enforcing the well-mixed condition. *J. Appl. Meteorol.*, **32**, 1695–1707.

Wilson, J. D., B. J. Legg, and D. J. Thomson, 1983: Calculation of particle trajectories in the presence of a gradient in turbulent-velocity scale. *Boundary-Layer Meteorol.*, **27**, 163–169.

Wotawa, G., H. Kroger, and A. Stohl, 2000: Transport of ozone towards the alps - results from trajectory analyses and photochemical model studies. *Atmospheric Environment*, **34**, 1367–1377.